NUMERICAL SIMULATION AND MODELING

OF CELL MOTION IN MICROCHANNELS

A Dissertation

Presented to

the Faculty of the Department of Mathematics

University of Houston

In Partial Fulfillment

of the Requirements for the Degree

Doctor of Philosophy

By

Yao Yu

December 2013

NUMERICAL SIMULATION AND MODELING

OF CELL MOTION IN MICROCHANNELS

Yao Yu

APPROVED:

Dr. Tsorng-Whay Pan,
Chairman

Dr. Roland Glowinski

Dr. Jiwen He

Dr. Dong Liu
Department of Mechanical Engineering
University of Houston

Dean, College of Natural Sciences and Mathematics

Acknowledgements

My most sincere gratitude goes to my advisor and mentor, Dr. Tsorng-Whay Pan at the Department of Mathematics. I thank him for introducing me to the wonders of scientific research and guiding me through this endeavor. I thank him for his support, encouragement, and all of the care and love without any reservation. I thank him for his wide knowledge and innovative ideas which have provided a good basis for the present dissertation. Last but not the least, I would like to thank him for his continuous efforts and tremendous amount of time spent on helping me shape my research views and career goals.

His insightful comments and advices have been, and will always be, of great value for me in my life.

I wish to express my warm thanks to Professor Roland Glowinski, Professor Jiwen He, and Professor Dong Liu for their time and helpful comments to improve my work. I also want to express my gratitude to Professor Shanyu Ji for all kinds of his nice suggestions during my time at the Department of Mathematics.

Lots of thanks to fellow group members Xiting Niu, Lingling Shi, and Shihai Zhao for insightful discussions and sharing of their ideas and experience.

Last but most importantly, I am deeply grateful to my parents, Guitao Yu and Duofang Gao, for breeding me and cultivating me with their significant support, care, and love. Finally, I owe my loving thanks to my wife Qiuzi Liang, the most important person in my life. Without her consistent encouragement and wholehearted support, I would not have been able to finish this work and stand where I am. It is she who has made me a better man.

NUMERICAL SIMULATION AND MODELING

OF CELL MOTION IN MICROCHANNELS

An Abstract of a Dissertation

Presented to

the Faculty of the Department of Mathematics

University of Houston

In Partial Fulfillment

of the Requirements for the Degree

Doctor of Philosophy

By

Yao Yu

December 2013

Abstract

The motion of cells in flow has been studied in vivo, in viro, and in silico. Different models have been developed. In this dissertation we have compared the cell mostion with Navier-Stokes model and the Stokes model in both shear and Poseuille flow. Surprisingly, both models produce almost the same motion for most of the cases studied in this dissertation. Whether the cell motion is deformation-dominated or rigid body like determines if the Stokes model can be applied. When the red blood cell (RBC) are infected by malaria, the parasite forms a 'core' inside the cell. During the infection the chemicals released by the parasite make the cell membrane stiffer. We present the numerical simulations of the motion of a single Malaria-infected cell in narrow blood vessel under Poseuille flow and those of the interactions between an infected cell and multiple healthy cells. The infected cell migrates to the side of the channel due to loss of deformability and interaction with the healthy RBCs. And in the end, a power-law for the effective viscosity of a compounded cell has been obtained based on the filling volume fraction.

Contents

Chapter 1

Introduction

1.1 Motivation

The human blood is a complex fluid that is primarily composed of red blood cells (RBCs or erythrocytes), white blood cells (leukocytes), and platelets suspended in blood plasma. The blood plasma makes up about 55% of the total blood volume. It is mostly water (92% by volume), and contains dissolved proteins, hormones, and carbon dioxide. The RBCs plays the roles of delivering oxygen (O_2) to body tissues via the blood flow through the circulatory system. They take up oxygen in the lungs or gills and release it while squeezing through the body's capillaries. They take up about 44% of the blood volume (in whole blood), and the rest of the blood cells combined take less then 1% of the total blood volume. The erythrocyte volume fraction (or hematocrit (Hct)) decreases gradually along the branching sequence in blood vessels. In capillaries, the Hct is about 20%. As shown in Figure 1.1, a healthy RBC, when relaxed, has a distinctive biconcave shape of around $8\mu m$ in diameter and $2\mu m$ in thickness. The mean volume of a healthy RBC has

been reported to be around $100\mu m^3$, and the surface area around $134\mu m^2$, which is greater than the surface area $(104.18\mu m^2)$ of a sphere with the same volume [5]. This excess area contributes to the deformability of the RBC. The human RBC membrane is made of a lipid bilayer reinforced on its inner face by a flexible two-dimensional protein network called cytosekeleton. This skeleton is made of spectrin dimers associated to form mainly tetramers, approximately 200 nm long. They are linked together by complex junctions and attached to the lipid bilayer via transmembrane proteins. In a simplified description, they form a triangular network in which each actin filament is connected to six spectrin tetramers (see Figure 1.2). The composite properties of the phospholipid bilayer and spectrin network result in the discocyte morphology of healthy RBCs and give the membrane its elastic and biorheological properties. The bilayer has little shear resistance but contributes to bending resistance and helps to maintain cell surface area while the spectrin network or cytoskeleton is largely responsible for the shear elastic properties of the RBC. The RBC membrane is highly deformable, allowing it to deform easily under external forces and return to the biconcave shape after removal of the force [16].

Unhealthy RBCs show different mechanical properties comparing to healthy ones. Research shows that some diseases such as sickle cell anemia, diabetes mellitus, and malaria are responsible for stiffer cell membrane. When a merozoite invades an RBC, it undergoes structural changes within the RBC. Broadly we can classify the developmental stages of the parasite as 3 stages: (i) during the ring stage, the parasite forms a thin discoidal, flat or cup-shaped ring inside the cell; (ii) during the trophozoite stage the parasite starts performs an asexual reproduction within the RBC; and (iii) during the schizont stage, the parasite continues the reproduction and releases special proteins causing severe distortion of the cell cytoskeleton. The parasite it self is spherical, stiff, and very slow to deform [60, 39]. In Figure 1.3, an illustration of development of the merozoite in human RBC is
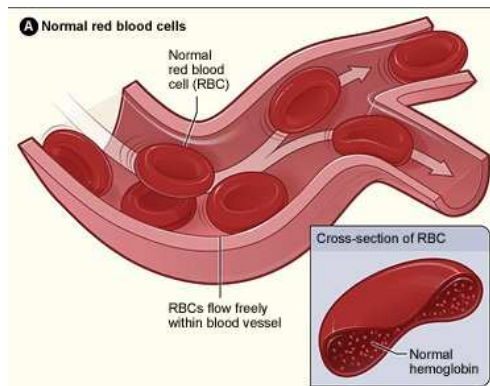
Figure 1.1: Normal red blood cells flowing freely in a blood vessel. The membrane is very soft allowing the RBC squeeze through narrow vessels. The inset image shows a cross-section of a normal red blood cell with normal hemoglobin [41] .
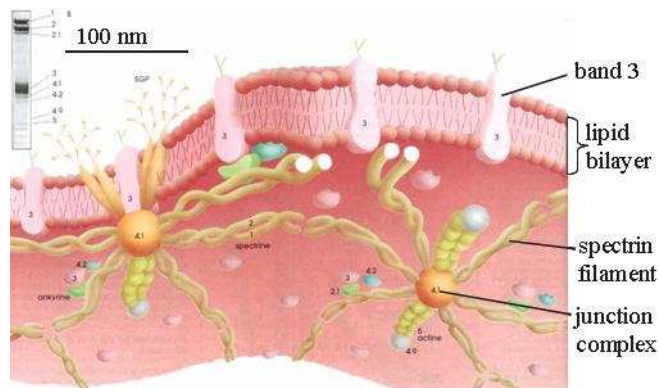
Figure 1.2: The cytoskeletal triangle mesh is embedded in the plasma phospholipid bilayer by the transmembrane proteins. The plasma layer is responsible for the constraints of constant area and resistance to buckling. It can rearrange itself very easily, and is often referred to as a fluid membrane. The network of proteins attached underneath the plasma layer is responsible for the shear resistance [59].
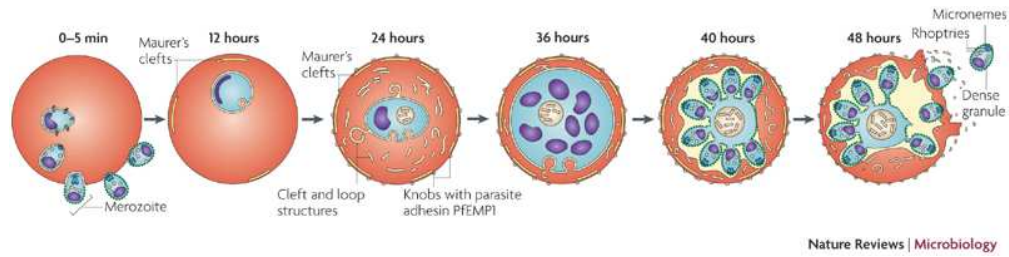
Figure 1.3: An illustration of development of malaria infection in human RBC. The merozoite undergoes through the ring stage (first 12 hours), the trophozoite stage (12 -24 hours), the schizont stage (24 - 40 hours), and finally finishes its reproduction and breaks the cell releasing more merozoite into the blood [40].

presented. Experiments show that the membrane of a malaria-infected RBC is about 10 times stiffer than a healthy RBC [37, 60]. The images of late stage malaria-infected RBC is shown in Figure 1.4.

Understanding the behavior of red blood cells in flow is fundamental to understanding the complex motion of blood. The behavior of soft entities, such as capsules, vesicles, and red blood cells has been studied theoretically [32, 54], experimentally [1, 21, 35], and numerically [27, 28, 29]. The Keller and Skalak model (KS model) for RBC assumes that the cell is shape preserving and is made of a viscous liquid drop surrounded by an in-extensible membrane. Due to these assumptions, the mechanical properties of the membrane is neglected. The dynamics of the cell can be determined by the geometry of the cell, the ratio of the viscosity contrast (λ) of the internal and external fluid, and the shear rate of the imposed flow. Based on the KS model, a steady inclination angle θ is obtained when λ is small, and a critical viscosity contrast ratio λ^* is obtained by setting the steady inclination angle $\theta^* = 0$ to seperate the steady tank-treading (TT) motion and the unsteady tumbling (TB) motion. The Skotheim and Scomb's model (SS model), basing on the KS model,
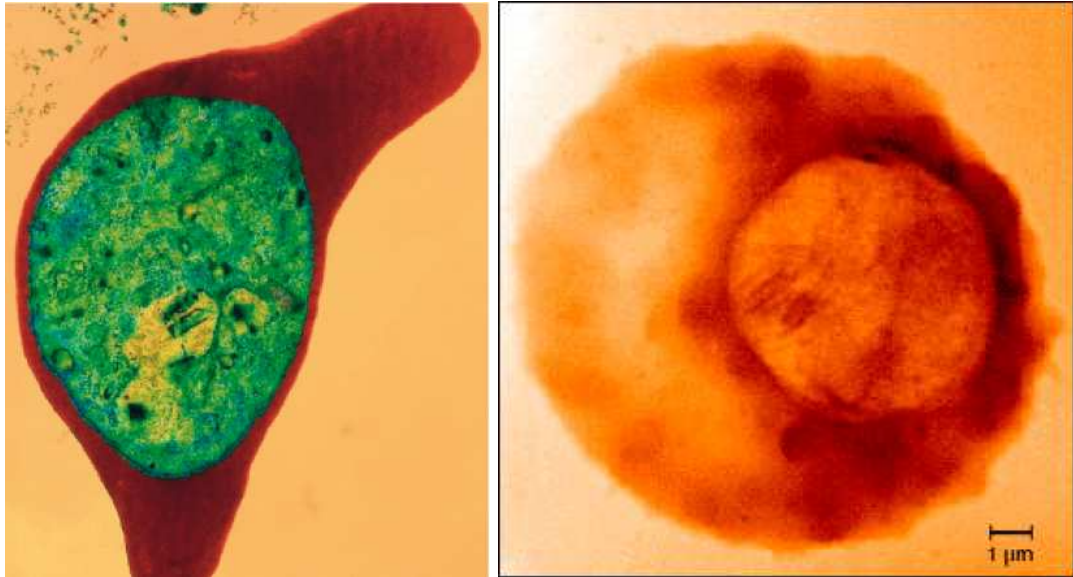
Figure 1.4: In the picture on the left, the red blob is a human red blood cell, and the green blob in the middle of it is a pack of the malaria-causing parasites Plasmodium falciparum. P. falciparum is responsible for almost all of the million-plus deaths due to malaria [15]. Shown in the right is an x-ray image taken at Berkeley Labs Advanced Light Source, the malaria parasite develops inside a red blood cell, where it accumulates iron [36] .

added the effect of the elastic energy of the cell membrane. It predicts the intermittent motion which is characterized by a combination of the swinging and tumbling motions. Such motion is captured in experiment by Abkarian *et al.* [1], and numerically by Niu *et al.* [42]. The deformation dynamics of the cell is neglected in the above two models. The vesicle model and the capsule model included the effect of deformation. A vesicle takes into consideration of bending rigidity but neglects shear elasticity. By this it shares a very important property with the real RBC – their membrane area is inextensible (or circumference is conserved in 2D). On the other hand, a capsule is extensible under shear external force but has no resist to bending. The spring-network model by Tsubota *et al.*

5

[62] includes both the shear and the bending elasticity.

Different flow models are used in numerical simulation of the blood flow. Instead of solving the full Navier-Stokes equations for the fluid field [31, 56, 67], many researchers use the stationary [27, 34] or non-stationary Stokes equations [4] to model the fluid assuming low Reynolds number. A comparison among motions of a soft RBC under two different flow models, namely the Navier-Stokes model and the Stokes model, are investigated in this dissertation.

Numerical simulation of RBC rheology have attracted growing interest since it is difficult to deal with *in vivo* and *in vitro* experiments to study microcirculation and RBC rheology due to the size limitation. Boundary element method (BEM) is used in [51]. The advantage of BEM arises from that there is no need to mesh the whole domain of the problem but only its boundary. But BEM formulations typically give rise to fully populated matrices. This means the storage requirements and computational time tend to grow according to the square of the problem size. Another short coming about the BEM method is that the flow is restricted to Stokesian flow, as there is no Green's function for Navier-Stokes equations. Yoshino *et al.* applied the lattice Boltzmann method to study the motion of a visco-elastic body in a Poiseuille flow and observed that the equilibrium position is very close to the center line for a low elasticity and it is at a certain position between the center line and the wall for a larger elasticity [65]. Danker *et al.* investigated the effect of viscosity ratio on the migration of vesicles in a Poiseuille flow by theoretical analysis, and predicted coexistence of two types of shapes: a bullet-like shape and a parachute-like shape [10]. Li *et al.* investigated the shape change and motion of the vesicle by using the lattice-Boltzmann method [53]. An operator splitting technique [12, 19] is adopted to solve the fluid-cell equations governed by the Navier-Stokes equations. We

apply a pre-conditioned conjugate gradient method in solving the Stokes-type sub-problem in the operator splitting and the stationary and non-stationary Stokes equations.

Concerning the cell motion in shear flow, three different types of motions have been observed: the tank-treading motion, in which the cell stays at a stable inclination angle (angle between the cell long axis and the horizontal line) while the membrane rotates as a tank tread [14, 27, 32, 54]; the tumbling motion, in which the whole cell rotates like a rigid body [25, 38, 43]; and the vacillating-breathing motion, in which the long axis of the cell undergoes oscillation about the flow while the shape shows a breathing behavior [38, 43].

The behavior of a RBC in Poiseuille flow is rather interesting and important in both biomedical and biochemical industries. Motions of drops, capsules, vesicles, rigid particles, and RBCs are investigated by researchers. An RBC tends to move toward the flow center where the flow is faster. Kaoui *et al.* [26] studied the cross-stream noninertial migration of a suspended vesicle in an unbounded (Coupier *et al.* [9] studied the bounded case) Poiseuille flow and found that the vesicle deforms and migrates toward the center of the flow. Pozrikidis studied the motion of different shaped capsules in tube flow and observed that capsules migrate to the tube center line. Numerical simulation of Shi *et al.* also showed that RBC, regardless of initial position, migrates toward the channel center when released in bounded Poiseuille flow [56].

Numerical simulation of the motion of a compound cell in flow can help understand the behavior of malaria-infected RBCs in blood flow and then can help design cell separation tools in malaria treatment. A compounded droplet model was employed by Tasoglu *et al.* [61] and Kan *et al.* [24] to simulate motion of human leukocytes in flow. But the soft mechanical property of the included drop also undergoes deformation during the motion, while the 'core' formed by parasite is much more rigid. Numerical simulation of a compound

vesicle enclosing a rigid core in shear flow is investigated by Lai *et al.* and Shraven *et al.* separately. The inclination angle of the final steady state is smaller than that of a vesicle of the same shape without inclusion due to bigger cytoplasmic viscosity. Karniadakis [30] investigated the raised apparent viscosity in tube flow due to infected cells. Wu *et al.* [64] showed that parasite-infected RBC becomes less deformable and fail to squeeze through narrow channel. Numerical simulations of a single infected cell in bounded Poiseuille flow and the interactions between infected cell and healthy cells are presented in this dissertation.

1.2   Dissertation outline

The purpose of this dissertation is to investigate the rheological properties of RBCs in microchannels. To achieve this goal, an elastic spring model [62] is chosen to model the skeleton structure of a RBC membrane in two dimensions. An immersed boundary method [47, 48, 49] combined with the elastic spring model is used to simulate the interaction between the cell and fluid flow. An operator splitting technique [12, 19] is adopted to solve the fluid-cell system equations governed by the Navier-Stokes equations. A pre-conditioned conjugate gradient method is applied to solve the Stokes equation. To deal with the rigid particle in flow, we use a distributed Lagrange multiplier-based fictitious domian method [19, 20, 45, 46]. The no-slip condition on the RBC membrane surface is enforced.

This dissertation is devoted to investigating the motion and deformation of a single RBC or collective RBCs in microchannels by direct numerical simulations. Here is an outline for this dissertation:

In Chapter 2, we introduce the methodologies used and developed in this dissertation.

An elastic spring model is chosen to model the skeleton structure of a RBC membrane. An immersed boundary method combined with the elastic spring model is applied to study the interaction between RBC and the fluid. An operator splitting technique is adopted to solve the fluid-cell system equations governed by the Navier-Stokes equations or the stationary Stokes equations. A pre-conditioned conjugate gradient method is used to solve the Stokes type equations. A distributed Lagrange multiplier-based fictitious domian method is applied to deal with the rigid inclusion for the malaria problem.

In Chapter 3, we validate the two flow models and methodologies by the comparison of the steady inclination angles of the tank treading motion of a single RBC in a shear flow and then analyze the motion of RBC in pressure driven Poiseuille flow under two different flow models.

In Chapter 4, we validate the compound cell model by commparing the steady inclination angles of the tank treading motion of a swallen RBC with rigid inclusion of different sizes. We then analyze the effect of solid inclusion on the leteral migration of cells in Poiseuille flow. Furthermore, the interactions between malaria-infected RBC and healthy RBCs in a narrow channel is investigated. Those healthy cells tend to stay in the channel center as in Poiseuille flow and hence they pushes the infected cell to the side.

In Chapter 5, we present a new scheme for handling the situation where the viscosity contrast is greater than 1. And then use this new scheme to investigate the effective viscosity of the RBC with a rigid filling by comparing the inclination angle of a compounded RBC and that of a RBC with higher cyto-plasma viscosity.

In Chapter 6, we summarize our research and discuss future direction.

Chapter 2

Models and methods

2.1 Flow models
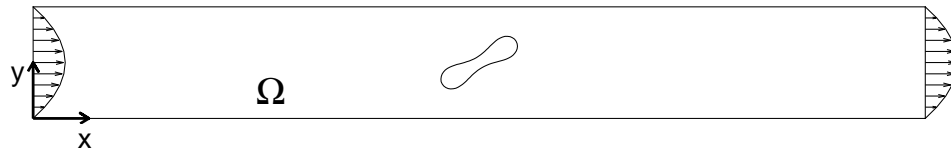
Figure 2.1: Schematic of a single red blood cell in plane Poiseuille flow with the computational domain Ω.

An elastic spring network model is chosen to model the skeleton structure of RBC membrane. Such model combined with an immersed boundary method and finite element method is applied to study the RBC rheology in two-dimensional microchannels. The governing equations for the fluid-cell system are the Navier- Stokes equations

$$\rho_f \left(\frac{\partial \mathbf{u}}{\partial t} + \mathbf{u} \cdot \nabla \mathbf{u} \right) - \nabla \cdot [2\mu(\mathbf{x}, t) D(\mathbf{u})] + \nabla p = \mathbf{f}, \text{ in } \Omega \times (0, T), \qquad (2.1)$$

$$\nabla \cdot \mathbf{u} = 0 \text{ in } \Omega \times (0, T). \qquad (2.2)$$

Here the domain Ω is a bounded region filled with blood plasma which is incompressible, Newtonian, and contains RBC(s) as in Figure 2.1.

The governing equations (2.1)-(2.2) are completed by the following boundary and initial conditions:

$$\mathbf{u} = \mathbf{g} \text{ on the top and bottom of } \Omega \text{ and } \mathbf{u} \text{ is periodic in the } \mathbf{x} \text{ direction}, \qquad (2.3)$$

$$\mathbf{u}(\mathbf{x}, 0) = \mathbf{u}_0(\mathbf{x}), \text{ in } \Omega. \qquad (2.4)$$

where $\mathbf{u}$ and p are the fluid velocity and pressure, respectively, ρ_f is the fluid density, and since in general the viscosity of the plasma and that of the cytoplasm are different, we denote the viscosity over the entire domain by $\mu(\mathbf{x}, t)$. In eq. (2.1), we have $\mathbf{D}(\mathbf{v}) = (\nabla \mathbf{v} + \nabla \mathbf{v}^t)/2$ (when the viscosity μ is constant throughout the domain, the term $-\nabla \cdot [2\mu(\mathbf{x}, t) D(\mathbf{u})]$ can be replaced with $\mu \triangle \mathbf{u}$), $\mathbf{f}$ is a body force which is the sum of $\mathbf{f}_p$ and $\mathbf{f}_B$ where $\mathbf{f}_p$ is the pressure gradient pointing in the x direction and $\mathbf{f}_B$ accounts for the force acting on the interface between fluid and cell. In eq. (2.4), $\mathbf{u}_0(\mathbf{x})$ is the initial fluid velocity. For the cases of shear flow, the external force $\mathbf{f}_p$ is set to zero. For the cases of Poiseuille flow, the boundary condition is $\mathbf{g} = 0$ on the top and bottom of Ω.

When the flow is very slow, we can understand it as an 'almost' steady flow. Since the $\frac{\partial \mathbf{u}}{\partial t}$ term and the $\mathbf{u} \cdot \nabla \mathbf{u}$ term is much smaller than the other terms in equation (2.1), some researchers choose to omit those two terms and use the stationary Stokes equations [27, 34]

$$-\nabla \cdot [2\mu(\mathbf{x}, t) D(\mathbf{u})] = -\nabla p + \mathbf{f} \text{ in } \Omega \times (0, T), \qquad (2.5)$$

$$\nabla \cdot \mathbf{u} = 0 \text{ in } \Omega \times (0, T). \qquad (2.6)$$

11

or the non-stationary Stokes equations [4]

$$\rho_f \frac{\partial \mathbf{u}}{\partial t} - \nabla \cdot [2\mu(\mathbf{x}, t) D(\mathbf{u})] + \nabla p = \mathbf{f} \text{ in } \Omega \times (0, T), \tag{2.7}$$

$$\nabla \cdot \mathbf{u} = 0 \text{ in } \Omega \times (0, T). \tag{2.8}$$

as the governing equation of such flow.

2.2   Elastic spring model for the RBC membrane
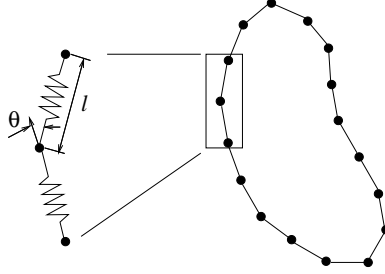
Figure 2.2: The elastic spring model of the RBC membrane

A two-dimensional elastic spring model developed in [62] is considered in this paper to describe the deformable behavior of the RBCs. Based on this model, the RBC membrane can be viewed as membrane particles connecting with the neighboring membrane particles by springs, as shown in Figure 2.2. Elastic energy stores in the spring due to the change of the length l of the spring with respected to its reference length l_0 and the change in angle θ between two neighboring springs. The total elastic energy of the RBC membrane, $E = E_l + E_b$, is the sum of the total elastic energy for stretch/compression and the total energy for bending which, in particular, are

$$E_l = \frac{k_l}{2} \sum_{i=1}^{N} (\frac{l_i - l_0}{l_0})^2 \tag{2.9}$$

12

and

$$E_b = \frac{k_b}{2} \sum_{i=1}^{N} \tan^2(\theta_i/2). \tag{2.10}$$

In equations (2.9) and (2.10), N is the total number of the spring elements, and k_l and k_b are spring constants for changes in length and bending angle, respectively.

In the process of creating the initial shape of RBCs described in [62], the RBC is assumed to be a circle of radius $R_0 = 2.8 \ \mu$m initially. The circle is discretized into $N = 76$ membrane particles so that 76 springs are formed by connecting the neighboring particles. The shape change is stimulated by reducing the total area of the circle through a penalty function

$$\Gamma_s = \frac{k_s}{2}(\frac{s - s_e}{s_e})^2 \tag{2.11}$$

where s and s_e are the time dependent area of the RBC and the equilibrium area of the RBC, respectively, and the total energy is modified as $E + \Gamma_s$. Based on the principle of virtual work the force acting on the ith membrane particle now is

$$\mathbf{F}_i = -\frac{\partial(E + \Gamma_s)}{\partial \mathbf{r}_i} \tag{2.12}$$

where $\mathbf{r}_i$ is the position of the ith membrane particle. When the area is reduced, each RBC membrane particle moves on the basis of the following equation of motion:

$$m\ddot{\mathbf{r}}_i + \gamma\dot{\mathbf{r}}_i = \mathbf{F}_i \tag{2.13}$$

Here, $\dot{()}$ denotes the time derivative; m and γ represent the membrane particle mass and the membrane viscosity of the RBC. The position $\mathbf{r}_i$ of the ith membrane particle is solved by discretizing (2.13) via a second-order finite difference method. The total energy stored in the membrane decreases as the time elapses. The final shape of the RBC is obtained as the total elastic energy is minimized (please see [63]). The area of the final shape has less than 0.001% difference from the given equilibrium area s_e and the length of the perimeter

of the final shape has less than 0.005% difference from the circumference of the initial circle. The reduced area of a RBC in this paper is defined by $s^* = s_e / \pi R_0^2$.

2.3 Fictitious domain formulation for the malaria-infected RBCs
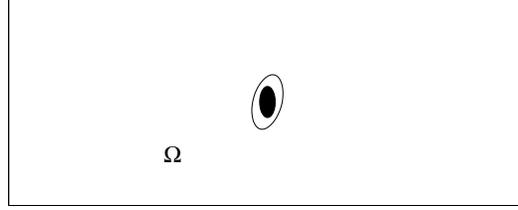
Figure 2.3: An example of computational domain with one malaria-infected RBC.

Let Ω be a bounded rectangular domain filled with blood plasma which is incompressible, Newtonian, and contains malaria-infected RBC(s) with the viscosity of the cytoplasm same as that of the blood plasma (see Figure 2.3). We suppose, for simplicity, that in Ω there is a infected RBC containing a freely moving rigid particle B centered at $\mathbf{G} = \{G_1, G_2\}^t$; the flow is modeled by the *Navier-Stokes equations* and the motion of the particle B is described by the *Euler-Newton's equations*. We define

$$W_{0,p} = \{\mathbf{v} | \mathbf{v} \in (H^1(\Omega))^2, \ \mathbf{v} = \mathbf{0} \text{ on the top and bottom of } \Omega \text{ and}$$

$$\mathbf{v} \text{ is periodic in the } x_1 \text{ direction}\},$$

$$L_0^2 = \{q | q \in L^2(\Omega), \int_\Omega q \, d\mathbf{x} = 0, \},$$

$$\Lambda_0(t) = \{\boldsymbol{\mu} | \boldsymbol{\mu} \in (H^1(B(t)))^2, < \boldsymbol{\mu}, \mathbf{e}_i >_{B(t)} = 0, \ i = 1, 2, < \boldsymbol{\mu}, \overrightarrow{Gx}^\perp >_{B(t)} = 0\}$$

with $\mathbf{e}_1 = \{1, 0\}^t$, $\mathbf{e}_2 = \{0, 1\}^t$, $\overrightarrow{Gx}^\perp = \{-(x_2 - G_2), x_1 - G_1\}^t$ and $< \cdot, \cdot >_{B(t)}$ an inner product on $\Lambda_0(t)$ which can be the standard inner product on $(H^1(B(t)))^2$ (see, e.g., [18],

14

for further information on the choice of $<\cdot,\cdot>_{B(t)}$). Then as in [44], the fictitious domain formulation with distributed Lagrange multipliers for the flow with an infected RBC around a freely moving neutrally buoyant particle is as follows

$For\ a.e.\ t > 0,\ find\ \mathbf{u}(t) \in W_{0,p},\ p(t) \in L_0^2,\ \mathbf{V_G}(t) \in \mathbb{R}^2,\ \mathbf{G}(t) \in \mathbb{R}^2,$

$\omega(t) \in \mathbb{R},\ \boldsymbol{\lambda}(t) \in \Lambda_0(t)\ \ such\ that$

$$\begin{cases} \rho \int_\Omega \left[\frac{\partial \mathbf{u}}{\partial t} + (\mathbf{u} \cdot \boldsymbol{\nabla})\mathbf{u} \right] \cdot \mathbf{v}\ d\mathbf{x} + 2\mu \int_\Omega \mathbf{D}(\mathbf{u}) : \mathbf{D}(\mathbf{v})\ d\mathbf{x} - \int_\Omega p\boldsymbol{\nabla} \cdot \mathbf{v}\ d\mathbf{x} \\ \quad - <\boldsymbol{\lambda}, \mathbf{v}>_{B(t)} = \rho \int_\Omega \mathbf{g} \cdot \mathbf{v}\ d\mathbf{x} + \int_\Omega \mathbf{f} \cdot \mathbf{v}\ d\mathbf{x},\ \forall \mathbf{v} \in W_{0,p}, \end{cases} \tag{2.14}$$

$$\int_\Omega q\boldsymbol{\nabla} \cdot \mathbf{u}(t) d\mathbf{x} = 0,\ \forall q \in L^2(\Omega), \tag{2.15}$$

$$<\boldsymbol{\mu}, \mathbf{u}(t)>_{B(t)} = 0,\ \forall \boldsymbol{\mu} \in \Lambda_0(t), \tag{2.16}$$

$$\frac{d\mathbf{G}}{dt} = \mathbf{V_G}, \tag{2.17}$$

$$\mathbf{V_G}(0) = \mathbf{V_G^0},\ \omega(0) = \omega^0,\ \mathbf{G}(0) = \mathbf{G}^0 = \{G_1^0, G_2^0\}^t, \tag{2.18}$$

$$\mathbf{u}(\mathbf{x}, 0) = \overline{\mathbf{u}}_0(\mathbf{x}) = \begin{cases} \mathbf{u}_0(\mathbf{x}),\ \forall \mathbf{x} \in \Omega \backslash \overline{B(0)}, \\ \mathbf{V_G^0} + \omega^0\{-(x_2 - G_2^0), x_1 - G_1^0\}^t,\ \forall \mathbf{x} \in \overline{B(0)}, \end{cases} \tag{2.19}$$

where $\mathbf{u}$ and p denote velocity and pressure, respectively, ρ is the fluid density, and μ is the fluid viscosity. We also assume that the flow is periodic in the x_1 direction with period L, L being the length of the channel Ω. In the above (2.14)-(2.19), we have $\mathbf{D}(\mathbf{v}) = (\boldsymbol{\nabla}\mathbf{v} + \boldsymbol{\nabla}\mathbf{v}^t)/2$, $\boldsymbol{\lambda}$ is a Lagrange multiplier, $\mathbf{g}$ is gravity, $\mathbf{f}$ is a body force which is the sum of $\mathbf{f}_p$ and $\mathbf{f}_B$ where $\mathbf{f}_p$ is the pressure gradient pointing in the x_1 direction and $\mathbf{f}_B$ accounts for the force acting on the fluid/cell interface (please see the following sections), $\mathbf{V_G}$ is the *translation velocity* of the particle B, and ω is the *angular velocity* of the particle B. We suppose that the *no-slip* condition holds on ∂B. We also use, if necessary, the notation $\phi(t)$ for the function $\mathbf{x} \to \phi(\mathbf{x}, t)$.

In (2.14) and (2.16), the rigid body motion in the region occupied by the particle is enforced via the Lagrange multipliers $\boldsymbol{\lambda}$. As discussed in [44], we solve the following equations to obtain the translation velocity $\mathbf{V_G}(t)$ and the angular velocity $\omega(t)$ once $\mathbf{u}(t)$ is known

$$\begin{cases} < \mathbf{e}_i, \mathbf{u}(t) - \mathbf{V_G}(t) - \omega(t)\ \overrightarrow{Gx}^{\perp} >_{B(t)} = 0, \ \ for \ i = 1, 2, \\ < \overrightarrow{Gx}^{\perp}, \mathbf{u}(t) - \mathbf{V_G}(t) - \omega(t)\ \overrightarrow{Gx}^{\perp} >_{B(t)} = 0. \end{cases} \tag{2.20}$$

In (2.14), $2\int_{\Omega} \mathbf{D}(\mathbf{u}) : \mathbf{D}(\mathbf{v})\, d\mathbf{x}$ can be replaced by $\int_{\Omega} \boldsymbol{\nabla}\mathbf{u} : \boldsymbol{\nabla}\mathbf{v}\, d\mathbf{x}$ since $\mathbf{u}$ is divergence free and in $W_{0,p}$. Also the gravity $\mathbf{g}$ in (2.14) can be absorbed into the pressure term.

2.4   Immersed boundary method

The immersed boundary (IB) methods developed by Peskin, e.g, [47, 48, 49], is employed in this study because of its distinguish features in dealing with the problem of fluid flow interacting with a flexible fluid/structure interface. Over the years, it has demonstrated its capability in study of computational fluid dynamics including blood flow. Based on the IB method, the boundary of the deformable structure is discretized spatially into a set of boundary nodes. The force located at the immersed boundary node $\mathbf{X} = (X_1, X_2)$ affects the nearby fluid mesh nodes $\mathbf{x} = (x_1, x_2)$ through a 2D discrete δ-function $D_h(\mathbf{X} - \mathbf{x})$:

$$\mathbf{f}_B(\mathbf{x}) = \sum \mathbf{F}_i D_h(\mathbf{X}_i - \mathbf{x}) \quad for \ |\mathbf{X} - \mathbf{x}| \leq 2h, \tag{2.21}$$

where h is the uniform finite element mesh size and

$$D_h(\mathbf{X} - \mathbf{x}) = \delta_h(X_1 - x_1)\delta_h(X_2 - x_2) \tag{2.22}$$

with the 1D discrete δ-functions being

$$\delta_h(z) = \begin{cases} \frac{1}{8h}\left(3 - 2|z|/h + \sqrt{1 + 4|z|/h - 4(|z|/h)^2}\right), & |z| \le h, \\ \frac{1}{8h}\left(5 - 2|z|/h - \sqrt{-7 + 12|z|/h - 4(|z|/h)^2}\right), & h \le |z| \le 2h, \\ 0, & otherwise. \end{cases} \quad (2.23)$$

The movement of the immersed boundary node $\mathbf{X}$ is also affected by the surrounding fluid and therefore is enforced by summing the velocities at the nearby fluid mesh nodes $\mathbf{x}$ weighted by the same discrete δ-function:

$$\mathbf{U}(\mathbf{X}) = \sum h^2 \mathbf{u}(\mathbf{x}_j) D_h(\mathbf{X} - \mathbf{x}_j) \quad for \ |\mathbf{X} - \mathbf{x}_j| \le 2h. \quad (2.24)$$

After each time step, the position of the immersed boundary node is updated by

$$\mathbf{X}_{t+\Delta t} = \mathbf{X}_t + \Delta t \mathbf{U}(\mathbf{X}_t). \quad (2.25)$$

2.5 Space approximation and time discretization

2.5.1 Finite dimensional subspaces
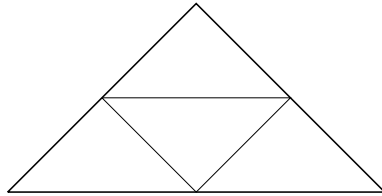
Figure 2.4: Schematic representation of a FEM triangulation and its subtriangulation.

Concerning the finite element-based *space approximation* of $\{\mathbf{u}, p\}$ in problem (2.14)-(2.19), we have used the P_1-*iso*-P_2 and P_1 finite element approximation (e.g., see [19]

(Chapter 5)). Suppose that a rectangular computational domain $\Omega \subset R^2$ is chosen with length L, h is a space discretization meshsize, $\mathcal{T}_h$ is a finite element triangulation of $\overline{\Omega}$ for velocity, and $\mathcal{T}_{2h}$ is a twice coarser triangulation for pressure (see Figure 2.4). Let P_1 be the space of polynomials in two variables of degree ≤ 1, we introduce the finite dimensional spaces:

$$W_{0h} = \{\mathbf{v}_h | \mathbf{v}_h \in C^0(\overline{\Omega})^2, \mathbf{v}_h|_T \in P_1 \times P_1, \forall T \in \mathcal{T}_h, \mathbf{v}_h = \mathbf{0} \text{ on the top and bottom}$$
$$\text{of } \Omega \text{ and is periodic in the } x_1 \text{ direction with period } L\},$$

$$L_h^2 = \{q_h | q_h \in C^0(\overline{\Omega}), q_h|_T \in P_1, \forall T \in \mathcal{T}_{2h}, \ q_h \text{ is periodic in the } x_1$$
$$\text{direction with period } L\},$$

$$L_{0h}^2 = \{q_h | q_h \in L_h^2, \int_\Omega q_h d\mathbf{x} = 0\}.$$

A finite dimensional space approximating $\Lambda_0(t)$ is defined as follows: let $\{\mathbf{x}_i\}_{i=1}^N$ be a set of points covering $\overline{B(t)}$; we define then

$$\Lambda_h(t) = \{\boldsymbol{\mu}_h | \boldsymbol{\mu}_h = \sum_{i=1}^N \boldsymbol{\mu}_i \delta(\mathbf{x} - \mathbf{x}_i), \ \boldsymbol{\mu}_i \in \mathbb{R}^2, \ \forall i = 1, ..., N\}, \tag{2.26}$$

where $\delta(\cdot)$ is the Dirac measure at $\mathbf{x} = \mathbf{0}$. Then, instead of the scalar product of $(H^1(B(t)))^2$, we shall use $< \cdot, \cdot >_{B_h(t)}$ defined by

$$< \boldsymbol{\mu}_h, \mathbf{v}_h >_{B_h(t)} = \sum_{i=1}^N \boldsymbol{\mu}_i \cdot \mathbf{v}_h(\mathbf{x}_i), \ \forall \boldsymbol{\mu}_h \in \Lambda_h(t), \ \mathbf{v}_h \in W_{0,h}. \tag{2.27}$$

Then we approximate $\Lambda_0(t)$ by

$$\Lambda_{0,h}(t) = \{\mu_h | \mu_h \in \Lambda_h(t), \ < \mu_h, \mathbf{e}_i >_{B_h(t)} = 0, \ i = 1, 2, \ < \mu_h, \overrightarrow{Gx}^\perp >_{B_h(t)} = 0\}. \tag{2.28}$$

A typical choice of points for defining $\Lambda_h(t)$ is to take the grid points of the velocity mesh internal to the region $B(t)$ and whose distance to the boundary of $B(t)$ is greater than, e.g. $h/2$, and to complete with selected points from the boundary of $B(t)$.

2.5.2 A scheme for flow modeled by the Navier-Stokes equations

In this subsection we present a DLM/FD/IB method scheme for an iRBC cell moving in fluid flows modeled by the Navier-Stokes equation. We apply the *Lie's scheme* [6, 19] to equations (2.14)-(2.19) with the backward Euler method in time for some subproblems and obtain the following fractional step subproblems (some of the subscripts h have been dropped):

$\mathbf{u}^0 = \mathbf{u}_0$ is given; for $n \geq 0$, $\mathbf{u}^n$ being known, we compute the approximate solution via the following fractional steps:

1. Solve

$$
\begin{cases}
\rho \displaystyle\int_\Omega \frac{\mathbf{u}^{n+1/6} - \mathbf{u}^n}{\triangle t} \cdot \mathbf{v} d\mathbf{x} - \int_\Omega p^{n+1/6}(\boldsymbol{\nabla} \cdot \mathbf{v})d\mathbf{x} = 0, \ \ \forall \mathbf{v} \in W_{0h}, \\
\displaystyle\int_\Omega q \boldsymbol{\nabla} \cdot \mathbf{u}^{n+1/6} d\mathbf{x} = 0, \ \ \forall q \in L_h^2, \\
\mathbf{u}^{n+1/6} \in W_{0h}, \ \ p^{n+1/6} \in L_{0h}^2.
\end{cases}
\tag{2.29}
$$

2. Update the position of the membrane by (2.24) and (2.25) and then compute the force $\mathbf{f}_B^{n+1/6}$ on the fluid/cell interface by (2.12) and (2.21) and obtain $\mathbf{f}^{n+1/6} = \mathbf{f}_p + \mathbf{f}_B^{n+1/6}$.

3. Solve

$$
\begin{cases}
\displaystyle\int_\Omega \frac{\partial \mathbf{u}(t)}{\partial t} \cdot \mathbf{v} d\mathbf{x} + \int_\Omega (\mathbf{u}^{n+1/6} \cdot \boldsymbol{\nabla})\mathbf{u}(t) \cdot \mathbf{v} d\mathbf{x} = 0 \ \ on \ \ (t^n, t^{n+1}), \ \ \forall \mathbf{v} \in W_{0h}, \\
\mathbf{u}(t^n) = \mathbf{u}^{n+1/6}, \\
\mathbf{u}(t) \in W_{0h} \ \ on \ \ (t^n, t^{n+1}),
\end{cases}
\tag{2.30}
$$

and set $\mathbf{u}^{n+2/6} = \mathbf{u}(t^{n+1})$.

4. Next, compute $\mathbf{u}^{n+3/6}$ via the solution of

$$\begin{cases} \rho \int_{\Omega} \dfrac{\mathbf{u}^{n+3/6} - \mathbf{u}^{n+2/6}}{\triangle t} \cdot \mathbf{v}\,d\mathbf{x} + \mu \int_{\Omega} \nabla \mathbf{u} : \nabla(\mathbf{v})\,d\mathbf{x} = \int_{\Omega} \mathbf{f}^{\mathbf{n+1/6}} \cdot \mathbf{v}\,d\mathbf{x}, \\[2mm] \forall \mathbf{v} \in W_{0,h}; \quad \mathbf{u}^{n+3/6} \in W_{0,h}. \end{cases} \tag{2.31}$$

5. Now predict the position and the translation velocity of the center of mass of the particles by:

$$\omega^{n+4/6} = \omega^n \tag{2.32}$$

$$\mathbf{V_G}^{n+4/6} = \mathbf{V_G}^n, \tag{2.33}$$

$$\mathbf{G}^{n+4/6} = \mathbf{G}^n + \frac{\triangle t}{2}\mathbf{V_G}^{n+3/6} \tag{2.34}$$

6. Now, compute $\mathbf{u}^{n+5/6}$, $\boldsymbol{\lambda}^{n+5/6}$, $\mathbf{V_G}^{n+5/6}$, and $\omega^{n+5/6}$ via the solution of

$$\begin{cases} \rho \int_{\Omega} \dfrac{\mathbf{u}^{n+5/6} - \mathbf{u}^{n+3/6}}{\triangle t} \cdot \mathbf{v}\,d\mathbf{x} = < \boldsymbol{\lambda}, \mathbf{v} >_{B_h^{n+4/6}}, \;\; \forall \mathbf{v} \in W_{0,h}, \\[2mm] < \boldsymbol{\mu}, \mathbf{u}^{n+5/6} >_{B_h^{n+4/6}} = 0, \;\; \forall \boldsymbol{\mu} \in \Lambda_{0,h}^{n+4/6}; \;\; \mathbf{u}^{n+5/6} \in W_{0,h}, \boldsymbol{\lambda}^{n+5/6} \in \Lambda_{0,h}^{n+4/6}, \end{cases} \tag{2.35}$$

and solve for $\mathbf{V_G}^{n+5/6}$ and $\omega^{n+5/6}$ from

$$\begin{cases} < \mathbf{e}_i, \mathbf{u}^{n+5/6} - \mathbf{V_G}^{n+5/6} - \omega^{n+5/6}\,\overrightarrow{G^{n+4/6}x}^{\perp} >_{B_h^{n+4/6}} = 0, \;\; for\; i = 1, 2, \\[2mm] < \overrightarrow{G^{n+4/6}x}^{\perp}, \mathbf{u}^{n+5/6} - \mathbf{V_G}^{n+5/6} - \omega^{n+5/6}\,\overrightarrow{G^{n+4/6}x}^{\perp} >_{B_h^{n+4/6}} = 0, \end{cases} \tag{2.36}$$

7. Finally, obtain the final position of the particle by:

$$\omega^{n+1} = \omega^{n+5/6} \tag{2.37}$$

$$\mathbf{V_G}^{n+1} = \mathbf{V_G}^{n+5/6}, \tag{2.38}$$

$$\mathbf{G}^{n+1} = \mathbf{G}^{n+4/6} + \mathbf{V_G}^{n+1}\frac{\triangle t}{2}. \tag{2.39}$$

In the above algorithm (2.29)-(2.39), we have $t^{n+s} = (n+s)\triangle t$, $\Lambda_{0,h}^{n+s} = \Lambda_{0,h}(t^{n+s})$, B_h^{n+s} is the region occupied by the particle centered at $\mathbf{G}^{n+s}$.

When simulating the case involving both cells and neutrally buoyant particles, we do need a repulsive force to prevent the overlapping between cell and particle. The repulsive force is obtained from the following Morse potential (e.g., see [3])

$$\phi(s) = k_r(1 - e^{-(s-s_0)})^2$$

where the parameter s is the shortest distance between the membrane particle and the surface of the solid particle and s_0 is the range of the repulsive force (when the distance s is greater than s_0, there is no repulsive force). The parameter k_r is a constance for the strength of the potential. At the step (2) in the above algorithm (2.29)-(2.39), we then also add the repulsive $\mathbf{f}_r = -\dfrac{\partial \phi(s)}{\partial s}$ for each membrane particle which is close to a solid particle.

In the algorithm (2.29)-(2.39), we can only use steps 1 to 4 for simulating the motion of cells in Poiseuille flow when there are no neutrally buoyant particles.

2.5.3   A scheme for flow modeled by the Stokes equations

In this subsection we present an IB method scheme for cell moving in fluid flows modeled by the stationary or non-stationary Stokes equations as follows:
$\mathbf{u}^0 = \mathbf{u}_0$ is given; for $n \geq 0$, $\mathbf{u}^n$ being known, we compute the approximate solution via the following fractional steps:

1. Update the position of the membrane by (2.24) and (2.25) and then compute the force $\mathbf{f}_B^n$ on the fluid/cell interface by (2.12) and (2.21) and obtain $\mathbf{f}^n = \mathbf{f}_p + \mathbf{f}_B^n$.

2. Solve

$$\begin{cases} \alpha\rho \int_\Omega \frac{\mathbf{u}^{n+1} - \mathbf{u}^n}{\triangle t} \cdot \mathbf{v}d\mathbf{x} + \mu \int_\Omega \nabla\mathbf{u} : \nabla\mathbf{v} - \int_\Omega p^{n+1}(\boldsymbol{\nabla} \cdot \mathbf{v})d\mathbf{x} = \mathbf{f}, \ \ \forall\mathbf{v} \in W_{0h}, \\ \int_\Omega q\boldsymbol{\nabla} \cdot \mathbf{u}^{n+1}d\mathbf{x} = 0, \ \ \forall q \in L_h^2, \\ \mathbf{u}^{n+1} \in W_{0h}, \ \ p^{n+1} \in L_h^2. \end{cases}$$

$$(2.40)$$

In the above scheme, $\alpha = 1$ for the non-stationary Stokes equations case and $\alpha = 0$ for the stationary case.

2.6 Numberical solutions of the subproblems

In the algorithm (2.29) - (2.39) and equation (2.40), there is a sequence of subproblems which can be solved by different numerical schemes. The elliptic problem (2.31) can be solved by a fast solver FISHPAK ([2]) and the saddle point problem (2.35) can be solved using a conjugate algorithm. For the advection subproblem (2.30) and the stokes problems (2.29) and (2.40), we shall discuss the related numerical methods in details in the following sections.

2.6.1 Numerical solution of the advection type subproblem

Clearly, the subproblem (2.30) can be solved by a *method of characteristics* (see, e.g., refs. [17] and [50] and the references therein). Here we follow the scheme for solving the general advection problem by a wave-like equation method (e.g., see [12] and [19] (Section 31)). It follows from that after translation and dilation on the time axis, each component of the velocity vector $\mathbf{u}$ and the configuration stress tensor A is a solution of a transport

equation of the following type:

$$\begin{cases} \dfrac{\partial \varphi}{\partial t} + (\mathbf{U} \cdot \boldsymbol{\nabla})\varphi = 0, \; in \; \Omega \times (0,1), \\[2mm] \varphi(0) = \varphi_0, \; \varphi = 0 \; on \; \Gamma \times (0,1), \end{cases} \tag{2.41}$$

The properties $\boldsymbol{\nabla} \cdot \mathbf{U} = 0$ and $\partial \mathbf{U}/\partial t = 0$ on $\Omega \times (0,1)$ imply that problem (2.41) is equivalent to the (formally) well-posed problem:

$$\begin{cases} \dfrac{\partial^2 \varphi}{\partial t^2} - \boldsymbol{\nabla} \cdot ((\mathbf{U} \cdot \boldsymbol{\nabla}\varphi)\mathbf{U}) = 0, \; in \; \Omega \times (0,1), \\[3mm] \varphi(0) = \varphi_0, \; \dfrac{\partial \varphi}{\partial t}(0) = -\mathbf{U} \cdot \boldsymbol{\nabla}\varphi_0, \\[3mm] \varphi = 0 \; on \; \Gamma \times (0,1), \; \dfrac{\partial \varphi}{\partial t} = 0 \; on \; \Gamma \times (0,1). \end{cases} \tag{2.42}$$

Solving the wave-like equation (2.42) by a classical finite element/time stepping method is quite easy since a variational formulation of (2.42) is given by

$$\begin{cases} \displaystyle\int_\Omega \dfrac{\partial^2 \varphi}{\partial t^2} v \, d\mathbf{x} + \int_\Omega (\mathbf{U} \cdot \boldsymbol{\nabla}\varphi)(\mathbf{U} \cdot \boldsymbol{\nabla}v) \, d\mathbf{x} = 0 \;\; \forall v \in W_0, \\[3mm] \varphi(0) = \varphi_0, \; \dfrac{\partial \varphi}{\partial t}(0) = -\mathbf{U} \cdot \boldsymbol{\nabla}\varphi_0, \\[3mm] \varphi = 0 \; on \; \Gamma \times (0,1), \end{cases} \tag{2.43}$$

with the test function space W_0 defined by

$$W_0 = \{v| \; v \in H^1(\Omega), \; v = 0 \; on \; \Gamma\}.$$

Let H_h^1 be a C^0- conforming finite element subspace of $H^1(\Omega)$ as discussed in, e.g., Ciarlet ([7],[8]). We define $W_{0h} = H_h^1 \cap W_0$; we suppose that $\lim_{h\to 0} W_{0h} = W_0$ in the usual element sense. Next, we define $\tau_1 > 0$ by $\tau_1 = \triangle t/Q$, where Q is a positive integer (and we discretize problem (2.43) by

$$\varphi^0 = \varphi_{0h}(\approx \varphi_0), \tag{2.44}$$

$$\begin{cases} \displaystyle\int_\Omega (\varphi^{-1} - \varphi^1)v \, d\mathbf{x} = 2\tau_1 \int_\Omega (\mathbf{U}_h \cdot \boldsymbol{\nabla}\varphi^0)v \, d\mathbf{x}, \; \forall v \in W_{0h}, \\[3mm] \varphi^{-1} - \varphi^1 \in W_{0h}, \end{cases} \tag{2.45}$$

and for $q = 0, 1, \cdots, Q - 1$,

$$
\begin{cases}
\varphi^{q+1} \in H_h^1, \ \varphi^{q+1} = g_h \quad on \ \Gamma^-, \\
\displaystyle\int_\Omega \frac{\varphi^{q+1} + \varphi^{q-1} - 2\varphi^q}{\tau_1^2} v \, d\mathbf{x} + \int_\Omega (\mathbf{U}_h \cdot \boldsymbol{\nabla}\varphi^q)(\mathbf{U}_h \cdot \boldsymbol{\nabla}v) \, d\mathbf{x} = 0 \quad \forall v \in W_{0h},
\end{cases} \tag{2.46}
$$

where, $\mathbf{U}_h$ and g_h are the approximates of $\mathbf{U}$ and g respectively.

Scheme (2.44)-(2.46) is a centered scheme which is formally second-order accurate with respect to space and time discretizations. To be stable, scheme (2.44)-(2.46) has to verify a condition such as

$$
\tau_1 \leq ch,
$$

with c of order of $1/||\mathbf{U}||$. Since the advection problem is decoupled from the rest, we can choose proper time step here so that the above condition is satisfied. If one uses the trapezoidal rule to compute the first and the third integrals in (2.46), the above scheme becomes explicit, i.e., φ^{q+1} is obtained via the solution of a linear system with diagonal matrix.

Scheme (2.44)-(2.46) does not introduce numerical dissipation, unlike the *upwinding* schemes commonly used to solve transport problems like (2.41).

2.6.2 Iterative solution of the Stokes type subproblem

2.6.2.1 The generalized Stokes problem

At each full time step of scheme (2.29)-(2.39), we have to solve twice the following generalized Stokes problem:

$$
\begin{cases}
\alpha\mathbf{u} - \nu\triangle\mathbf{u} + \nabla p = \text{ in } \boldsymbol{\Omega} \\[2mm]
\nabla \cdot \mathbf{u} = 0 \text{ in } \Omega \\[2mm]
\mathbf{u} = g_0 \text{ on } \Gamma_0, \ \nu\dfrac{\partial \mathbf{u}}{\partial n} - \mathbf{n}p = g_1 \text{ on } \Gamma_1
\end{cases}
\tag{2.47}
$$

with α and ν two positive parameters. Our main goal in this section is to discuss *iterative methods* for the solution of *generalized Stokes problem* (2.47).

2.6.2.2 Weak formulation of the generalized Stokes problem

We suppose that in the above (2.47), Ω is a bounded domain with $\alpha \geq 0$, $\nu > 0$, $\Gamma_0 \cap \Gamma_1 = \emptyset$, $\overline{\Gamma_0 \cup \Gamma_1} = \Gamma$; we suppose also that $\mathbf{f} \in (L^2(\Omega))^d$ (with d being the dimension), $g_0 \in \widetilde{g}_0 \mid_{\Gamma_0}$ with $\widetilde{g}_0 \in (H^1(\Omega))^d, g_1 \in (L^2(\Gamma_1))^d$. If (2.47) has a solution $\{\mathbf{u},\text{p}\}$ belonging to $(H^1(\Omega))^d \times L^2(\Omega)$, this solution verifies clearly

$$
\begin{cases}
\mathbf{u} \in V_{g_0}, \ p \in L^2(\Omega), \\[2mm]
\displaystyle\int_\Omega (\alpha\mathbf{u} \cdot \mathbf{v} + \nu\nabla\mathbf{u} : \nabla\mathbf{v})\, d\mathbf{x} - \int_\Omega p\nabla \cdot \mathbf{v}\, d\mathbf{x} = \\[2mm]
\qquad \displaystyle\int_\Omega \mathbf{f} \cdot \mathbf{v}\, d\mathbf{x} + \int_{\Gamma_1} g_1 \cdot \mathbf{v} d\Gamma, \forall \mathbf{v} \in V_0, \\[2mm]
\nabla \cdot \mathbf{u} = 0
\end{cases}
\tag{2.48}
$$

where

$$V_0 = \{\mathbf{v} \mid \mathbf{v} \in (H^1(\Omega))^d, \ \mathbf{v} = \mathbf{0} \ on \ \Gamma_0\}, \tag{2.49}$$

$$V_{g_0} = \{\mathbf{v} \mid \mathbf{v} \in (H^1(\Omega))^d, \ \mathbf{v} = g_0 \ on \ \Gamma_0\}. \tag{2.50}$$

$$\tag{2.51}$$

We define $L : (H^1(\Omega))^d \to \mathbb{R}$ as follows

$$L(\mathbf{v}) = \int_\Omega \mathbf{f} \cdot \mathbf{v} \, d\mathbf{x} + \int_{\Gamma_1} g_1 \cdot \mathbf{v} \, d\Gamma \tag{2.52}$$

The existence and uniqueness of the solution to equations (2.48) is proved in Mexicopaper.

2.6.2.3   A saddle-point interpretation of the generalized Stokes problem

As we shall see in a moment, any pair $\{\mathbf{u}, p\}$ solution of the generalized Stokes problem (2.47) can be viewed as a saddle-point of a well chosen Lagrangian functional, defined over $(H^1(\Omega))^d \times L^(\Omega)$. We associate with the generalized Stokes problem (2.47) the Lagrangian functional

$$\mathscr{L}(\mathbf{v}, q) = \frac{1}{2} \int_\Omega (\alpha \mid \mathbf{v} \mid^2 + \nu \mid \nabla \mathbf{v} \mid^2) \, d\mathbf{x} - L(\mathbf{v}) - \int_\Omega q \nabla \cdot \mathbf{v} \, d\mathbf{x}; \tag{2.53}$$

functional $\mathscr{L}$ is C^∞ on $(H^1(\Omega))^d \times L^2(\Omega)$. We have then the following:

Theorem 2.1. *Suppose that functional $\mathscr{L}$ has a saddle-point $\{\mathbf{u}, p\}$ over $V_{g_0} \times L^2(\Omega)$, i.e.,*

$$\begin{cases} \{\mathbf{u}, p\} \in V_{g_0} \times L^2(\Omega), \\ \mathscr{L}(\mathbf{u}, q) \le \mathscr{L}(\mathbf{u}, p) \le \mathscr{L}(\mathbf{v}, q), \forall \{\mathbf{v}, q\} \in V_{g_0} \times L^2(\Omega). \end{cases} \tag{2.54}$$

Then $\{\mathbf{u}, p\}$ is a solution of the Stokes problem (2.47). Conversely, any solution of (2.47) belonging to $V_{g_0} \times L^2(\Omega)$ is a saddle-point of $\mathscr{L}$ over $V_{g_0} \times L^2(\Omega)$.

2.6.2.4 A pre-conditioned conjugate gradient algorithm

If follows from Theorem 2.1 of the previous subsection that any solution of the generalized Stokes problem (2.47) is also a saddle-point over $V_{g_0} \times L^2(\Omega)$ of the Lagrangian functional defined by (2.53); conversely, any saddle-point of over $V_{g_0} \times L^2(\Omega)$ is also a solution of the Stokes problem (2.47). This equivalence property implies, among other things, that it makes sense to attempt solving problem (2.47) by solving the saddle-point problem (2.54), by a pre-conditioned conjugate gradient algorithm:

$$p^0 \in P \text{ is given;} \tag{2.55}$$

solve

$$\begin{cases} \mathbf{u}^0 \in V_{g_0}; \forall \mathbf{v} \in V_0, \\ \int_\Omega [\alpha \mathbf{u}^0 \cdot \mathbf{v} + \nu \nabla \mathbf{u}^0 : \nabla \mathbf{v}] \, d\mathbf{x} = L(\mathbf{v}) + \int_\Omega p^0 \nabla \cdot \mathbf{v} \, d\mathbf{x}, \end{cases} \tag{2.56}$$

and set

$$r^0 = \nabla \cdot \mathbf{u}^0. \tag{2.57}$$

Now solve

$$\begin{cases} -\triangle \phi^0 = r^0 \text{ in } \Omega, \\ \dfrac{\partial \phi^0}{\partial n} = 0 \text{ on } \Gamma_0, \phi^0 = 0 \text{ on } \Gamma_1, \end{cases} \tag{2.58}$$

if $\int_{\Gamma_i} d\Gamma > 0, \forall i = 0, 1$; or

$$\begin{cases} -\triangle \phi^0 = r^0 \text{ in } \Omega, \\ \dfrac{\partial \phi^0}{\partial n} = 0 \text{ on } \Gamma, \displaystyle\int_\Omega \phi^0 \, d\mathbf{x} = 0, \end{cases} \tag{2.59}$$

if $\Gamma_0 = \Gamma$; or

$$\begin{cases} -\triangle \phi^0 = r^0 \text{ in } \Omega, \\ \phi^0 = 0 \text{ on } \Gamma, \end{cases} \tag{2.60}$$

if $\Gamma_1 = \Gamma$. Then set

$$g^0 = \nu r^0 + \alpha \phi^0, \tag{2.61}$$

$$w^0 = g^0. \tag{2.62}$$

Then, for $n \geq 0$, assuming that p^n, r^n, g^n, w^n are known, compute $p^{n+1}, r^{n+1}, g^{n+1}, w^{n+1}$ as follows:

Solve:

$$\begin{cases} \bar{\mathbf{u}}^n \in V_{g_0}; \forall \mathbf{v} \in V_0, \\ \displaystyle\int_\Omega [\alpha \bar{\mathbf{u}}^0 \cdot \mathbf{v} + \nu \nabla \bar{\mathbf{u}}^n : \nabla \mathbf{v}] \, d\mathbf{x} = \int_\Omega w^n \nabla \cdot \mathbf{v} \, d\mathbf{x}, , \end{cases} \tag{2.63}$$

and set

$$\bar{r}^n = \nabla \cdot \bar{\mathbf{u}}^n. \tag{2.64}$$

Compute

$$\rho_n = \int_\Omega r^n g^n \, d\mathbf{x} \bigg/ \int_\Omega \bar{r}^n w^n \, d\mathbf{x}, \tag{2.65}$$

and then

$$p^{n+1} = p^n - \rho_n w^n. \tag{2.66}$$

$$r^{n+1} = r^n - \rho_n \bar{r}^n. \tag{2.67}$$

Solve, next,

$$\begin{cases} -\triangle \bar{\phi}^n = \bar{r}^n \text{ in } \Omega, \\ \dfrac{\partial \bar{\phi}^n}{\partial n} = 0 \text{ on } \Gamma_0, \bar{\phi}^n = 0 \text{ on } \Gamma_1, \end{cases} \tag{2.68}$$

if $\int_{\Gamma_i} d\Gamma > 0, \forall i = 0, 1$; or

$$\begin{cases} -\triangle \bar{\phi}^n = \bar{r}^n \text{ in } \Omega, \\ \dfrac{\partial \bar{\phi}^n}{\partial n} = 0 \text{ on } \Gamma, \int_\Omega \bar{\phi}^n \, d\mathbf{x} = 0, \end{cases} \tag{2.69}$$

if $\Gamma_0 = \Gamma$; or

$$\begin{cases} -\triangle \bar{\phi}^n = \bar{r}^n \text{ in } \Omega, \\ \bar{\phi}^n = 0 \text{ on } \Gamma, \end{cases} \tag{2.70}$$

if $\Gamma_1 = \Gamma$. Then, compute

$$g^n + 1 = g^n - \rho_n(\nu \bar{r}^n + \alpha \bar{\phi}^n). \tag{2.71}$$

29

If $\int_\Omega r^{n+1}g^{n+1}\,d\mathbf{x}/\int_\Omega r^0 g^0\,d\mathbf{x} \leq \epsilon$, take $p = p^{n+1}$; else, compute

$$\gamma_n = \int_\Omega r^{n+1}g^{n+1}\,d\mathbf{x}/\int_\Omega r^n g^n\,d\mathbf{x}, \tag{2.72}$$

and update w^n by

$$w^{n+1} = g^{n+1} + \gamma_n w^n. \tag{2.73}$$

Do $n = n + 1$ and return to (2.63).

In the above algorithm (2.55)-(2.73), when solving the Stokes-type subproblem of the operator splitting for the Navier-Stokes equations, we have $\nu = 0$, and $\mathbf{f} = 0$; we set $\alpha = 0$, $\nu = \mu$ when we are solving the stationary Stokes equations and $\mathbf{f}$ is the sum of the external force from the cell membrane calculated by the immersed boundary method and the flow pressure gradient; when solving the non-stationary Stokes equations, $\alpha = \dfrac{\rho}{\triangle t}$ is non-zero.

2.7   Cell with higher interior viscosity

The fluids separated by the cell membrane can have different properties, for example: the viscosity of the plasma and that of the cytoplasm are different. In the system considered in this dissertation, we assume that the densities of the cytoplasm of RBC and the plasma are same. For most cases considered in this dissertation, the viscosities of the cytoplasm and that of the suspending plasma are the same. But we have also considered some cases with different viscosities inside and outside of the RBC membrane.

2.7.1   Viscosity function across the cell membrane

To deal with the cases with higher interior viscosity, the viscosity is treated as a smoothing function instead of a piecewise constant function across the cell membrane [33, 66]. In

this dissertation, we treat different viscosities when crossing the cell membrane via a Heaviside function [66] defined as

$$\theta(d) = \begin{cases} 0, & d < -2h \\ \dfrac{1}{2}(1 + \dfrac{d}{2h} + \dfrac{1}{\pi}sin\dfrac{\pi d}{2h}), & -2h \le d \le 2h \\ 1, & d > 2h \end{cases} \tag{2.74}$$

where d denotes the shortest distance to the cell membrane from the fluid node, negative means the node is outside the membrane. If the node is close to two or more membrane segments, the distance is taken as the smallest one. Then the viscosity function can be defined as:

$$\mu(\mathbf{x}) = \mu_{out} + (\mu_{in} - \mu_{out})\theta[d(\mathbf{x})] \tag{2.75}$$

where μ_{out} and μ_{in} are the viscosities outside and inside of the cell, respectively.

2.7.2 A new scheme in handling the non-constant viscosity

As mentioned in section 2.1, when the viscosity contrast between the viscosity of the interior and exterior fluid is 1, the term $\nabla \cdot [2\mu(\mathbf{x}, t)D(\mathbf{u})]$ can be replaced with $\mu\triangle\mathbf{u}$. In addition to making the function look neater, the replacement also brings great convenience in solving the Navier-Stokes equations. When the parameter μ is constant, the diffusion problem (2.31) can be solved by the matrix-free fast solver from FISHPAK by Adams *et al.*[2]. But when μ is non-constant, the fast solver can't handle it. We have to apply other numerical schemes such as the red-black SOR method, which is not as efficient as the fast solver.

With non-constant viscosity $\mu(\mathbf{x}, t)$, the weak formulation of equation (2.31) is:

$$
\begin{cases}
\rho \int_\Omega \dfrac{\mathbf{u}^{n+3/6} - \mathbf{u}^{n+2/6}}{\triangle t} \cdot \mathbf{v} \, d\mathbf{x} + 2 \int_\Omega \mu(\mathbf{x}, t) \mathbf{D}\mathbf{u}^{n+2/6} : \mathbf{D}\mathbf{v} \, d\mathbf{x} = \int_\Omega \mathbf{f}^{\mathbf{n+1/6}} \cdot \mathbf{v} \, d\mathbf{x} \\[2ex]
\forall \mathbf{v} \in W_{0,h}; \quad \mathbf{u}^{n+3/6} \in W_{0,h}.
\end{cases}
\tag{2.76}
$$

Due to the non-constant coefficient $\mu(\mathbf{x}, t)$, the fast solver FISHPAK cannot be applied to solve the diffusion equation. A red-black SOR method was employed as the numerical solver for the above equation (2.76). In order to apply the fast solver, a new scheme is developed for the diffusion equation as follows: by plugging equation (2.75) into the above equation (2.76), and move the $(\mu_{in} - \mu_{out})\theta[d(\mathbf{x})]$ part to the right hand side of the equation. Then equation (2.31) becomes:

$$
\begin{cases}
\rho \int_\Omega \dfrac{\mathbf{u}^{n+3/6} - \mathbf{u}^{n+2/6}}{\triangle t} \cdot \mathbf{v} \, d\mathbf{x} + \mu_{in} \int_\Omega \nabla \mathbf{u}^{n+3/6} : \nabla \mathbf{v} \, d\mathbf{x} = \\[2ex]
\quad \int_\Omega \mathbf{f}^{\mathbf{n+1/6}} \cdot \mathbf{v} \, d\mathbf{x} - 2 \int_\Omega (\mu_{in} - \mu_{out})(\mathbf{x}) \theta[d(\mathbf{x})] \mathbf{D}(\mathbf{u}^{n+2/6}) : \mathbf{D}(\mathbf{v}) \, d\mathbf{x} \\[2ex]
\forall \mathbf{v} \in W_{0,h}; \quad \mathbf{u}^{n+3/6} \in W_{0,h}.
\end{cases}
\tag{2.77}
$$

Here C denote the part of domain with the cell. Note that the θ function is non-zero only in a very small region around the RBC. So the new part on the right hand side is not costly from computational point of view. Now, equation (2.77) again is the diffusion problem with constant parameters and can be solved by the fast solver.

Chapter 3

Single RBC in flows

Different flow models (Navier-Stokes flow, stationary Stokes flow, and the non-stationary Stokes flow) have been used to model the fluid flow under different situations. Among which the Navier-Stokes (NS) model and the stationary-Stokes (Stokes) model receive the most popularity. In this chapter, the motions of a single RBC in blood flows under the two different flow models are analyzed. As a validation test of the fluid model and the numerical scheme, the steady inclination angles of the tank-treading motions of RBCs under two different degrees of confinement in shear flow are compared with the simulation results in [28]. Then the comparison of motions of a soft RBC in Poiseuille flow using two different flow models is studied in detail.

3.1 Validation of models

The validation for the elastic spring model is done in [52]. By minimizing the total energy we achieve the equilibrium shapes of cells of different swelling ratio s^*. We further
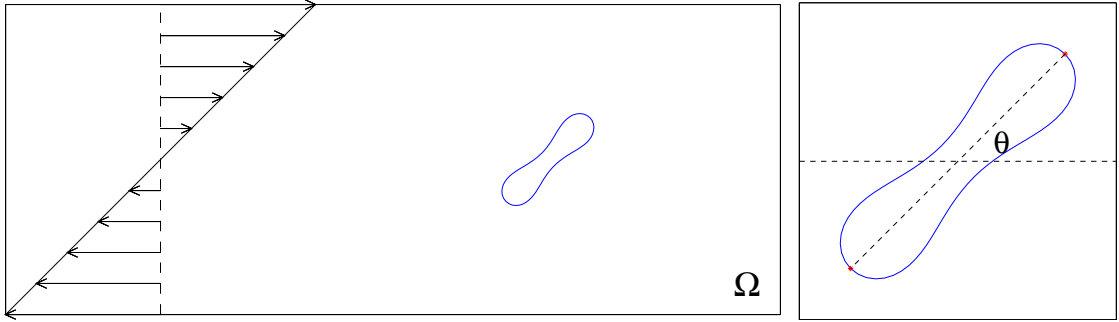
Figure 3.1: An schematic diagram of a single red blood cell in shear flow with the computational domain Ω, the inclination angle θ is defined as the angle between the cell long axis and the horizontal line.

validate the NS model and the Stokes model by comparing the steady inclination angles of tank-treading under two different degrees of confinement. A two-dimensional vesicle model is used by Kaoui to analyze the effect of confinement on the tank-treading motion in [28]. The inclination angle is defined as the angle between the cell long axis and the horizontal line as shown in Figure 3.1. The degree of confinement is defined as the ratio of the cell's effective radius R_0 to the channel half height w. To produce a shear flow, a Couette flow driven by two walls at the top and bottom which have the same speed but move in directions opposite to each other is applied to the suspension. Different shear rate can be obtained by adjusting the wall speed. In addition, periodic conditions are imposed at the left and right boundary of the domain.

We present the results of simulation of a single RBC suspended in a linear shear flow with shear rate $\gamma = 500 s^{-1}$. The values of parameters for modeling cells are as follows: the bending constant is $k_b = 5 \times 10^{-10} \mathrm{N \cdot m}$, the spring constant is $k_l = 5 \times 10^{-8} \mathrm{N \cdot m}$ and the penalty coefficient is $k_s = 10^{-5} \mathrm{N \cdot m}$. The cells are suspended in blood plasma which has a density $\rho = 1.00 \mathrm{g/cm^3}$ and a dynamical viscosity $\mu = 0.012 \mathrm{g/(cm \cdot s)}$. The viscosity ratio

which describes the viscosity contrast of the inner and outer fluid of the RBC membrane is fixed at $\lambda = 1.0$. The Reynolds number is defined by $Re = \rho U H / \mu$, where $U = \gamma \times L$ is multiplication of the shear rate of the the shear flow and the channel width. The capillary number is defined by $Ca = \mu G_r R_0^3 / B$, where G_r, R_0, and B represent the shear rate of fluid flow, the effective radius of the cell, and the bending coefficient, respectively. The dimensions of the computational domain are 112×7 µm^2 and 112×14 µm^2 . The two degrees of confinement are 0.8 for the narrower domain and 0.4 for the wider domain, respectively. The grid resolution for the computational domain is 80 grid points per 10 µm. The time step $\triangle t$ is 10^{-5} ms. The initial velocity of the fluid flow is zero everywhere and the initial positions of the mass center of the cell are $(56, 3.5)$ and $(56, 7)$ for the narrower domain and the wider domain, respectively. For comparison reason, the channel capillary number in this section is set as $Ca = 0.455$ as in [28].

During the tank-treading motion, the cell remains its shape while the cell membrane circles around. As in Figure 3.2, RBCs of different swelling ratio undergo almost no deformation at the final steady tank-treading state from their relaxed shapes. This is also mentioned in [28]. In Figure 3.3, the shapes and steady inclination angle of cells under the two different flow models are plotted. The plots overlap each other, meaning that the steady inclination angle are the same under the two different flow models. The steady inclination angle of the RBC as a function of swelling ratio under two different degrees of confinement is plotted in Figure 3.4 together with the results of Kaoui *et al.* ([28]). The results show good agreement with each other. When swelling ratio is the same, the inclination angle is smaller when the degree of confinement is bigger. When the degree of confinement is the same, the inclination angle increases as the swelling ratio s^* increases.

ratio
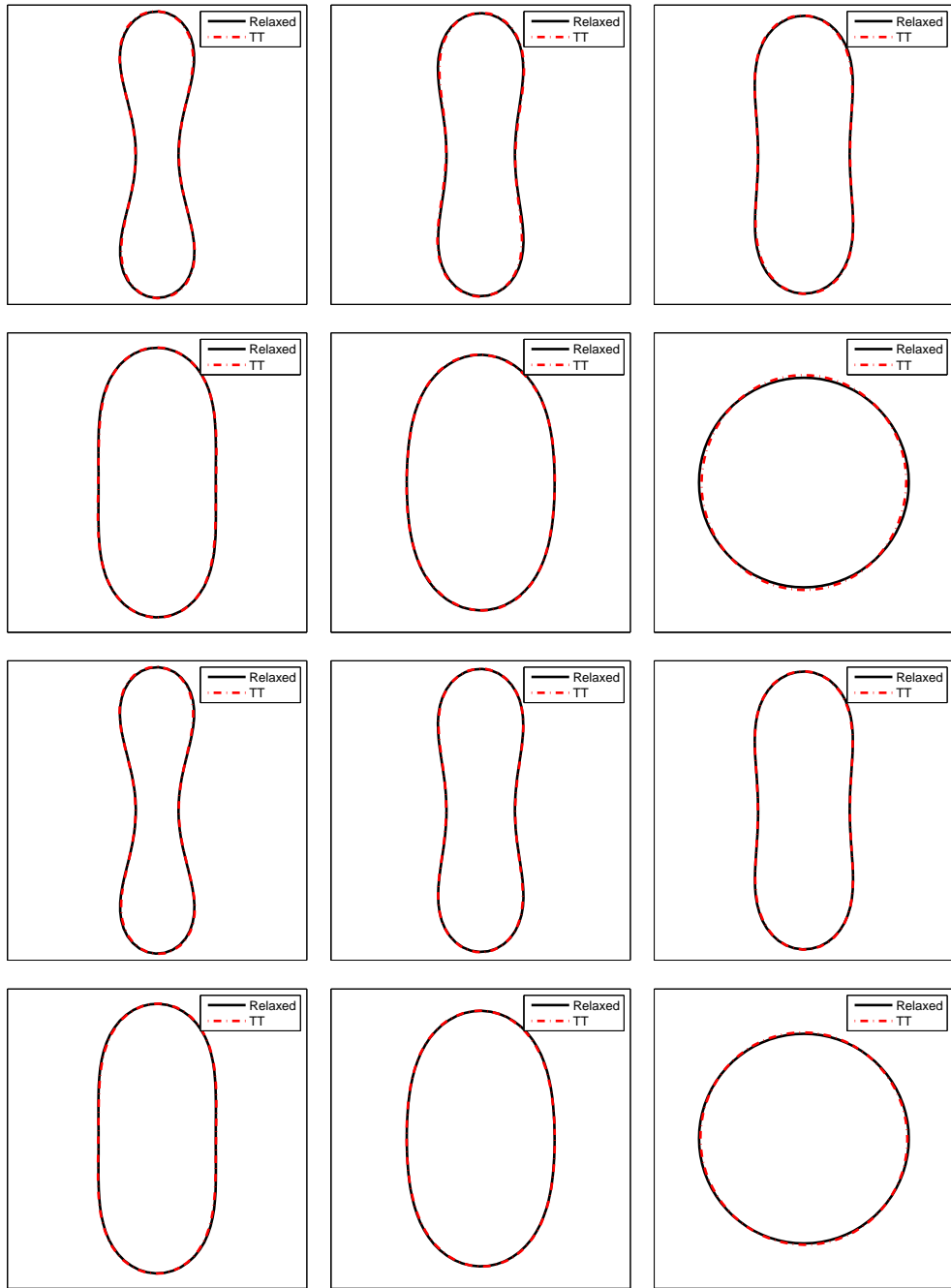
Figure 3.2: Comparison between relaxed cell shapes and tank-treading shapes of RBCs with swelling ratio $s^* = 0.481, 0.6, 0.7, 0.8, 0.9, 1.0$. Degrees of confinement is 0.4 for the upper two rows and 0.8 for the lower two rows.
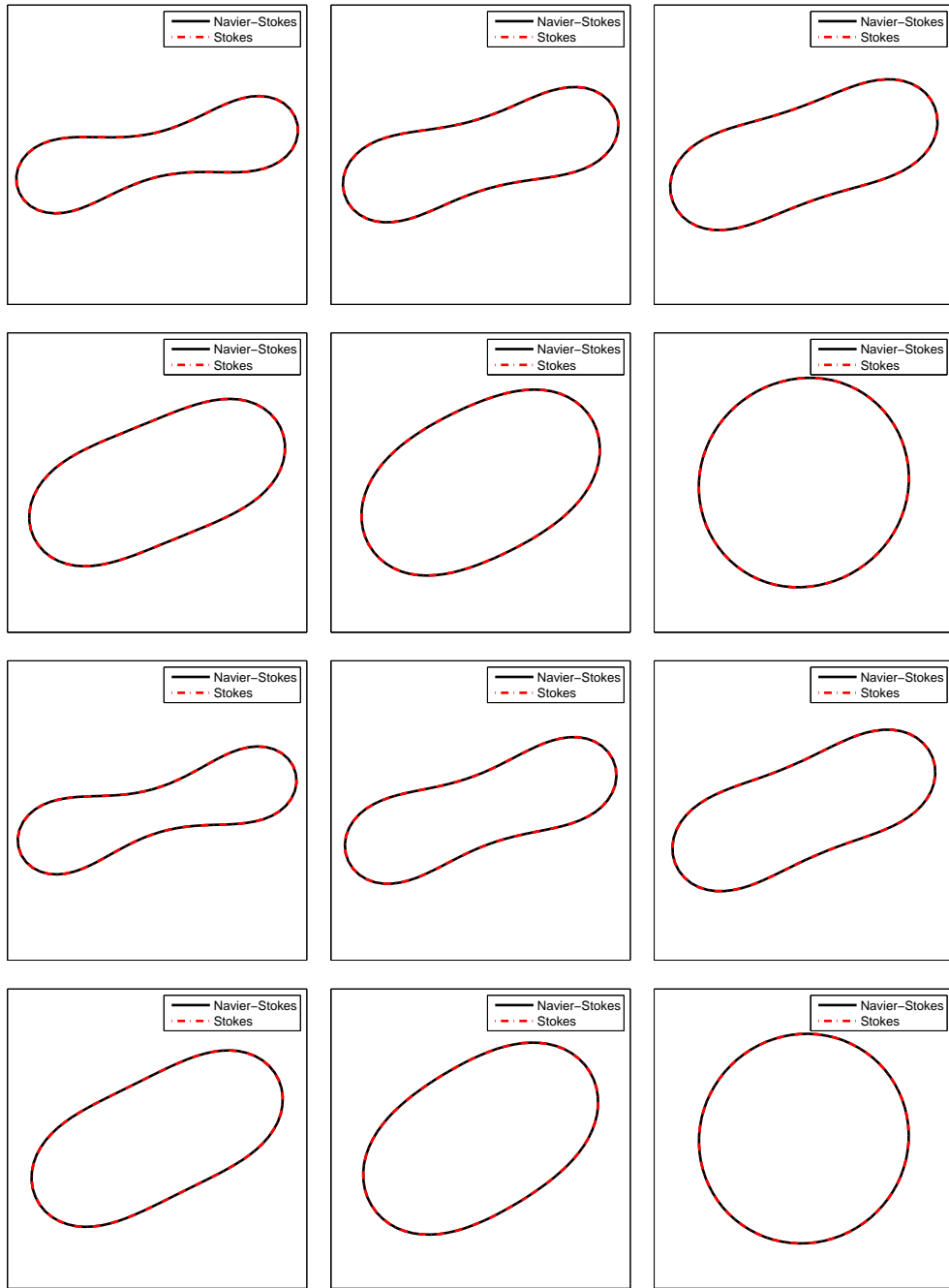
Figure 3.3: The equilibrium inclination angle of a single cell with swelling ratio s^*=0.481, 0.6, 0.7, 0.8, 0.9, 1.0. Degree of confinement is R_0/w=0.8 for top two rows and 0.4 for the bottom two rows.
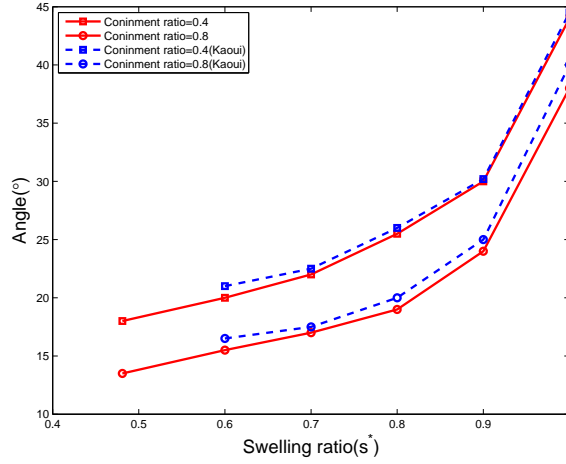
Figure 3.4: Steady inclination angle as a function of the cell swelling ratio for two degrees of confinement R_0/w=0.4 and 0.8.

3.2   Motions of a single RBC in Poiseuille flows

The deformation and lateral migration of a single cell in two dimensional Poiseuille flows using two different flow models have been investigated in this section. The values of parameters for modeling cells are as follows: The bending constant is $kb = 5 \times 10^{-10}$ Nm, the spring constant is $kl = 5 \times 10^{-8}$ Nm, and the penalty coefficient is $ks = 10^{-5}$ Nm. The cells are suspended in blood plasma which has a density $\rho = 1.00$ g/cm^3 and a dynamical viscosity $\mu = 0.012$ g/(cms). The viscosity ratio is $\lambda = 1$ throughout this section. The computational domain is a two-dimensional horizontal channel. To obtain a Poiseuille flow, a constant pressure gradient is prescribed as a body force. In addition, periodic conditions are imposed at the left and right boundaries of the domain. The Reynolds number is defined by $Re = \rho U H/\mu$, where U is the maximum velocity at center of the channel without RBC suspending in it. The capillary number is defined by $Ca = \mu G_r R_0^3/B$, where Gr, R_0, and B represent the shear rate at the top or bottom of fluid flow, the effective radius of

the cell, and the bending coefficient, respectively. The dimensions of the computational domain are 100×10 µm^2. The grid resolution for the computational domain is 64 grid points per 10 μm. The time step $\triangle t$ is 10^{-5} ms. The initial velocity of the fluid flow is a parabolic velocity field and the initial positions of the mass center of the cell are either at the channel center $(50, 5)$ or on side of the channel at $(50, 3)$. The pressure gradient is set as a constant such that a Poiseuille velocity profile can be reached. When the maximum velocity of the flow without cell suspending in it is 1.8 cm/s and the bending constant is $1k_b$, the corresponding Reynolds number is 0.1 and the capillary number is $Ca = 6.55$. A higher bending constant or a faster u_{max} at the centerline can lead to a bigger capillary number. The comparison between the Navier-Stokes flow model and the Stokes flow model is done based on the same capillary number.

3.2.1   The deformation-dominated motions of RBCs in Poiseuille flows

When the RBC is soft with a relatively lower bending constant, it has little resistance to external force and deforms easily. In this subsection, the deformation dominated motion of a single RBC in bounded Poiseuille flow is investigated using both the NS and the Stokes model. The bending constant used in this subsection is $0.1k_b$ and $1k_b$. The initial positions of the mass center of the cell are either at the channel center $(50, 5)$ or on side of the channel at $(50, 3)$. When the mass center is at center (resp. on the side) of the channel, the initial inclination angle is set as $\phi_0 = 45°$ (resp. $\phi_0 = 0°$). The final equilibrium shapes, the deformations during the migration of RBCs under two different flow models are compared.
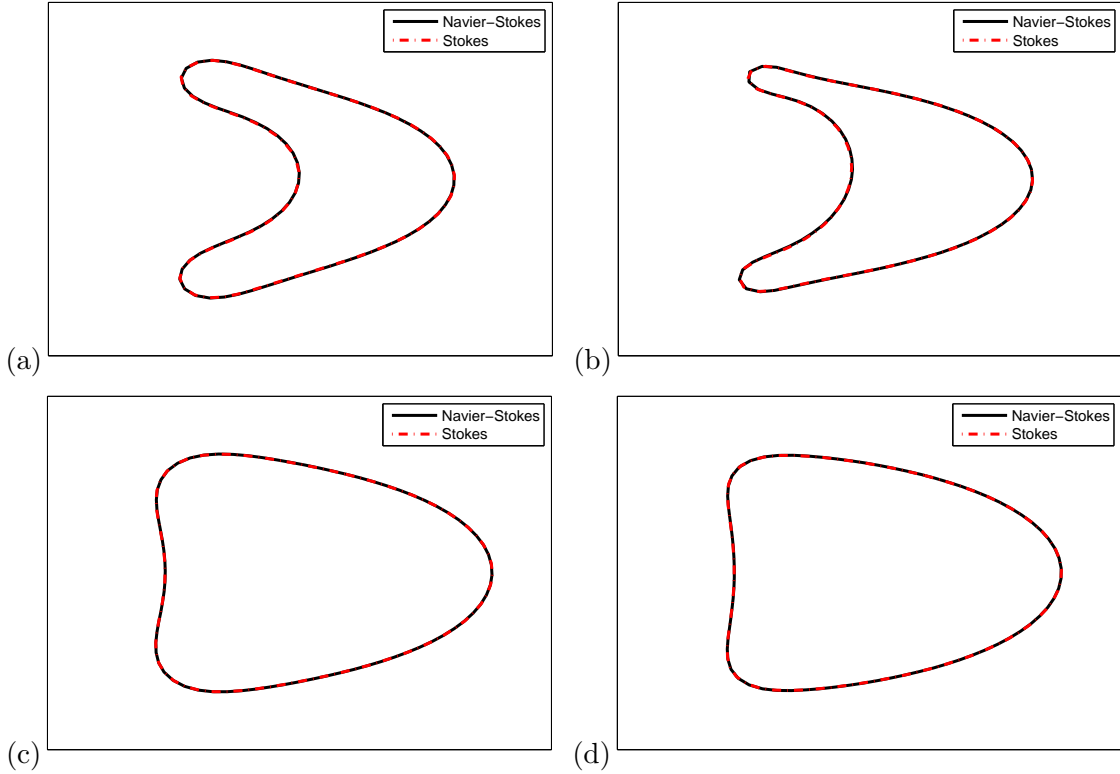
Figure 3.5: The final equilibrium shape of RBCs with $0.1k_b$ in bounded Poiseuille flow. Cell swelling ratio is $s^* = 0.481$ (a,b) and 0.9 (c,d) , and the flow capillary number $Ca = 0.65$ (a,c) and 3.27 (b,d), respectively.

3.2.1.1 Equilibrium shape of a soft RBC in Poiseuille flows

The final equilibrium shape of RBC in bounded two-dimensional Poiseuille flows is studied by numerical simulation. For the Navier-Stokes flow, it is well known that the following factors are important in determining the shape of single RBC in Poiseuille flows: the swelling ratio (S^*), the maximum velocity at the center line of fluid flow (u_{max}), the fluid viscosity (μ), the membrane bending stiffness of a RBC (k_b), and the height of the microchannel (H). In [57], it is reported that for stiff RBCs, initial inclination angle (ϕ_0)
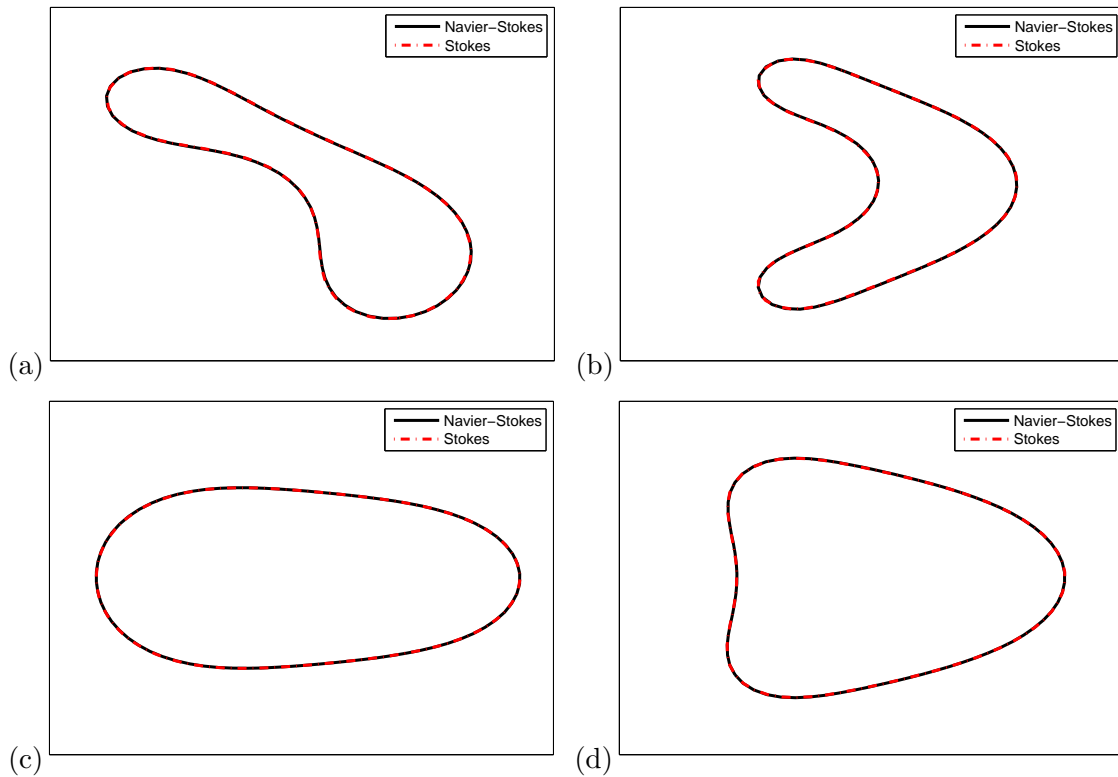
Figure 3.6: The final equilibrium shape of RBCs with $1k_b$ in bounded Poiseuille flow. Cell swelling ratio is $s^* = 0.481$ (a,b) and 0.9 (c,d) , and the flow capillary number $Ca = 0.065$ (a,c) and 0.33 (b,d), respectively.

can also affect the final equilibrium shape. The final equilibrium shape of a single RBC (with swelling ratio $S^* = 0.481$ or 0.9, bending constant $0.1k_b$ or $1k_b$) in bounded Poiseuille flow (with maximum flow speed $u_{max} = 1.8$ cm/s or 9.0 cm/s) are presented in Figure 3.5 and Figure 3.6. In all the cases, the cell undergo large deformation and doesn't maintain its relaxed state shape anymore. When capillary number is high (bending is weak or u_{max} is big), the cell reaches a parachute equilibrium state as in Figure 3.5(a)-(d) and Figure

3.6(b),(d). When capillary number is low, the biconcave-shaped cell reaches a slipper-like equilibrium shape (Figure 3.6(a)) and the elliptical-shaped cell ends with a bullet-like equilibrium shape (Figure 3.6(c)). In all of the cases discussed above in Figure 3.5 and Figure 3.6, the final equilibrium shapes of cells under Navier-Stokes flow and the stationary Stokes flow are the same when the capillary number is the same.

3.2.1.2 Deformations of a soft RBC in Poiseuille flows

In this subsection, the deformation of a single RBC in Poiseuille flow is studied. Two motions of oscillation and vacillating breathing (also called swing; the long axis undergoes oscillation while the cell shape displays breathing) of the RBC are observed for the bi-concave cell with bending equal to $1k_b$ and capillary number equal to 6.55. A bullet-like equilibrium shape is obtained for the elliptical shaped cell with bending equal to $1k_b$ and capillary number equal to 6.55. The histories of cell mass center under two different flow models are plotted in Figure 3.7 and Figure 3.8. The trajectories of the cell mass center under the two flow models agree with each other well. The initial inclination angle of the biconcave cell for the Navier-Stokes case is set as $-45°$ and the RBC shows a symmetric behavior comparing to the motions under the Stokes flow model. The snapshots of the de-tails of the motions are plotted in Figure 3.9 and Figure 3.10. An asterisk and a circle mark are put on the cell membrane to track the trajectory of the same point on the membrane for both flow models respectively. The snapshots in Figures 3.9 and 3.10 confirm again that the deformation dominated motions of a RBC in Poiseuille flow under NS model and Stokes model agree with each other. When capillary number $Ca = 6.55$, both the elliptic and biconcave cell shows a damped oscillation, during which the mass center oscillates up and down the channel center line with the magnitudes of oscillation keeps decreasing. The
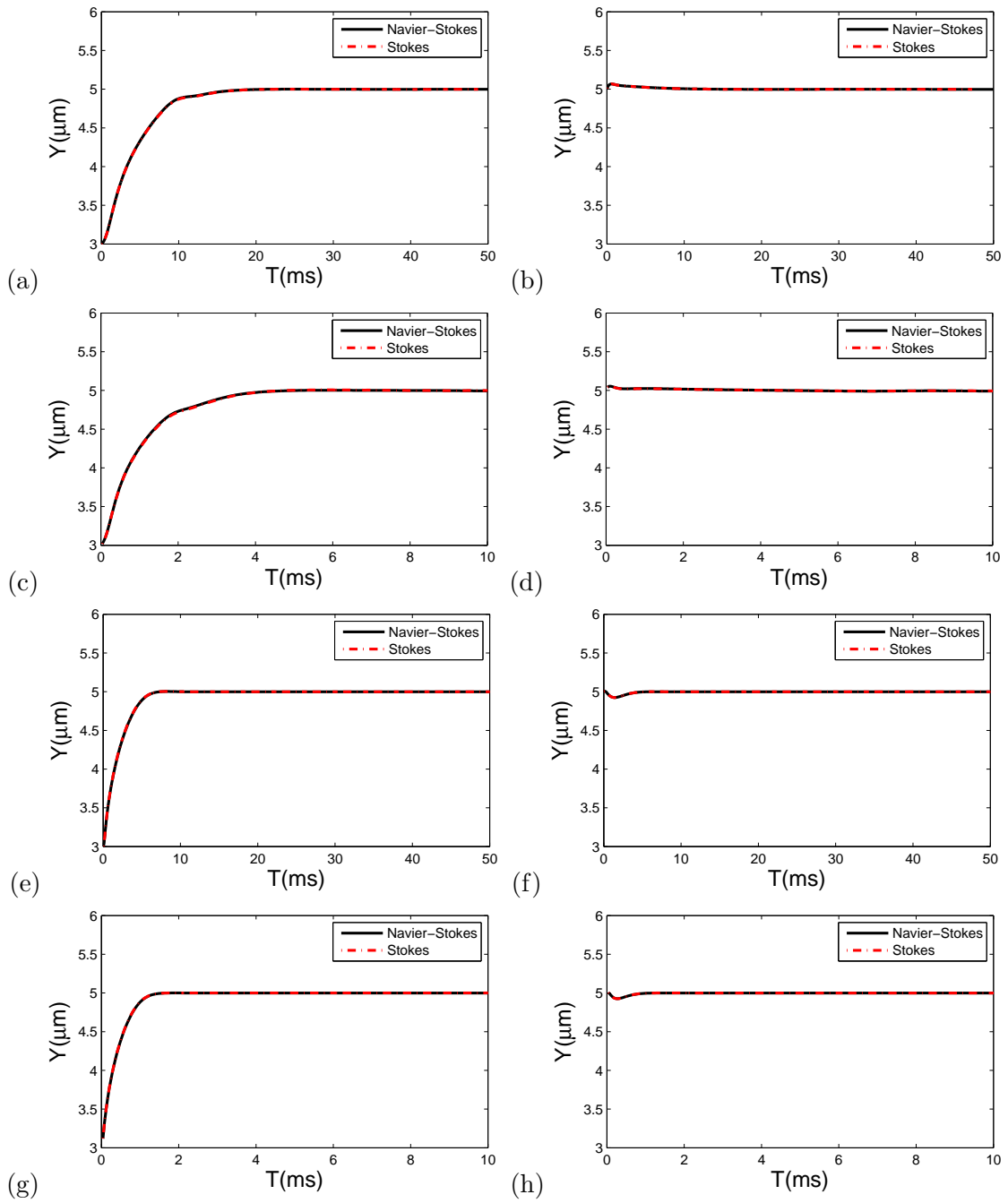
Figure 3.7: The trajectory of cell mass center with cell bending constant $0.1k_b$. The swelling ratio is 0.481 (a,b,c,d) and 0.9 (e,f,g,h) and the capillary number is 0.65 (a,b,e,f) and 3.27 (c,d,g,h), respectively.
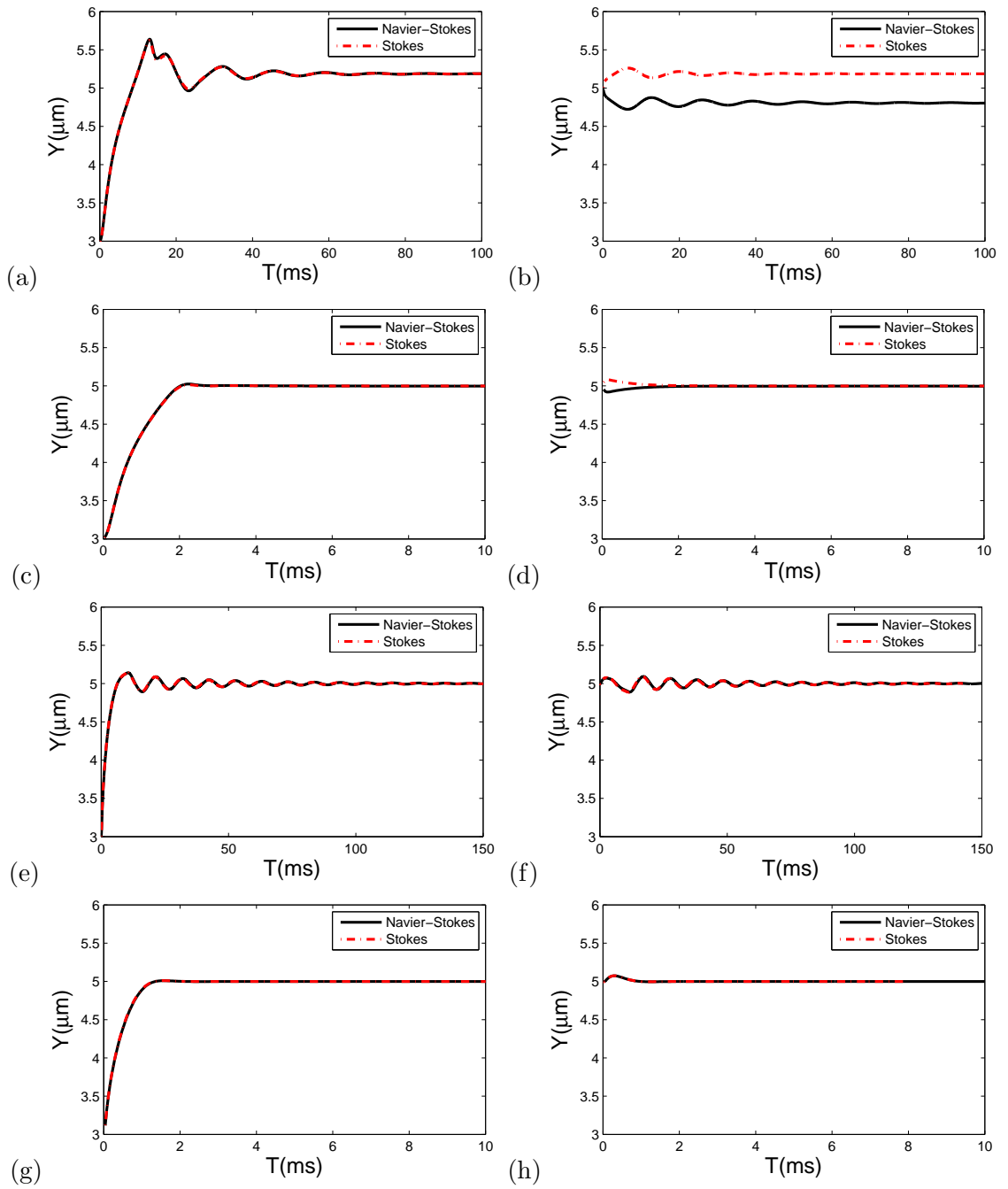
Figure 3.8: The trajectory of cell mass center with cell bending constant $1k_b$. The swelling ratio is 0.481 (a,b,c,d) and 0.9(e,f,g,h) and the capillary number is 0.065 (a,b,e,f) and 0.327 (c,d,g,h), respectively.
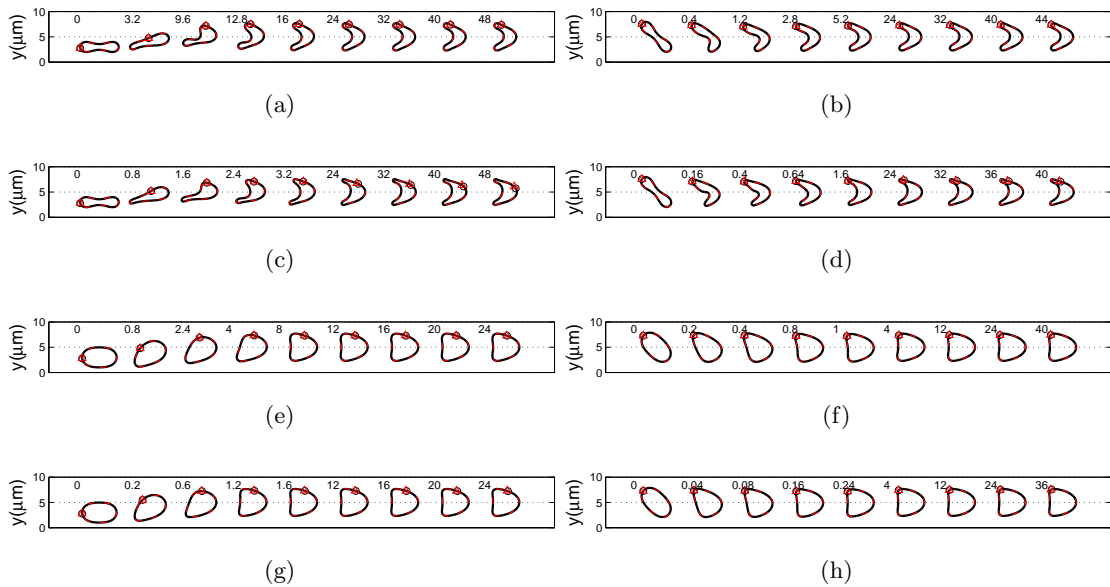
Figure 3.9: The snapshots of motions of RBC under two different flow models with bending constant $0.1k_b$. The cell swelling ratio is 0.481 in the upper four plots and 0.9 in the lower four plots. The capillary number are 0.65 and 3.27 for the plots in row one,three and two,four respectively. the circle, triangle denotes the same mark on the cell membrane.
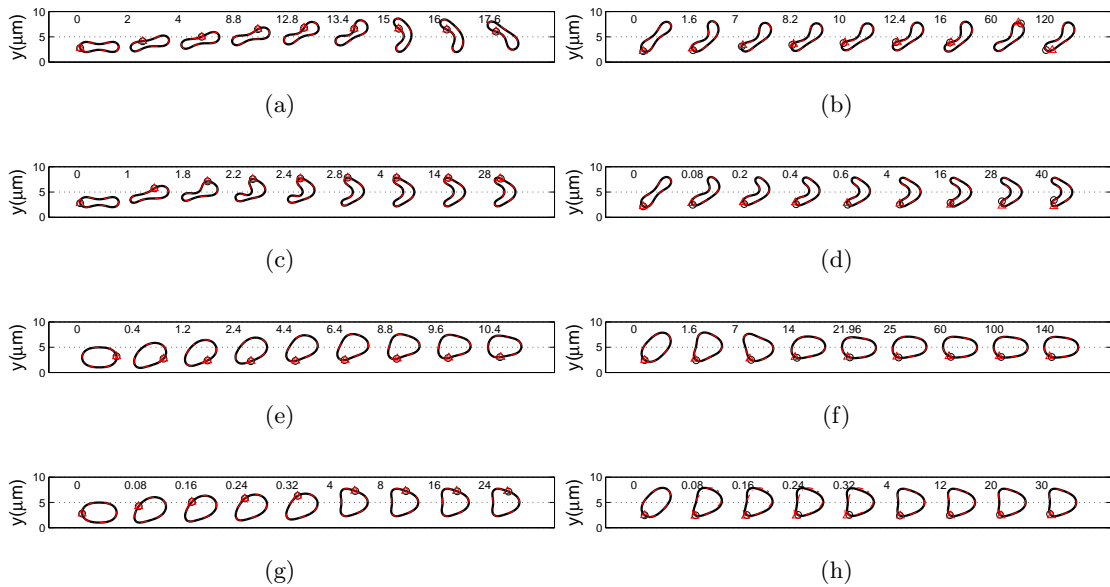
Figure 3.10: The snapshots of motions of RBC under two different flow models with bending constant $1k_b$. The cell swelling ratio is 0.481 in the upper four plots and 0.9 in the lower four plots. The capillary number are 0.065 and 0.327 for the plots in row one,three and two,four respectively. the circle, asterisk denotes the same mark on the cell membrane.
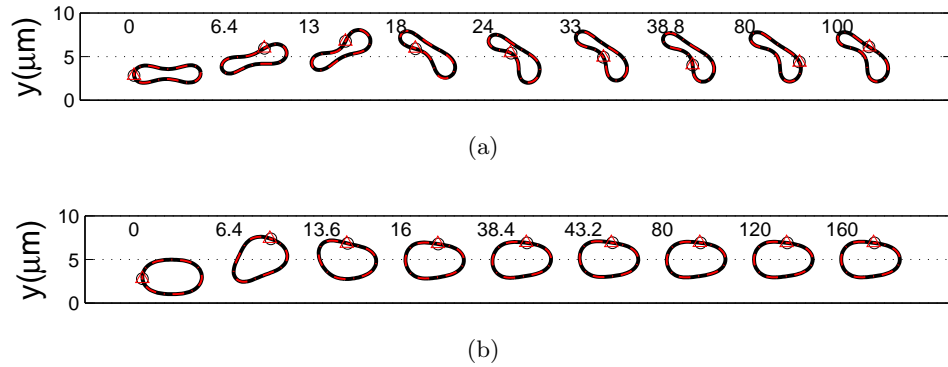
Figure 3.11: The snapshots of damped oscillations of RBC under two different flow models with bending constant $1k_b$ in flow. The circle, asterisk denotes the same mark on the cell membrane.

biconcave cell shows a vacillating breathing motion (the long axis undergoes oscillation while the cell shape bends back and forth) and the elliptic cell shows a 'swimming' motion (the tip of the cell leads the motion and the tail swings). Two detailed snapshots of such motions are shown in Figure 3.11.

3.2.1.3 Motions of RBC in faster flow

In this subsection, we increase the Reynolds number from 0.1 and 0.5 as in the previous subsection to $1, 2$, and 3. The bending constant of cells varies from $1k_b$ to $10k_b$. In Figure 3.12 and Figure 3.13, the history of migration of cell mass center under two different flow models are plotted together for comparison. And the final equilibrium shape of cells are also compared in Figure 3.14 and Figure 3.15. As shown in Figure 3.14 and Figure 3.15, at final equilibrium state, both the elliptical and the biconcave shaped cell cell undergo large deformation comparing to their relaxed states. It is clear that from the comparisons

47
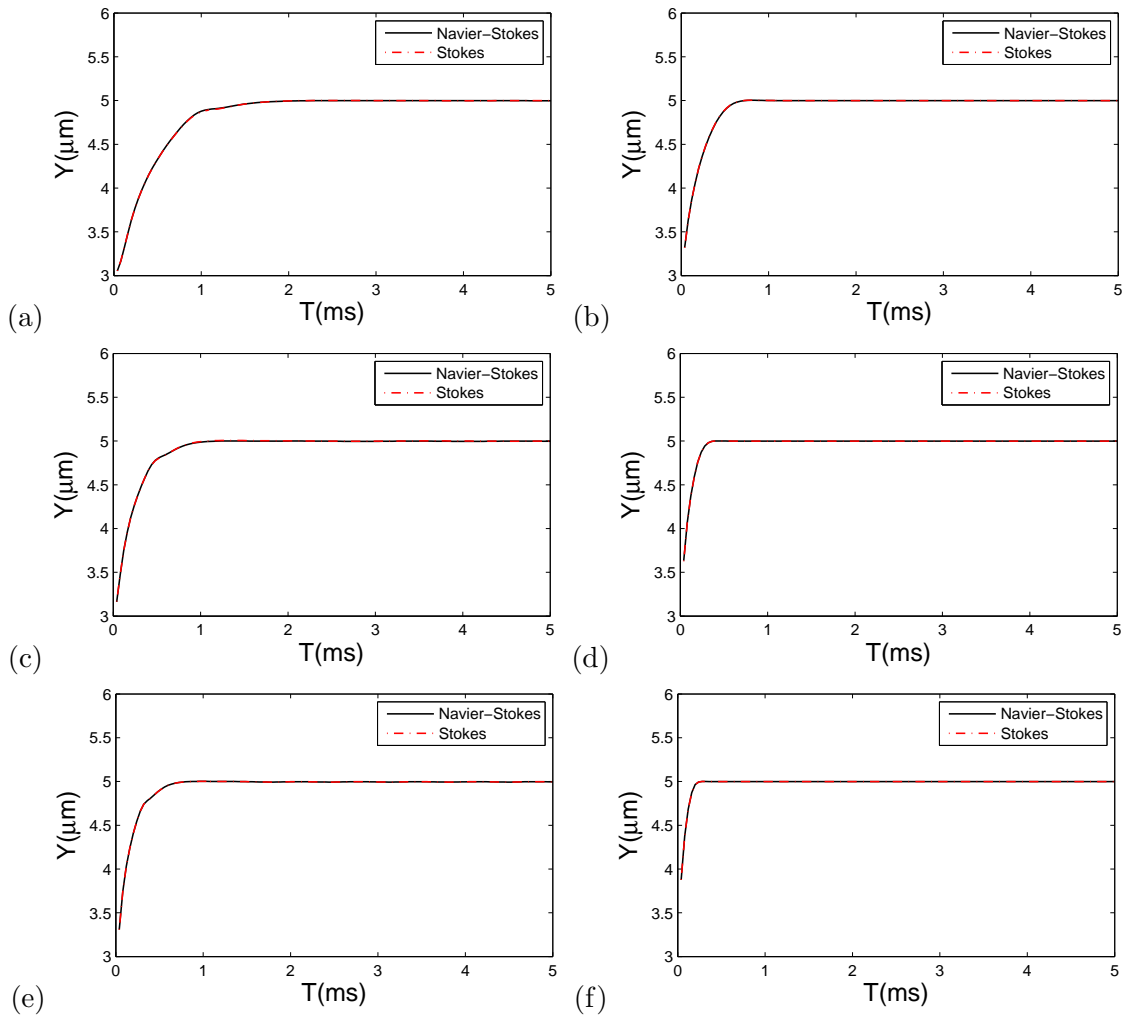
Figure 3.12: Trajectory of cell mass center with cell swelling ratio $s^* = 0.481$ (a,c,e) and 0.9 (b,d,f). The maximum flow speed is $u_{max} = 18, 36$, and 54 cm/s for three rows, respectively. Bending constant is $1k_b$.

in Figure 3.12 through Figure 3.15, the motions of RBC under Stokes flow model matches with motions of that under NS flow model in all the cases . Thus raises the question: is the speed of the flow really a good factor in determining whether to choose the Navier-Stokes or the Stokes flow as the fluid model?
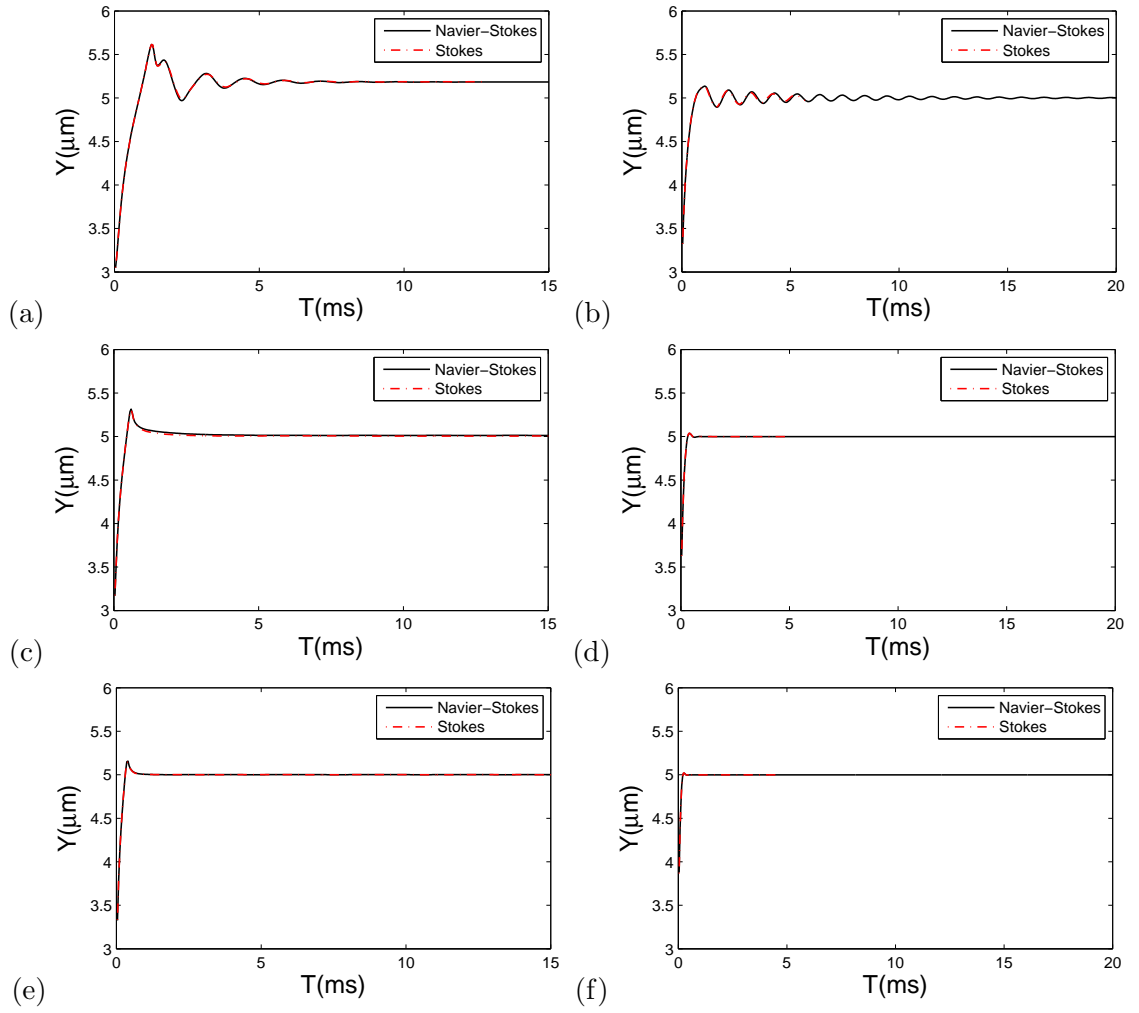
Figure 3.13: Trajectory of cell mass center with cell swelling ratio $s^* = 0.481$ (a,c,e) and 0.9 (b,d,f). The maximum flow speed is $u_{max} = 18, 36$, and $54\,\text{cm/s}$ for three rows, respectively. Bending constant is $10k_b$.

3.3 Motions of a stiffer cell in Poiseuille flows

In this section, the bending constant of the cells is set as $100k_b$. The Reynolds number of the NS flow model is $1, 2$, or 3 and the corresponding capillary number $0.65, 0.33$, or
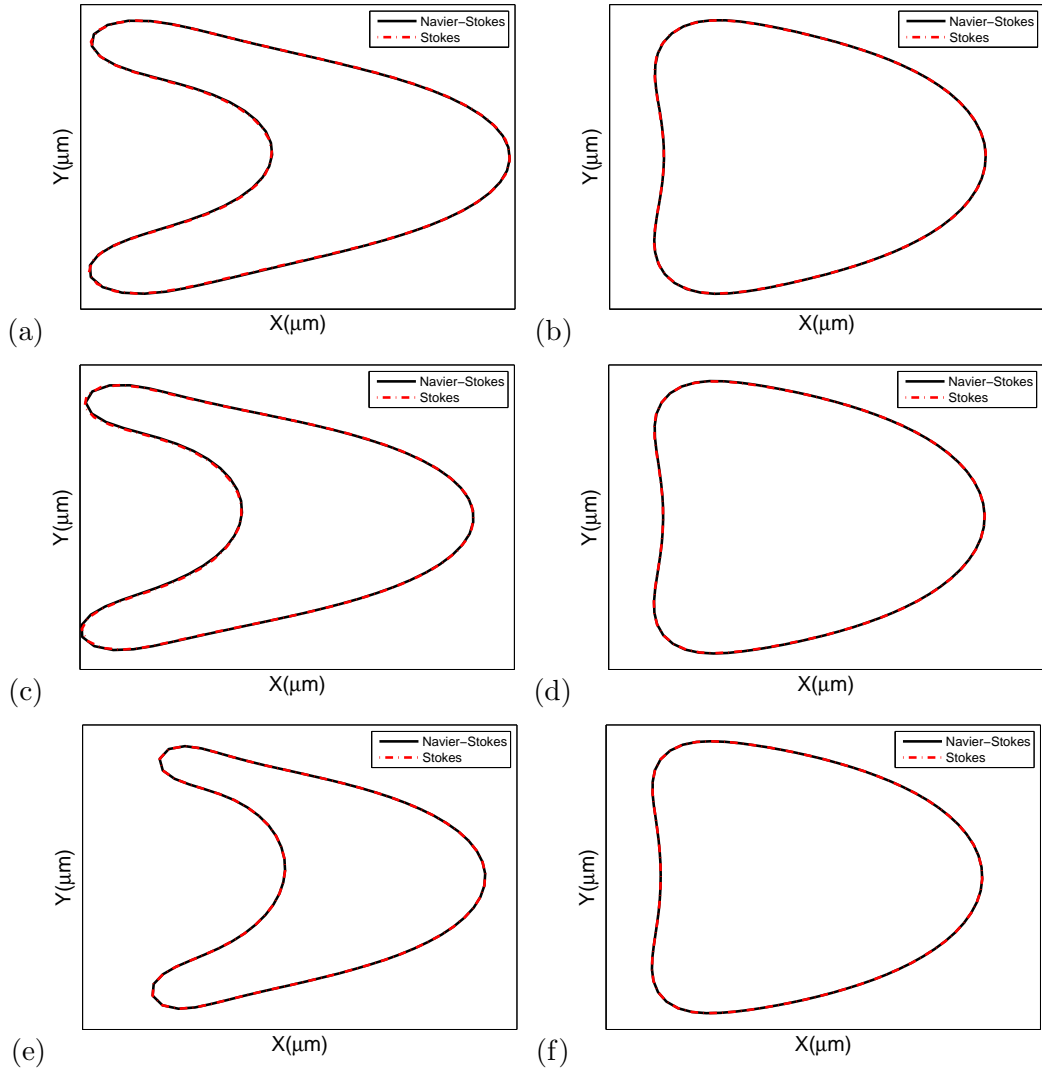
Figure 3.14: Final shapes of RBCs with cell swelling ratio $s^* = 0.481$ (a,c,e) and 0.9 (b,d,f). The maximum flow speeds are $u_{max} = 18, 36$, and 54 cm/s for the top, middle and bottom rows, respectively. Bending constant is $1k_b$.

0.22. The rest of the parameters are the same as in section 3.2.

Under both the NS and the Stokes flow model, the biconcave cell shows a similar
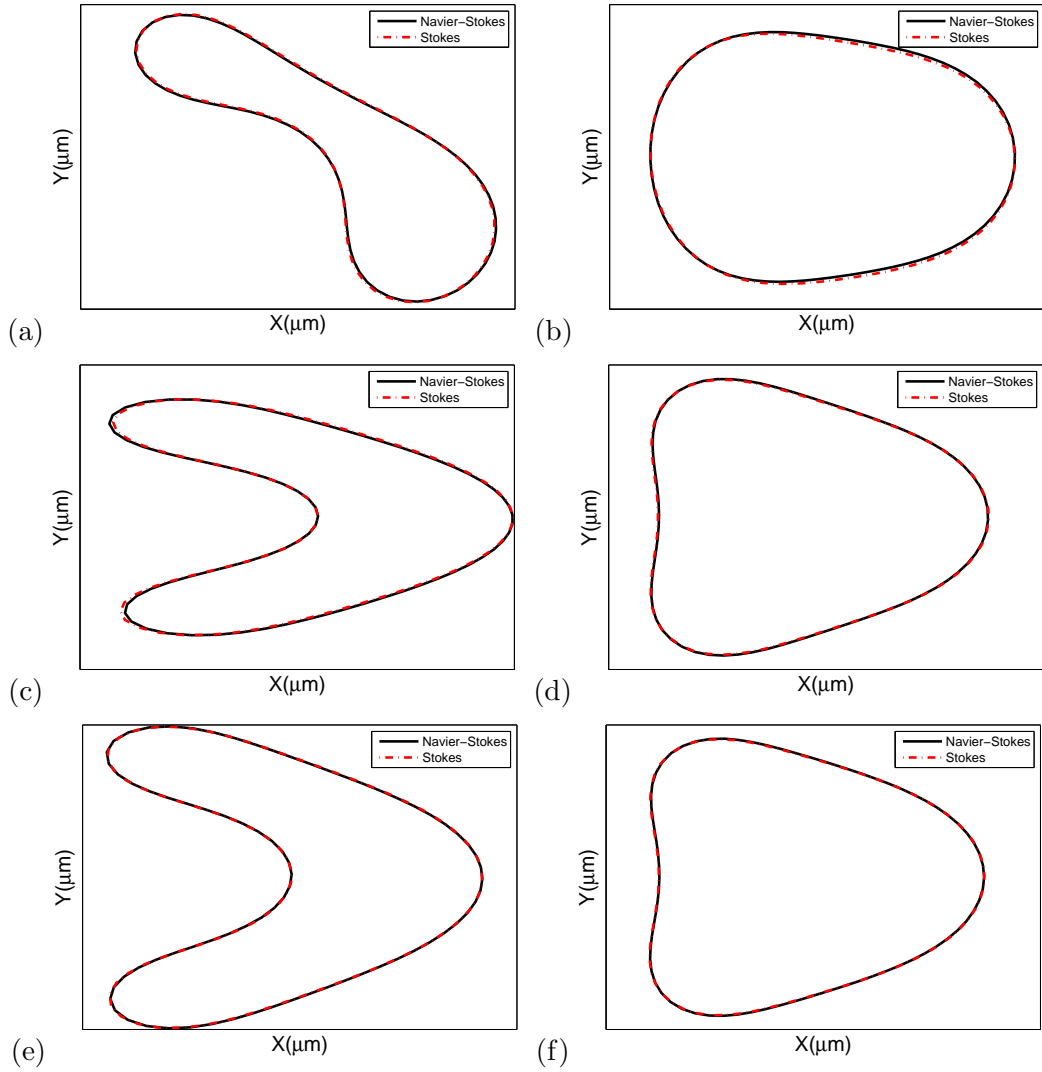
Figure 3.15: Final shapes of RBCs with cell swelling ratio $s^* = 0.481$ (a,c,e) and 0.9 (b,d,f). The maximum flow speeds are $u_{max} = 18, 36$, and 54 cm/s for the top, middle and bottom rows, respectively. Bending constant is $10k_b$.

damped oscillation motion. In the first few oscillations, as the mass center performs an up and down motion about the channel center line, the long axis of the cell shows a rigid body motion (when cell is close to the wall, it uses the tip that is closer to the wall as axis and
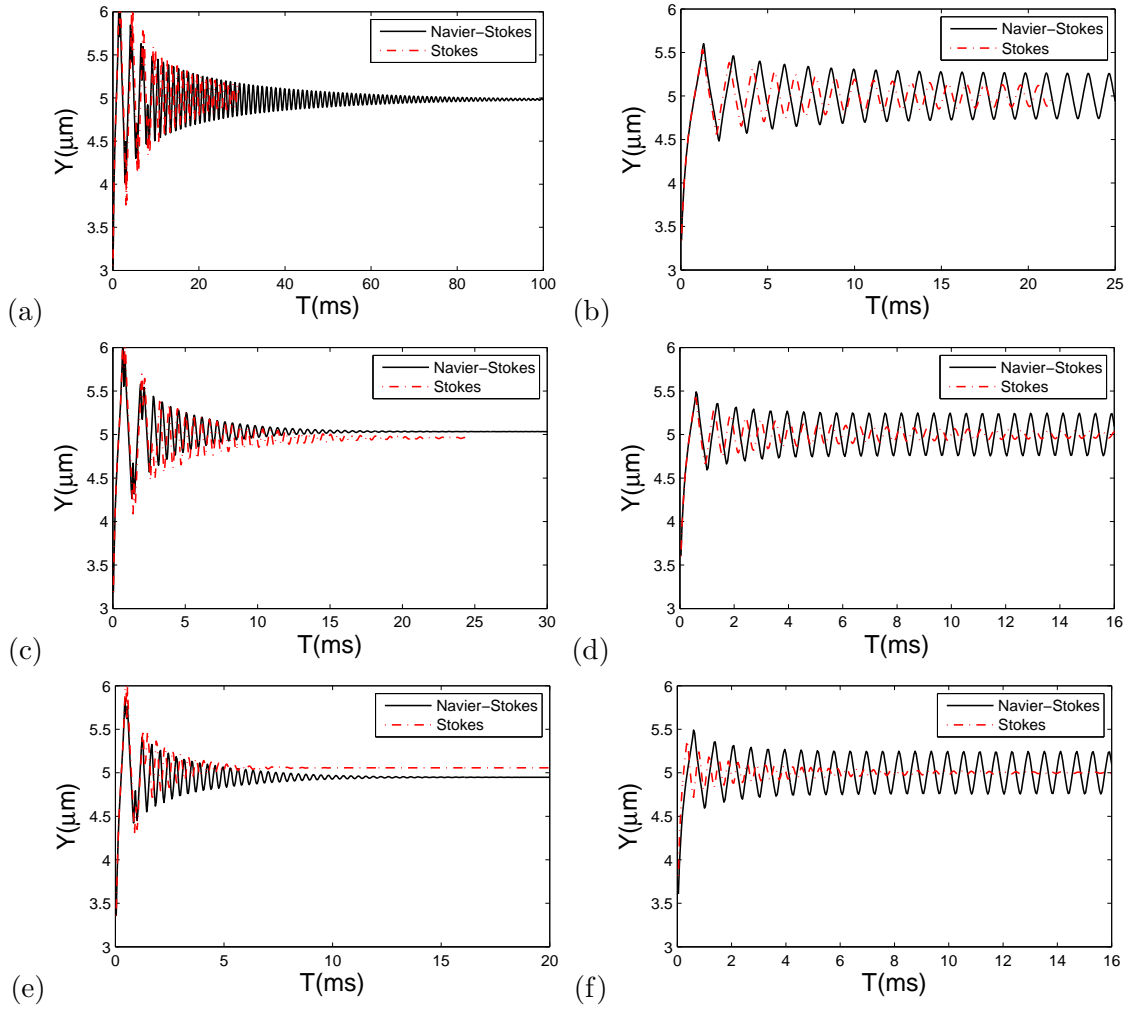
Figure 3.16: Trajectory of cell mass center with cell swelling ratio $s^* = 0.481$ (a,c,e) and 0.9 (b,d,f). The maximum flow speed is $u_{max} = 18, 36$, and 54 cm/s for three rows, respectively. Bending constant is $100k_b$.

turns). And as the oscillation in mass center becomes weaker, the cell shows a breathing motion and eventually reaches at a steady inclination angle. Snapshots of the motion of a stiff biconcave cell in Poiseuille flow is presented in Figure 3.18. Figure 3.18a explains the rigid body motion and Figure 3.18b shows the swing motion and final equilibrium state.
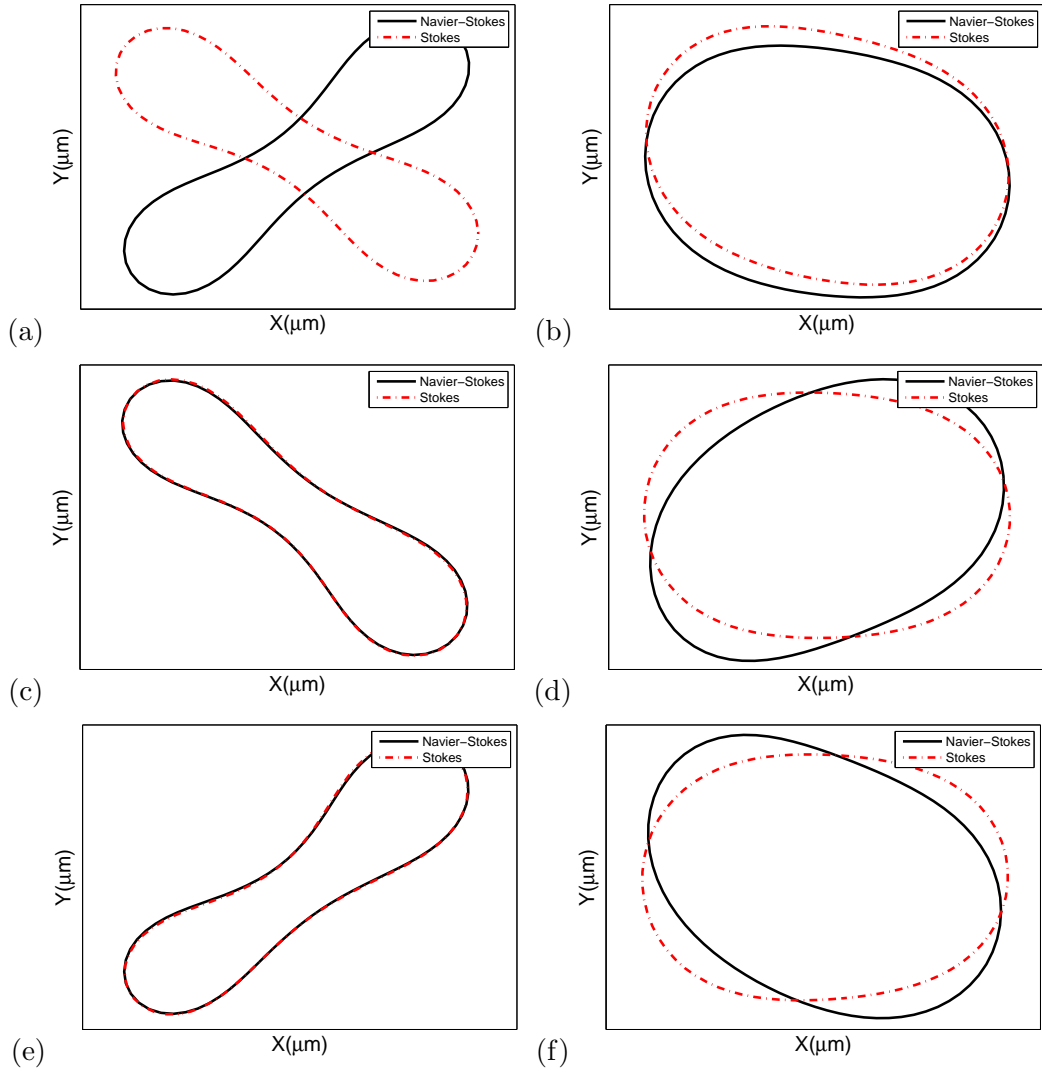
Figure 3.17: Final shapes of RBCs with cell swelling ratio $s^* = 0.481$ (a,c,e) and 0.9 (b,d,f). The maximum flow speed is $u_{max} = 18, 36$, and 54 cm/s for three rows, respectively. Bending constant is $100k_b$.

The elliptical cell shows different motions under NS flow model and Stokes flow model. In the NS flow, the cell shows a snaking motion. The cell swims up and down crossing the channel center line. No damping of the magnitude of oscillation of mass center is observed.

53
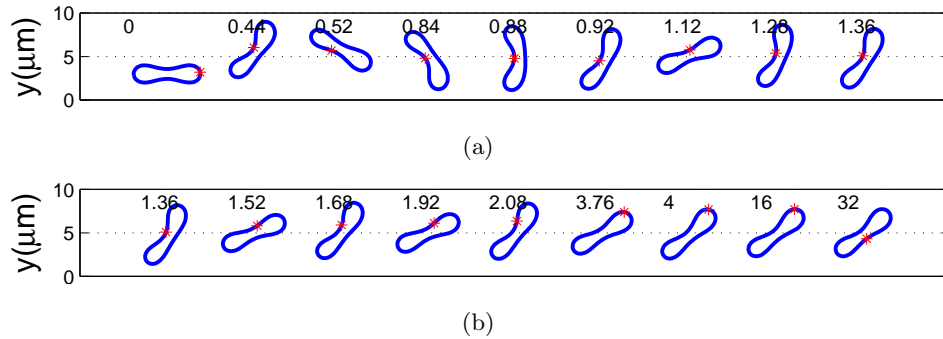
Figure 3.18: The snapshots of motions of a stiff biconcave RBC in Poiseuille flow. The number above each snapshot marks the time in millisecond (ms).

On the other hand, the elliptical cell under Stokes flow shows a damped oscillation and the cell eventually stays at the flow center line with a bullet-like equilibrium shape. The snaking motion in NS flow and the damped oscillation motion in Stokes flow is plotted in Figure 3.19.

3.4   Conclusion

The comparison of the motions of a single RBC under two flow models, namely the Navier-Stokes and the stationary Stokes, is presented in this chapter. In shear flow, the steady inclination angles are matched for cells with different swelling ratio. In Poiseuille flow, by comparing the history of cell mass center, snapshots of positions and shapes of the cells, and trajectory of marked points on the membranes, motions of cells under the two flow models agree with each other very well when the cell is soft. The motions start to show difference when the cell becomes stiffer. The cell with biconcave shape is easier to bend along its long axis because it has plenty of excessive membrane length to be deformed

54
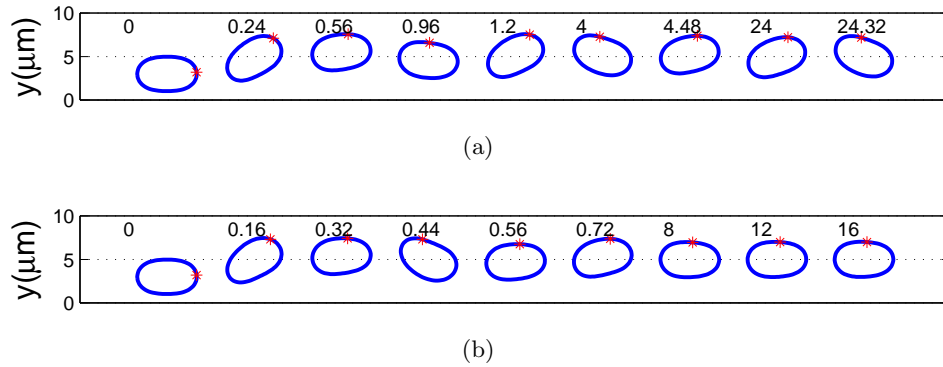
Figure 3.19: The snaking motion in NS flow and the damped oscillation motion in Stokes flow of an elliptical cell. The bending is $100k_b$, the speed at the center line of the flow is $54cm/s$. The number above each snapshot marks the time in millisecond (ms).

while maintaining the cell area. The oscillation eventually damps out and the cell stays at the center region of the flow with a steady inclination angle. The elliptical shaped cell shows different motions under two flow models. In NS flow, a snaking motion is observed but a damped oscillation motion is observed in Stokes flow. This difference is caused by the inertial effect as the elliptical cell is less deformable due to the lack of excessive length and behaves closer to a rigid particle. The lifting inertial effect caused by the angular motion of the long axis of the cell gives the cell an extra push to keep the oscillation from damping out. As a conclusion, both NS model and Stokes model can be used when the motion of the cell is deformation dominated. When the cell becomes stiffer, inertial effect becomes more important and a full Navier-Stokes model is a more proper model for the fluid.

Chapter 4

Infected RBC in flows

Biological fluid mechanics often requires one to study the dynamics of a lipid membrane encapsulating some cellular contents. For instance, a compound membrane usually consists of a lipid bilayer membrane enclosing a fluid with a suspended particle in it. Since the bilayer membrane resists area dilation and is on the order of a nanometer in membrane thickness, one can neglect the thickness while modeling the compound cell. In this chapter, the motions of a single malaria-infected RBC in flows are investigated by numerical simulation. The infected RBC (iRBC) is modeled as a membrane enclosing a rigid particle. The cell model and numerical scheme is validated by comparing the steady inclination angles of the tank-treading motions in shear flow with results by Lai [34]. The motions of a single iRBC in Poiseuille flow is then investigated. In the last section we look into interactions between iRBC and healthy RBCs in bounded Poiseuille flow.

4.1 Validation of iRBC model

In this section, we perform a series of numerical tests to simulate the motions of a compounded iRBC in shear flow. The computational domain through out this section is 20×20 µm ^{2} as in [34]. The shear rate of the flow is set as $50 \ s^{-1}$, Two different swelling ratios ($A = 0.84$ and $A = 0.95$) of cells is used. The filling fraction $\Phi = a^2\pi/A$ of the particle varies from 0 to 0.2. The compounded iRBC is initially placed at center of the domain $(10, 10)$. With the filling fraction increases, the angle between the cell long axis and the horizongtal line decreases as shown in Figure 4.1 and Figure 4.2. This can be explained as follows: by including a solid particle, the energy dissipation enhances, so the compound interface behaves like an inclusion-free interface that encapsulates a more viscous fluid. The larger the inclusion is, the higher the effective viscosity will be. And as shown in Figure 4.2, the results agree with those in [34] well. the steady inclination angle is close with the results in [34]. The slope in [34] is steeper than our results. This is because in [34], a force free condition is forced on the particle so the particle is forced to stay still. In our model, free motion is allowed on the particle. So the particle shows less resist to flow as in [34].

4.2 Motions of iRBC in bounded Poiseuille flow

A malaria-infected RBC (iRBC) undergoes a series of changes at different stages. The parasite forms a round ring shape in the early stage and keeps growing in size. At late stages the parasite forms a 'core' inside the cell, causing the cell to lose its biconcave formation and turn into a elliptical shape. In addition to the size change, the parasite also releases a protein causing the membrane to become stiffer. Understanding the motions of
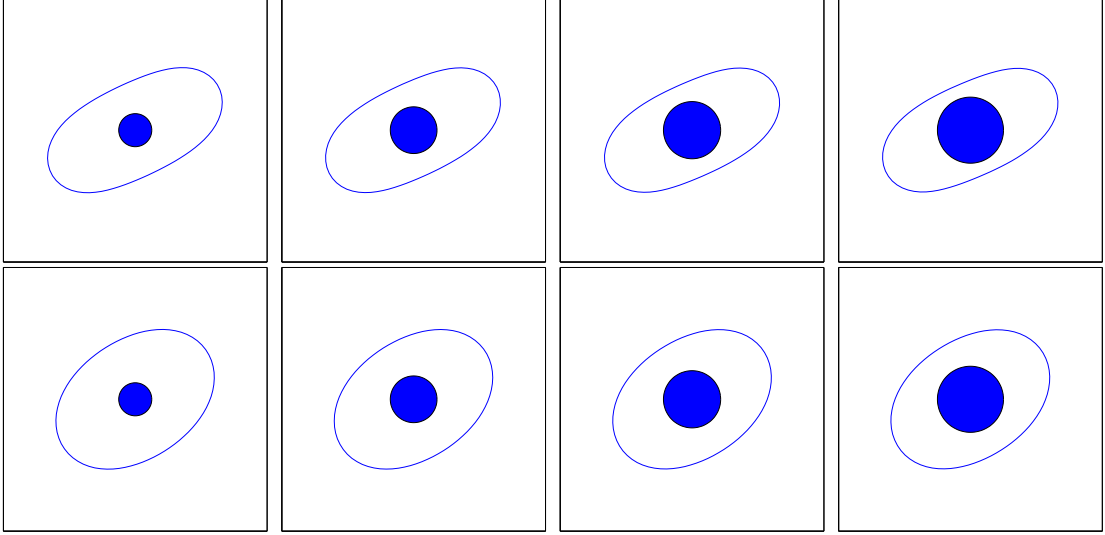
Figure 4.1: Final steady tank treading state of a compound iRBC in shear flow. The filling fraction is $\Phi = 0.05, 0.10, 0.15, 0.20$ from left to right for each row. The cell swelling ratio is 0.84 for the upper row and 0.95 for the lower row.

iRBCs in flows can help design cell separation tools in malaria treatment.

In this section, a single iRBC is put into bounded Poiseuille flow. The values of parameters for modeling cells are as follows: The bending constant is $k_b = 5 \times 10^{-10} \text{N} \cdot \text{m}$, the spring constant is $k_l = 5 \times 10^{-8} \text{N} \cdot \text{m}$ and the penalty coefficient is $k_s = 10^{-5} \text{N} \cdot \text{m}$. The cells are suspended in blood plasma which has a density $\rho = 1.00 \text{g/cm}^3$ and a dynamical viscosity $\mu = 0.012 \text{g/(cm} \cdot \text{s)}$. The viscosity ratio which describes the viscosity contrast of the inner and outer fluid of the RBC membrane is fixed at $\lambda = 1.0$. The Reynolds number is defined by $Re = \rho U H / \mu$, where $U = u_{max}$ is maximum velocity at the channel center without cell. The capillary number is defined by $Ca = \mu G_r R_0^3 / B$, where G_r, R_0, and B represent the shear rate of fluid flow, the effective radius of the cell, and the bending coefficient, respectively. The computational domains are $100 \times 10 \ \mu\text{m}^{\ 2}$ for the narrower
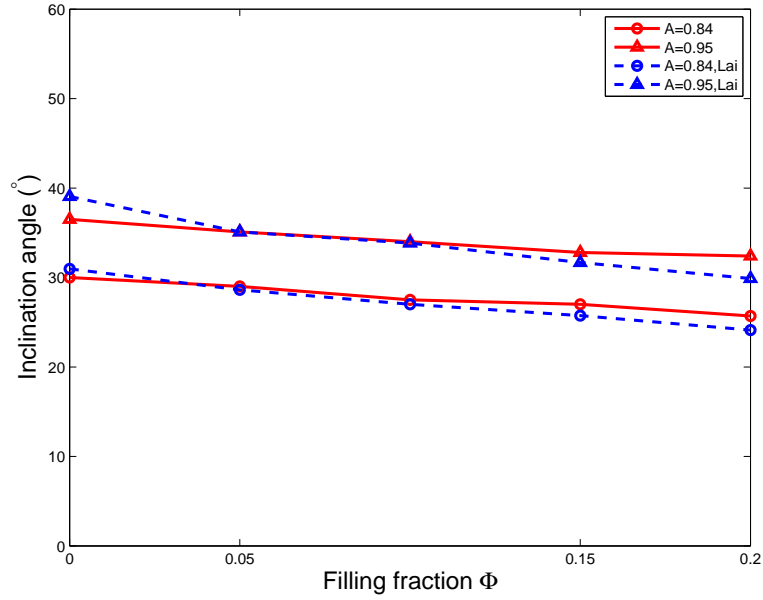
Figure 4.2: Plot of steady inclination angle as a function of filling fraction.

channel and 100×20 µm^2 for the wider channel. The grid resolution for the computational domain is 64 grid points per 10 μm. The time step $\triangle t$ is 10^{-5} ms. The initial velocity of the fluid flow is zero everywhere and the initial positions of the mass center of the cell are either at middle of the channel with $\phi_0 = 45°$ or at 30% of the channel width with $\phi_0 = 0°$. The swelling ratio of the RBC is $s^* = 0.9$. A neutrally buoyant rigid particle is put inside the cell with filling fraction ratio $\Phi = 0.2$ to 0.4. In the following subsections we will look into effects of the maximum velocity of the flow, effects of the filling fraction, effects of the membrane stiffness, and the effects of channel width on the motions of the iRBC.

4.2.1   General description of iRBC motion

It is well known that in Poiseuille flow, a healthy RBC tends to move towards the center region of the flow where the flow is faster. This is due to the deformability of the
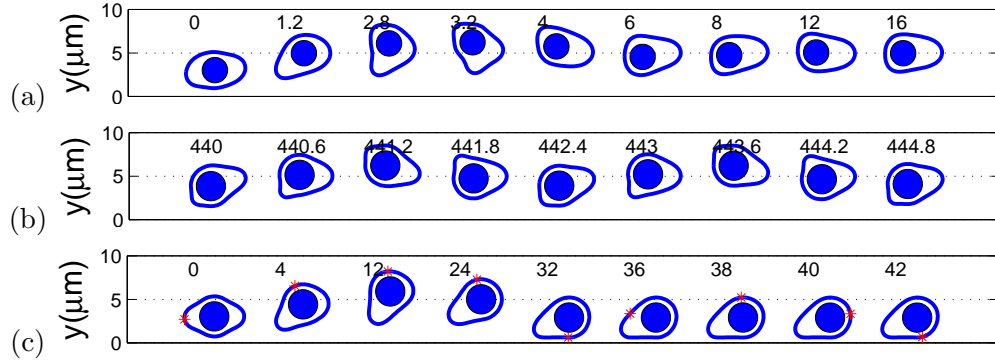
Figure 4.3: Snapshots of motions of iRBC in channel flow. The snapshot (a) is of iRBC with $\Phi = 0.3$, $y_0 = 5\mu$m and $u_{max} = 5cm/s$, the cell stays at the center of the flow. The snapshot (b) is of iRBC with $\Phi = 0.4$, $y_0 = 5\mu$m and $u_{max} = 15cm/s$, the cell keeps oscillating up and down. The snapshot (c) is of iRBC with $\Phi = 0.4$, $y_0 = 3\mu$m and $u_{max} = 1cm/s$, the cell is pushed to the side of the channel and undergoes a tank-treading motion. The red asterisk marks the trajectory of the same point on the mambrane of an iRBC. The number above each snapshot marks the time in millisecond (ms).

cell membrane. There is no deformability for the rigid particle. The flow shear gradient causes the particle to migrate away from the channel center and the inertial wall lifting effect tends to push the particle toward the channel center. The motion of a particle in Poiseuille flow is determined by the competition between the pushing force from the flow shear gradient and the lifting wall effect. The compounded iRBC's motion has features from both motions. The soft membrane deforms easily and tend to migrate toward the center region of the flow. But due to the existence of the rigid inclusion, deformability of the rear part of membrane near the inclusion is greatly hindered and its behavior is more like a particle as it tends to migrate away from the channel center. The competition between these two effects determines the motion of iRBC in Poiseuille flow.

60

As shown in Figure 4.3, three motions of iRBC in Poiseuille flow are observed: a steady pulling motion, an oscillation motion, and a stick to the wall tank-treading motion. In the steady pulling motion and the oscillation motion, the motions of the iRBC can be described as an inclusion free end leading the motion while the rear inclusion adjacent region lags behind. In the stick to the wall tank-treading motion, the cell sticks on the wall and the membrane undergoes a tank treading motion around the particle and moves forward. In the steady pulling motion, the inclusion size is small so it affects a smaller part of the membrane leading to a smaller pushing force. The pushing force is balanced by the pulling force from the tip of the iRBC so the cell can stay steady. The oscillating motion appears when we increases the inclusion size. In this case the rear pushing force becomes stronger so the cell starts to oscillate. The stick to the wall motion appears when the inclusion free end of the cell fail to lead the motion. Then the motion is more determined by the rear end and is pushed away to the side of the channel.

4.2.2   Effects of the maximum velocity

The speed of the flow has direct connection with the force exerted on the cell membrane. To the inclusion-free end of the cell, the force is pulling as it pulls the cell to migrate toward the region where the flow is faster. To the inclusion adjacent end of the cell, the force is more like a push causing the rear end of the cell to move away from the center region of the flow. When the flow is slow, the pulling force is weak so the cell with 40% filling fails to stay at the channel center and is pushed to the side of the channel as shown in Figure 4.3(c). The history of the cell mass center for different filling fraction and different flow velocity is plotted in Figure 4.4. When the flow is slow, the iRBC with $\Phi = 0.2$ and $\Phi = 0.3$ shows an oscillation motion. When the flow becomes faster, a steady pulling motion is observed.
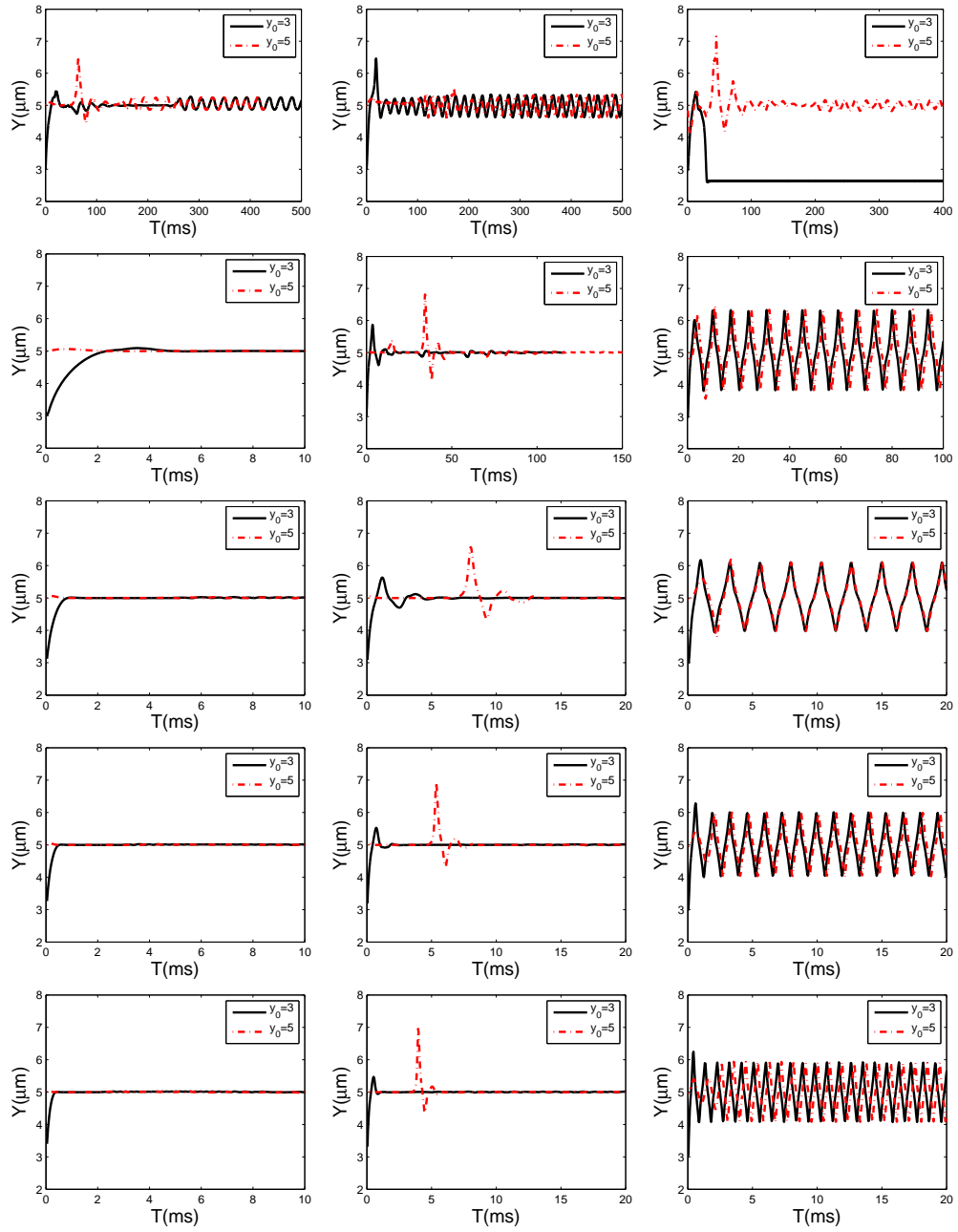
Figure 4.4: History of trajectory of cell mass center. The filling fraction is $\Phi = 0.2, 0.3, 0.4$ from left to right for each row. The velocity at centerline is $u_{max} = 1, 5, 15, 25, 35$ cm/s from up to low.

This is because the faster flow helps the cell to maintain a steady shape as it provides larger force to restrict the deformation of the membrane. In the oscillating motion, faster flow provides stronger pulling force to resist the rear end motion. So the magnitude of oscillation decreases as the flow speed increases.

4.2.3   Effects of the filling fraction

In this subsection, we look into the effects of filling fraction on the motions of the iRBC in a narrow channel. The channel width is 10μm, the cell membrane has bending constant of $1k_b$ and the filling fraction increases from $\Phi = 0.2$ to $\Phi = 0.4$ of the cell volume. The existence of a rigid inclusion will hinder the deformability of the membrane near it. The larger the inclusion, the greater part of membrane it affects. As shown in Figure 4.4: with filling fraction 0.2, there is enough excessive membrane to deform so the cell quickly reaches the equilibrium state; the iRBC undergos a few oscillations before it can reach the equilibrium state as the filling fraction increases to 0.3 because it has less excessive membrane; with a large inclusion volume of 0.4, there isn't enough excessive membrane to deform for the iRBC to reach an equilibrium state, instead the cell shows an oscillating motion. The magnitude of the oscillation is the same regardless of whether it is initially put in center of the channel or on side of the channel as shown in Figure 4.4. The magnitude is determined by the volume of the rigid inclusion and the flow speed.

4.2.4   Effects of membrane stiffness

It has been reported that at late stage of malaria, the cell membrane can be 10 times stiffer than that of a healthy one [37, 60]. In this subsection, the membrane bending constant is set as $10k_b$ while keeping all the parameters same as the previous subsection.
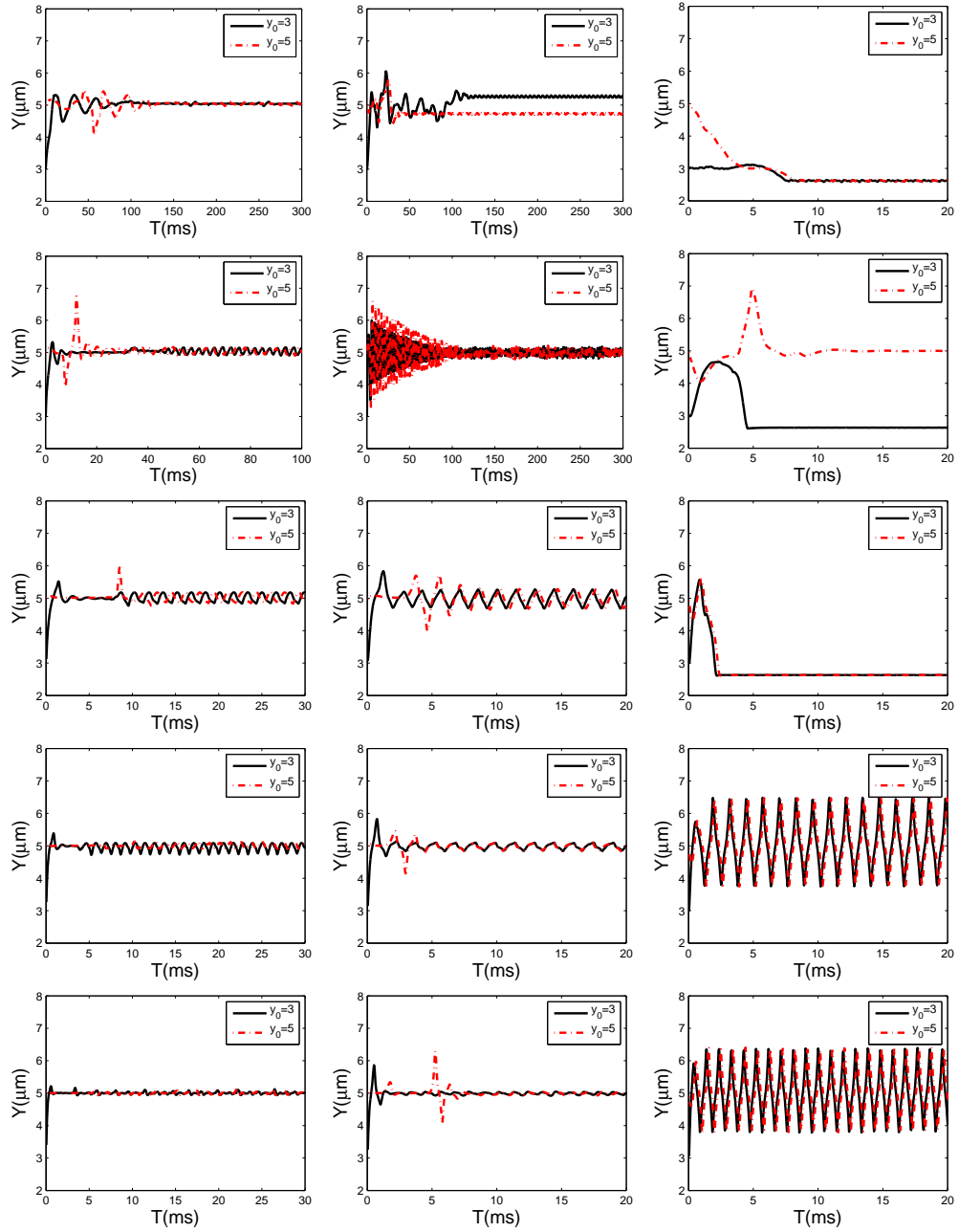
Figure 4.5: History of trajectory of cell mass center. The filling fraction is $\Phi = 0.2, 0.3, 0.4$ from left to right for each row. The velocity at centerline is $u_{max} = 1, 5, 15, 25, 35 cm/s$ from up to low.

The history of iRBC mass center is plotted in Figure 4.5. In the cases with filling fraction of 0.2 and 0.3, the cell fail to stay steady at the channel center and an oscillation motion is observed. For filling fraction of 0.4, the iRBC goes to the side when u_{max} is from 1 to $15cm/s$. The oscillation motion is observed for u_{max} euqauls to 25 and $35cm/s$. The reason for such motions is that the stiffened membrane show greater resist to external force thus the pulling force from the inclusion-free part of the cell becomes weaker, making it hard for the cell to stay at the channel center. This partially explains the fact that at late stage of malaria infection, the sick cell moves to the side of the flow sticking to the wall.

4.2.5   Effects of the channel width

In this subsection, the channel width is set as 20μm. The filling fraction is 0.4. Because the channel width is doubled, to have the same Reynolds number as in the narrow channel case, u_{max} is reduced to half. The behaviors of the iRBCs in a wider channel with same Reynolds number are investigated. The motions of iRBC is plotted in Figure 4.6. Since the u_{max} in the channel center is cut to half, so is the shear gradient. A reduced shear gradient weakens the pulling force from the fluid to the cell membrane. As shown in the Figure 4.6, for the iRBCs with bending rigidity $1k_b$, all cases with initial cell position on side of the channel eventually sticks to the wall; and for the stiffer iRBC, except $u_{max} = 0.5cm/s$, the iRBC goes to the side. The iRBC in the very slow case doesn't go to side is because the flow being too slow, neither the pulling nor the pushing force is strong enough to show dominating effect. So the motions of the iRBC in a very slow flow is zigzagging. Comparing the results in Figure 4.6 and the results in Figure 4.4 and Figure 4.5, we can conclude that in cell separation design, while the flux ($u_{max} * L$ where L is the channel width) is constant, a wider channel can have better results in separating the sick cells.
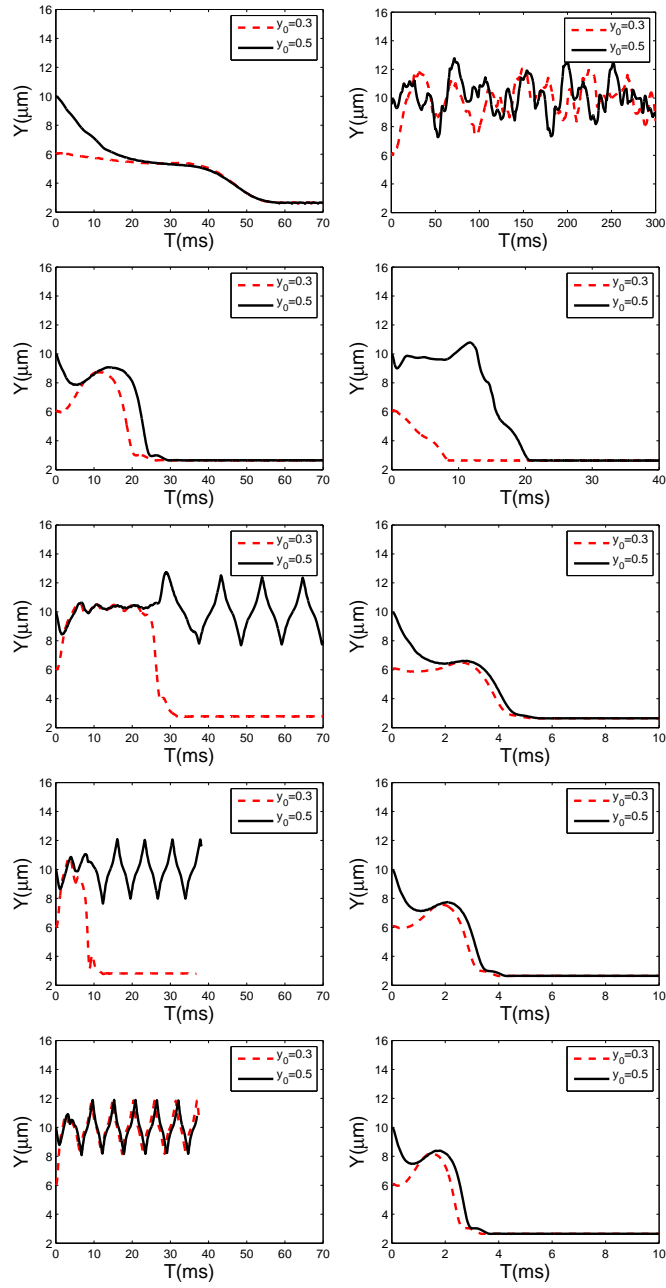
Figure 4.6: History of trajectory of cell mass center in a wide channel with same Reynolds number as in the narrow channel. The left column is iRBC with $1k_B$ and $10k_b$ on the right.

66

4.3   Interaction between healthy RBC and iRBC

The interaction between healthy RBCs and iRBC is investigated. The computational domain is set as 80×10 µm ^{2}. The parameters for the RBC and fluid properties are the same as the previous section. For the iRBC, the swelling ratio of cell is $s^* = 0.9$, the filling fraction is $\Phi = 0.4$, and the membrane stiffness is $1k_b$. The maximum velocity at channel center without cells is $2cm/s$, which corresponds to a Reynolds number of $Re = 0.11$.

We first look into the case with 8 healthy RBCs in the channel flow distributed with even space in the domain. As shown in the snapshots in Figure 4.7(a)-(g), the cells are initially distributed in the domain evenly spaced. In the beginning the cells lines up like a chain at the channel center (Figure 4.7(b)), but this state is unsteady and eventually breaks as in Figure 4.7(c). The snapshots in Figure 4.7(d)-(g) shows the motions of cells in the channel. Even sometimes some cells can be pushed close to the channel walls as in Figure 4.7(e), they tend to stay at the channel center where flow is faster and leaving a cell-free layer close to the upper and lower boundaries. In Figure 4.8, the trajectory of the cell mass centers are plotted. From the figure we can see a clear cell-free layer in the adjacent area of the channel walls.

Then the interaction between 7 healthy RBCs and a sick iRBC is then investigated. The 8 cells are distributed in the domain with even spacing and initial inclination angles of 90°. The healthy cell has a biconcave shape with swelling gratio of 0.481 and the sick cell has a swelling ratio of 0.9. The inclusion size $\Phi = 0.4$. Once the cells start to move, the RBCs catches up with the iRBC because it has more excessive membrane length allowing it migrate to the faster flow region easily. For the same reason, after the RBCs get closer to the iRBC, they tend to pass by the iRBC through the space between the iRBC and the
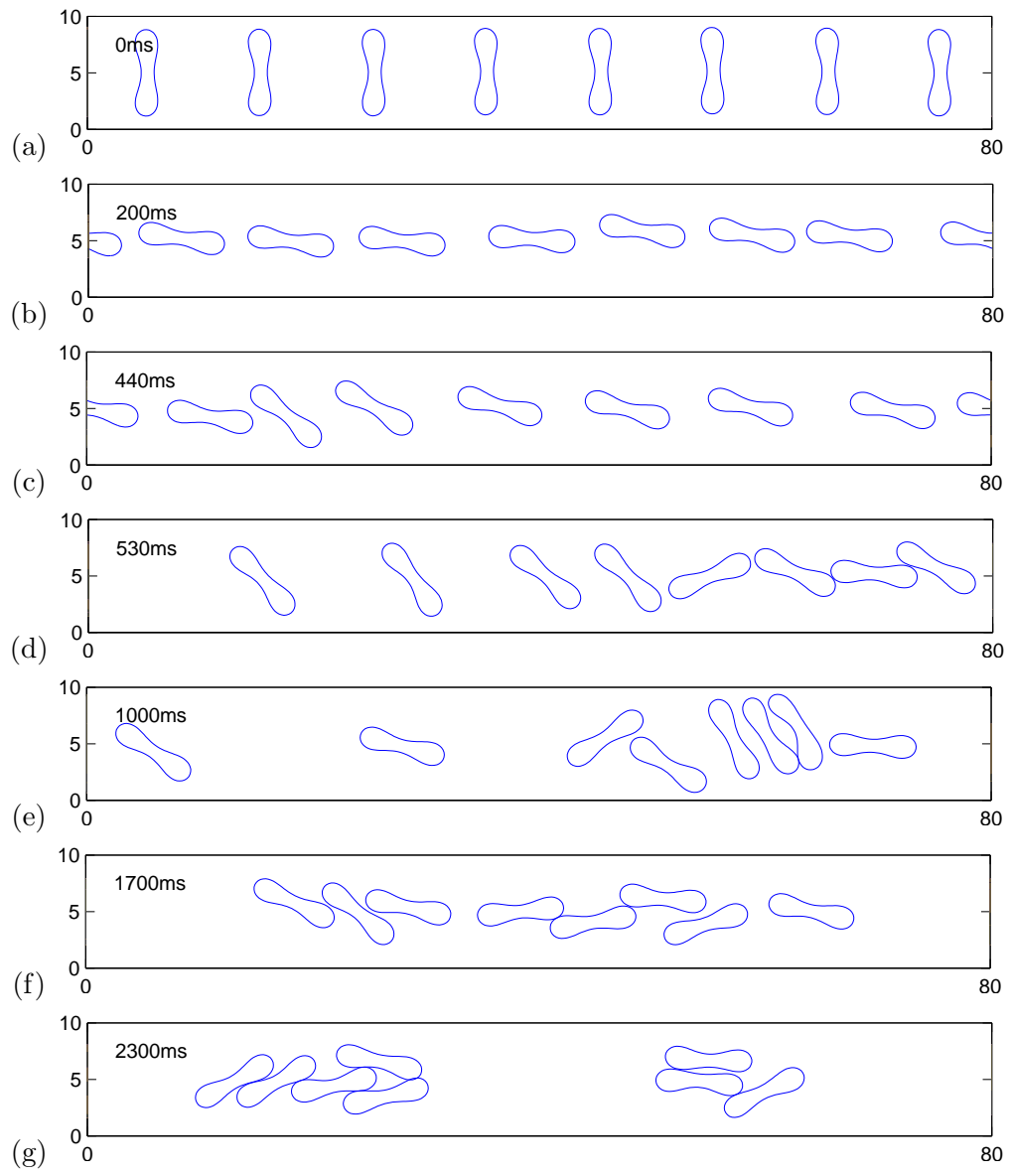
Figure 4.7: Snapshots of 8 healthy RBC in channel flow.
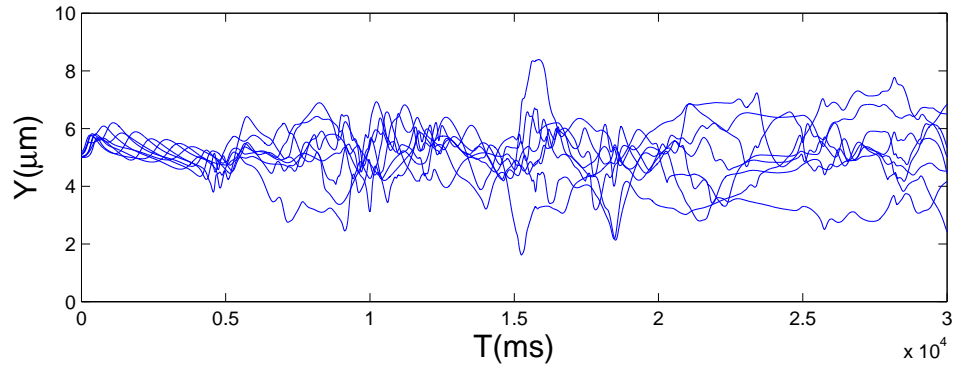
Figure 4.8: Trajectory of the cell mass centers in channel flow.

channel wall. This motion pushes the iRBC to the side of the channel. An illustration of the procedure of a RBC bypassing an iRBC is shown in Figure 4.9, It takes time for a RBC to bypass an iRBC and in the mean while more RBCs catches up with them and causes a stack up of cells behind the infected cell as shown in Figure 4.10(a)-(c). Then the stacked RBCs compete to squeeze through the pack and eventually detaches from the iRBC and continue in the flow. During the procedure of RBCs bypassing the iRBC, the iRBC keeps being pushed to the side of the channel (Figure 4.10(d)-(j)). In Figure 4.11, the trajectory of cell mass center is plotted. The red solid line represents the trajectory of iRBC while the blue dotted lines represent the RBCs. The fact that the red line is above the blue lines means that the iRBC is pushed toward the upper channel wall by the healthy RBCs. Because the cells are stacked up, keeping in mind that the inclusion in the iRBC has a radius of about $1.7\mu m$ and it is pushed against the wall most of the time, there is almost no cell free layer in this situation.
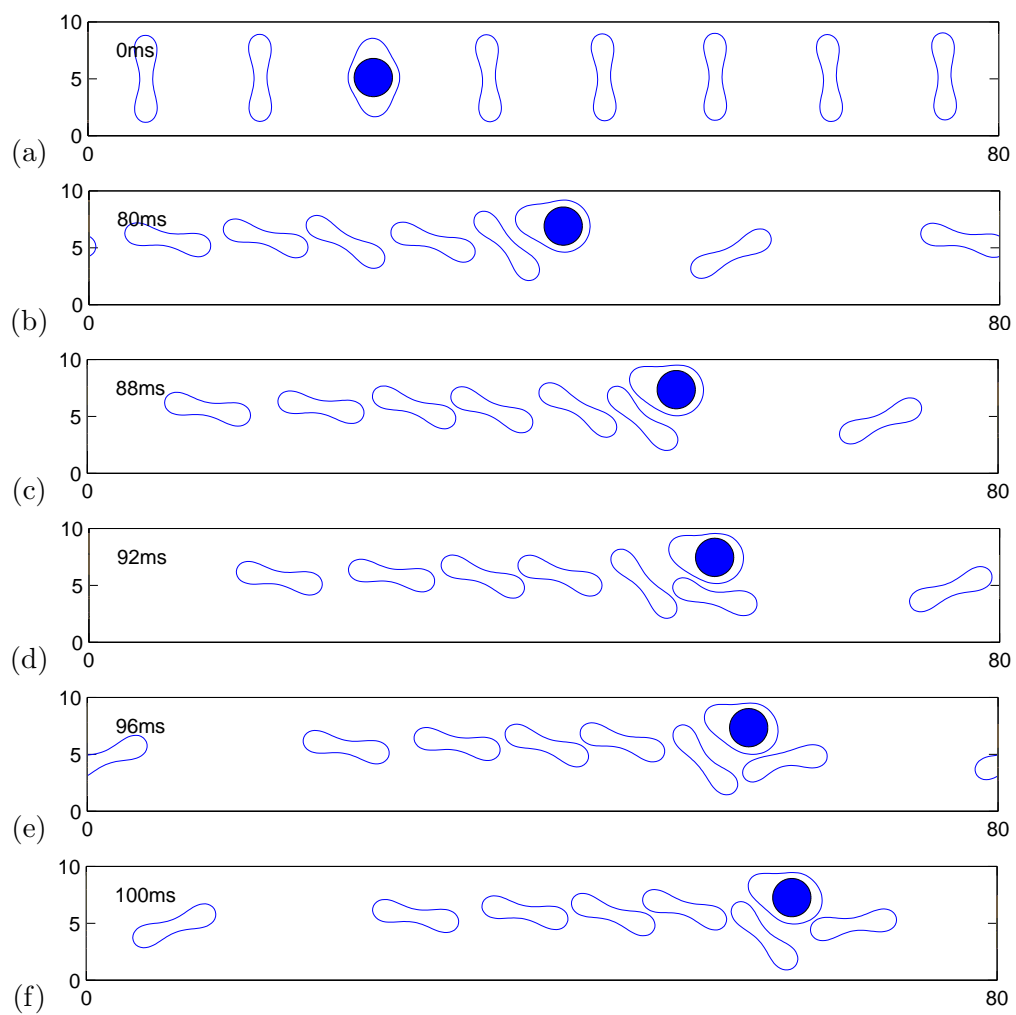
Figure 4.9: Snapshots of interaction between 7 healthy RBCs and a sick iRBC.
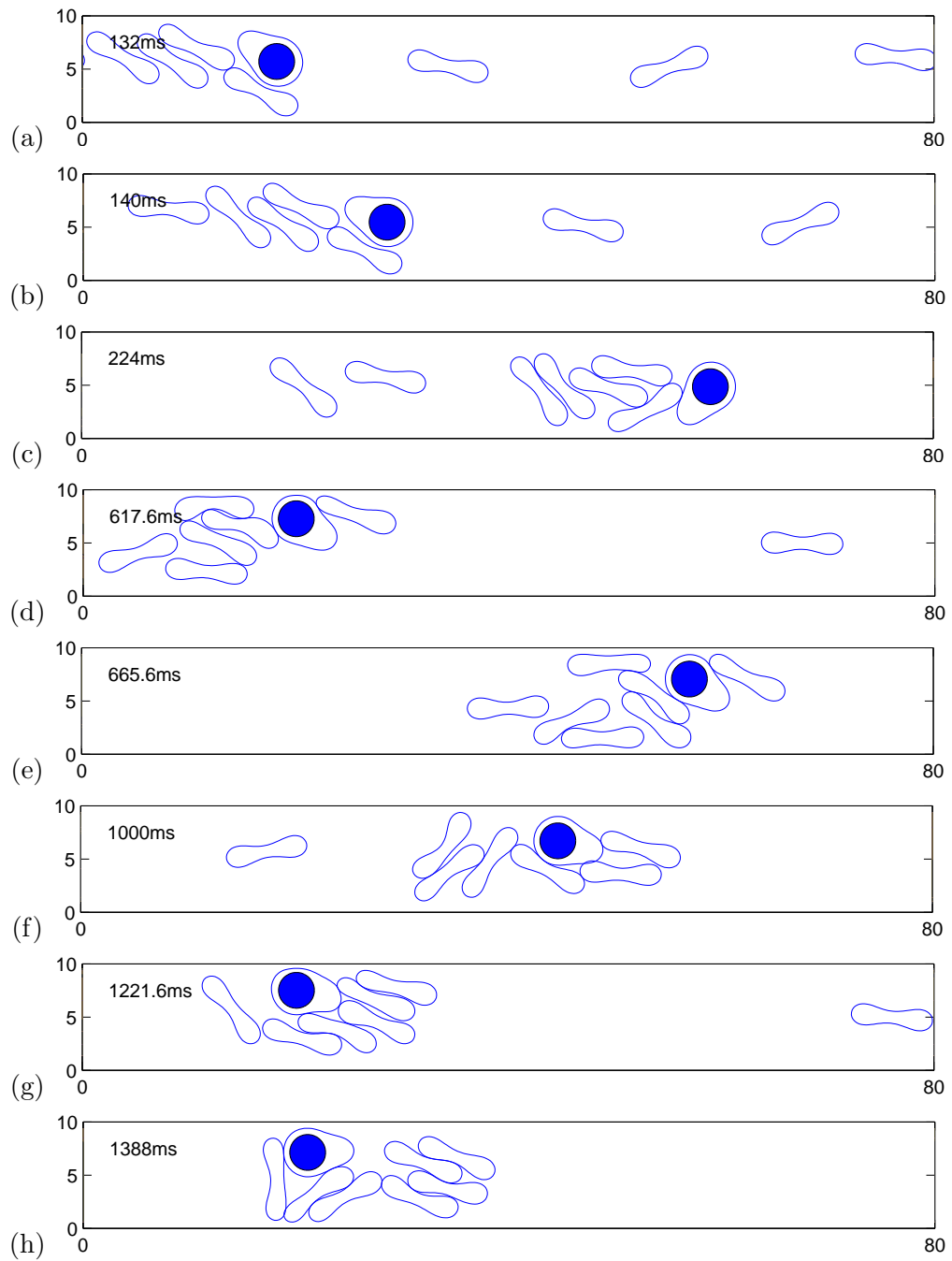
Figure 4.10: More snapshots of interaction between 7 healthy RBCs and a sick iRBC.
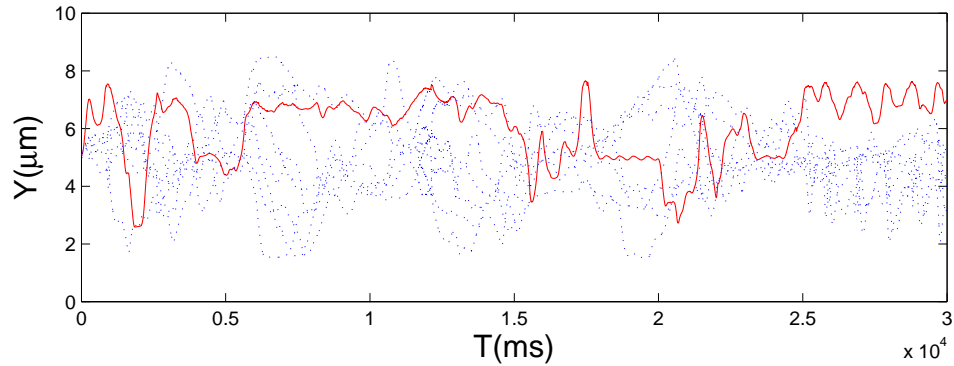
Figure 4.11: Trajectory of the cell mass centers in channel flow.

4.4 Conclusion and future work

In this chapter, the motions of malaria-infected RBC in blood flow is investigated by numerical simulation of a compound cell enclosing a rigid particle. Medical experiments show at late stage, the infected cell tend to migrate toward the vessel walls. Through numerical simulation we find this phenomenon can be explained as combination of two facts: 1) with a parasite inside the deformability of the RBC is hindered, making the cell hard to stay at the channel center; and 2) It is easier for the healthy RBC to move toward the region where flow is faster because it has more excessive membrane and has less resist to deformation. While healthy RBC bypasses the iRBC, it pushes the iRBC toward the channel wall.

As for future work, it is reported that malaria can cause blockage of micro-vessels. This phenomenon is not seen here. Also the interactions between multiple iRBCs and RBCs in a wide channel is an interesting topic because this can help design cell separation tools.

Chapter 5

A new scheme for handling a fluid flow with non-constant viscosity

In this chapter, a new scheme discussed in subsection 2.7.2 to handle the non-constant fluid viscosity of inside and outside the RBC membrane has been applied to analyze the motion of a RBC with higher inner fluid viscosity. As a validation, the numerical results for the steady inclination angles of the tank treading motion are compared with the simulation results by Kim *et al.* [33] and theoretical results by Keller *et al.* [32]. The cell swelling ratio (s^*) varies from 0.481 to 0.9 and the viscosity ratio of the interior and exterior fluid $(\lambda = \dfrac{\mu_{in}}{\mu_{out}})$ varies from 1 to 5. When $\lambda = 1$, the viscosity of the fluid is constant throughout the domain. The values of parameters for modeling cells are as follows: the bending constant is $k_b = 5 \times 10^{-10} \text{N} \cdot \text{m}$, the spring constant is $k_l = 5 \times 10^{-8} \text{N} \cdot \text{m}$ and the penalty coefficient is $k_s = 10^{-5} \text{N} \cdot \text{m}$. The cells are suspended in blood plasma which has a density $\rho = 1.00 \text{ g/cm}^3$ and a dynamical viscosity $\mu = 0.012 \text{ g/(cm} \cdot \text{s)}$. The computational domain is $30 \times 50 \ \mu m^2$, the cell is put at center of the domain $(15, 25)$. The grid resolution

for the computational domain is 64 grid points per 10 μm. The initial velocity of the fluid flow is zero everywhere.

5.1 Validation of models
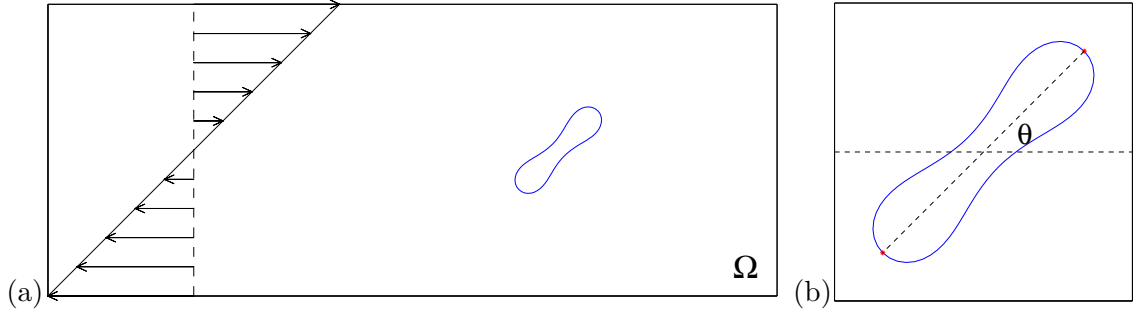
Figure 5.1: An schematic diagram of a single red blood cell in shear flow with the computational domain Ω, the inclination angle θ is defined as the angle between the cell long axis and the horizontal line.

Over the past decades, the dependence of the inclination angle θ on the swelling ratio s^* and the viscosity ratio of λ has been studied by many researchers. For the ellipsoidal shape particle (i.e. the membrane deformation is not considered), Keller *et al..* [32] has given an evolutional equation for the inclination angle θ as shown in Figure 5.1(b):

$$\frac{d\theta}{dt} = A + B\cos(2\theta) \tag{5.1}$$

where A and B are functions of the viscosity ratio λ and the shear rate $\dot{\gamma}$, and the shape of the ellipsoid (see [32] for more information about A and B). There are two motions determined by the Equation (5.1) namely, (1) the tank-treading motion if $A/B < 1$, where the fixed inclination angle θ can be calculated by

$$\theta = \frac{\arccos(-A/B)}{2} \tag{5.2}$$

74

(2) the tumbling motion if $A/B > 1$, where the general solution of the equation (5.1) can be expressed as

$$\theta(t) = \arctan(\frac{A + B}{\sqrt{A^2 - B^2}} \tan(\sqrt{A^2 - B^2}(t - t_0))). \tag{5.3}$$

Due to the non-constant viscosity, we have used the SOR method to solve the related diffusion equation in the operator splitting scheme (short for SOR scheme). By re-arranging the viscosity term as in equation (2.77) we can apply the fast solver FISHPAK (short for FISHPAK scheme) to solve the diffusion equation. In Figure 5.2, the final steady shapes of the tank-treading motion by both schemes are compared. The results by the FISHPAK scheme show the exact match with whose by the SOR scheme. We further validate the inclination angle with the simulation results by Kim *et al.* [33] and theoretical results by Keller *et al.* [32]. In the tank-treading regime, the inclination angle θ is a decreasing function of the viscosity ratio λ for the same swelling ratio s^* , but for the same viscosity ratio λ, the inclination angle θ increases as the swelling ratio s^* increases. The steady inclination angle θ as a function of the viscosity ratio λ for different values of the swelling ratio s^* is plotted in Figure 5.3. Our simulation results show good agreement with the numerical results reported in [33] by Kim *et al.*. The small deviation of our results from Keller *et al.* ([32]) is due to the fact that their cells has a fixed elliptical boundary and no deformability.

5.2 Effective viscosity of compound cell

In the validation of the compound cell iRBC model, the steady inclination angle of iRBC in the tank-treading motion in shear flow has been discussed.. The inclination angle
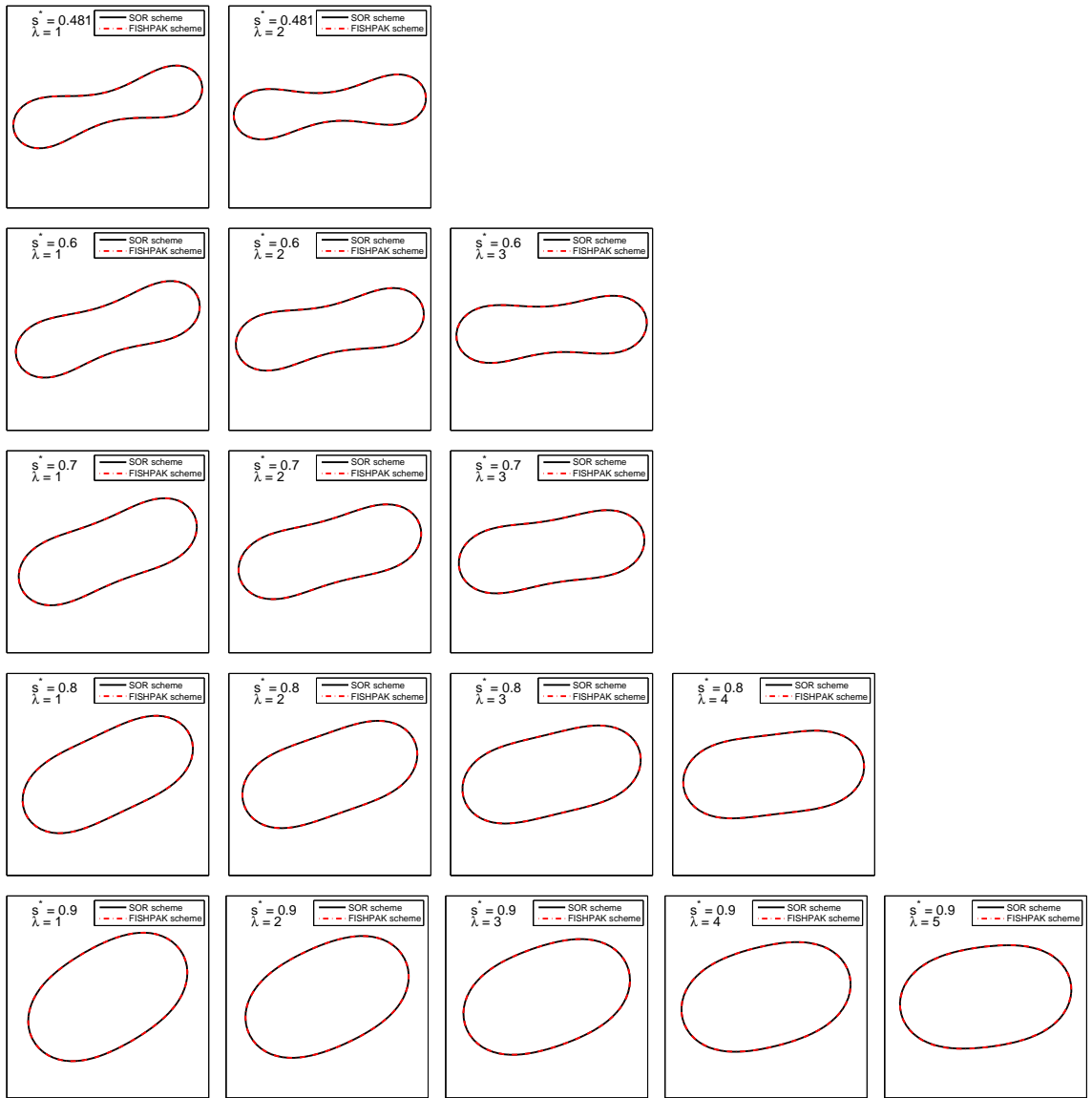
Figure 5.2: The final equilibrium shape of cells with swelling ratio $s^* = 0.481, 0.6, 0.7, 0.8, 0.9$ from top to bottom and viscosity ratio $\lambda = 1, 2, 3, 4, 5$ from left to right if any.
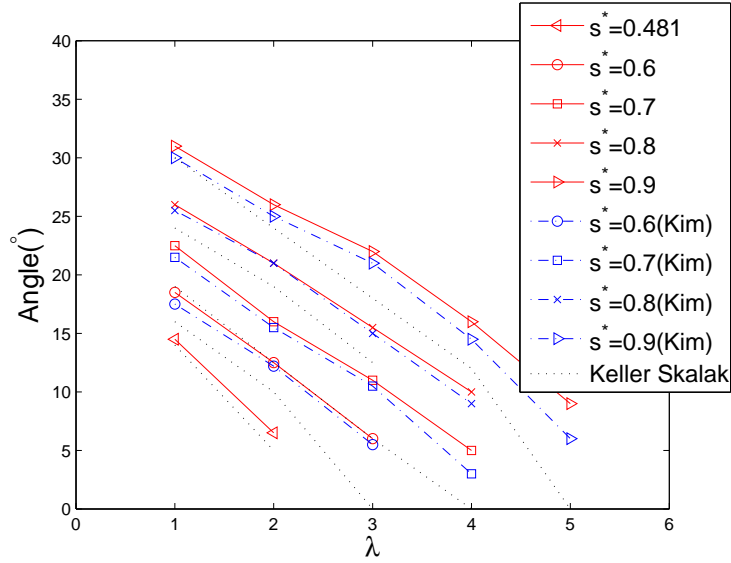
Figure 5.3: Steady inclination angle θ as a function of the viscosity ratio λ for different values of the swelling ratio s^*.

θ decreases as the filling fraction gets larger. In this section the effective viscosity due to the rigid inclusion is investigated. The computational domain is $30 \times 50 \mu m^2$. The cell mass center is put at channel center at $(15, 25)$. For the compound cell, the inclusion size raises from $\Phi = 0.05$ to $\Phi = 0.4$. The final equilibrium inclination angle verses filling fraction is plotted in Figure 5.4(a). As the inclusion size increases, the inclination angle decreases. The decrease in inclination angle due to increase of inclusion size is not as large as the cases in Chapter 4. It is because the domain of $20 \times 20 \mu m^2$ is much smaller there. The channel wall is closer to the membrane and has a stronger confinement effect on the iRBC motion. The velocity field of the tank-treading motion in the $20 \times 20 \mu m^2$ domain as in section 4.1 is plotted in Figure 5.5. And the velocity field of the current $30 \times 50 \mu m^2$ domain is plotted in Figure 5.6. The velocity field in the larger domain does have more than $10 \mu m$ for the flow field to adjust back to the simple shear flow pattern. We can consider the effect

77

of an rigid inclusion as a raise in interior fluid viscosity in the following way: The rigid inclusion blocks the inner circulation of the iRBC, the exchange of inner fluid can only be done through the narrow margin between the cell and the membrane. So the circulation of fluid inside the membrane is weakened like in a more viscos fluid. A polynomial fitting of the effective viscosity ratio as a function of inclusion fraction can be expressed as:

$$\lambda = 1 + 0.7930\Phi - 0.5960\Phi^2 + 3.2943\Phi^3 \tag{5.4}$$

A exponential fitting of the effective viscosity ratio as a function of inclusion fraction can be expressed as:

$$\lambda = (1 - \Phi)^{-0.6894} \tag{5.5}$$

The relation between the filling fraction and the effective viscosity ratio is plotted in Figure 5.4(b) along with a power law result. An illustration of the velocity field of inner circulation of a RBC and an iRBC is plotted in Figure 5.7 and 5.8. An rotation motion is observed for the rigid inclusion, which is different from the one with the fixed rigid filling in [34].

5.3   Issues with the new scheme

The new scheme allows the application of the fast solver to the diffusion problem but also brings about some issues. Since the coupling between the cell membrane and the fluid is done through an Immersed Boundary Method, the computational time step is very sensible to the forcing term. The terms moved to the right hand side in equation (2.77) contributes to the external force and may need a smaller time step which makes the scheme less efficient.

(a)

(b)
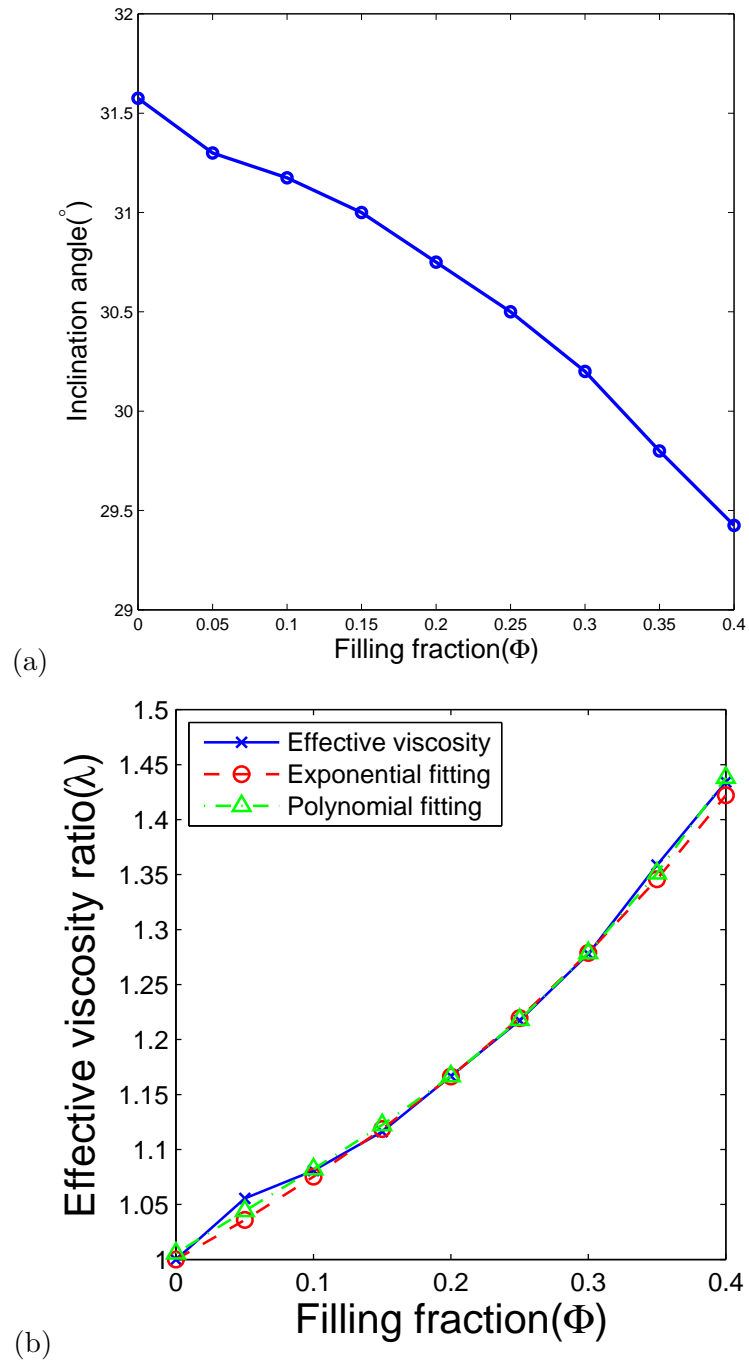
Figure 5.4: Equilibrium inclination angle of compound iRBC with inclusion ratio $\Phi = 0.05, 0.1, 0.15, 0.2, 0.25, 0.3, 0.35, 0.4$ and corresponding effective viscosity ratio.
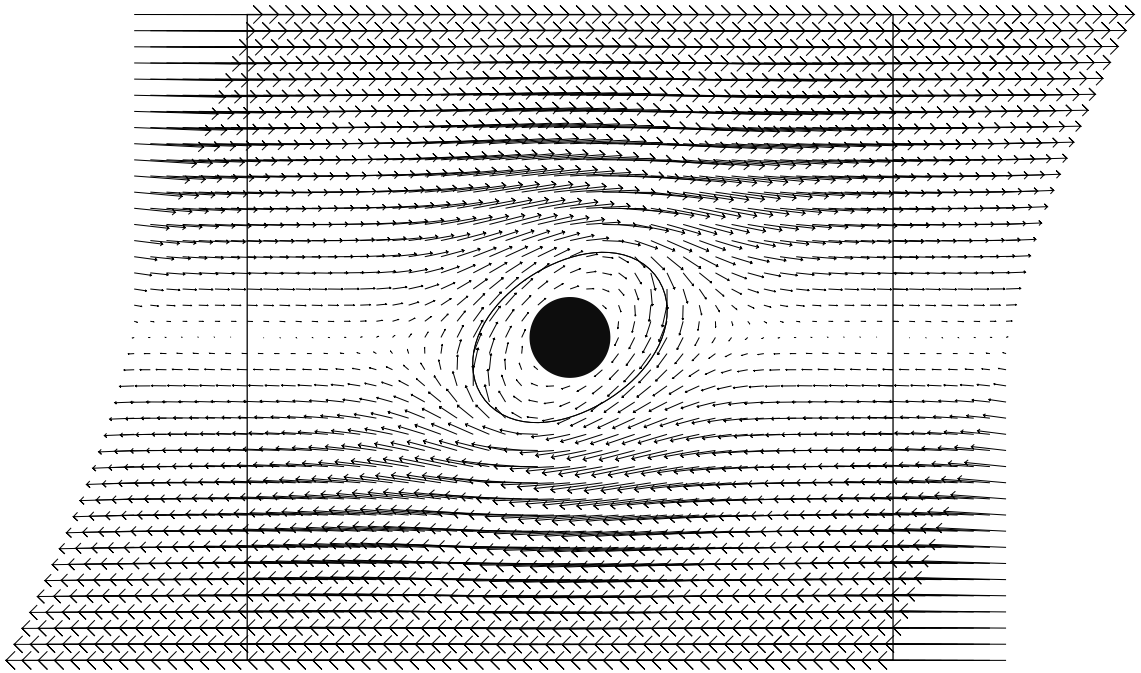
Figure 5.5: Velocity field of a compound iRBC tank-treading in a shearflow in a domain of $20 \times 20 \ \mu m^2$.
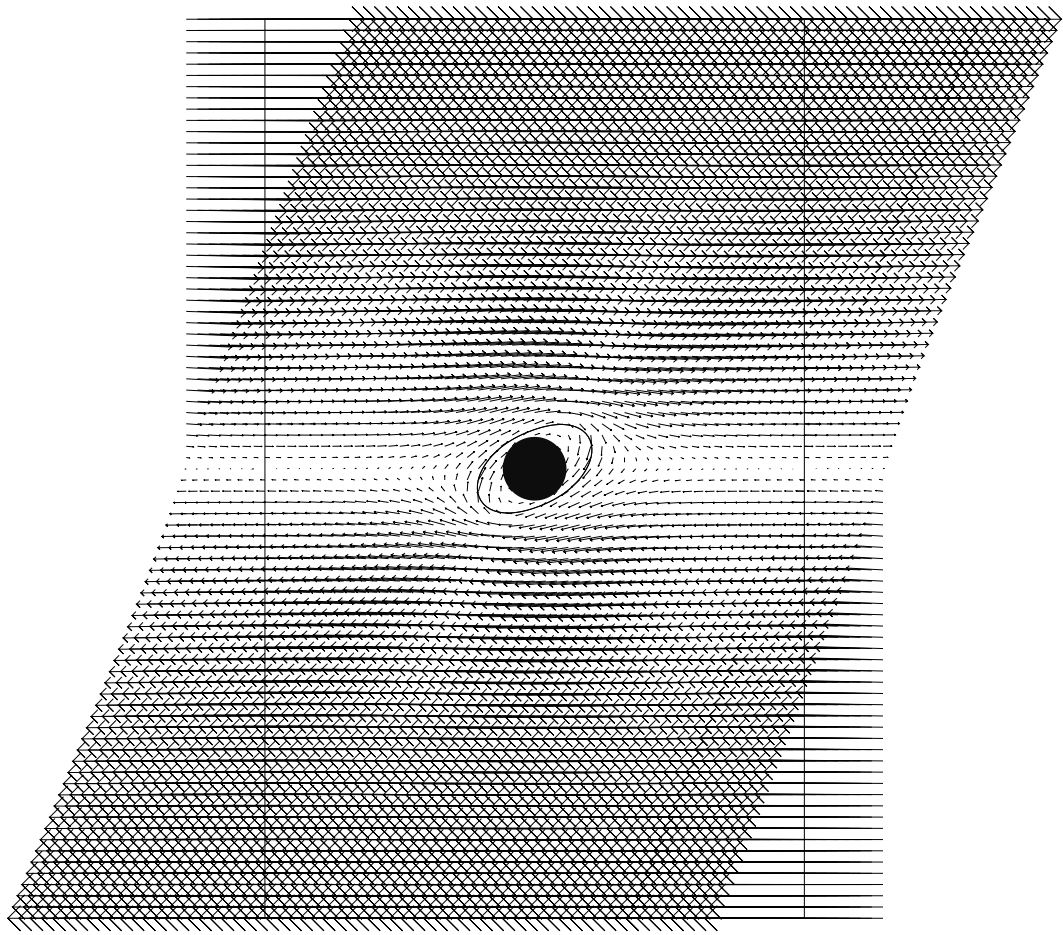
Figure 5.6: Velocity field of a compound iRBC tank-treading in a shearflow in a domain of $30 \times 50 \ \mu m^2$.
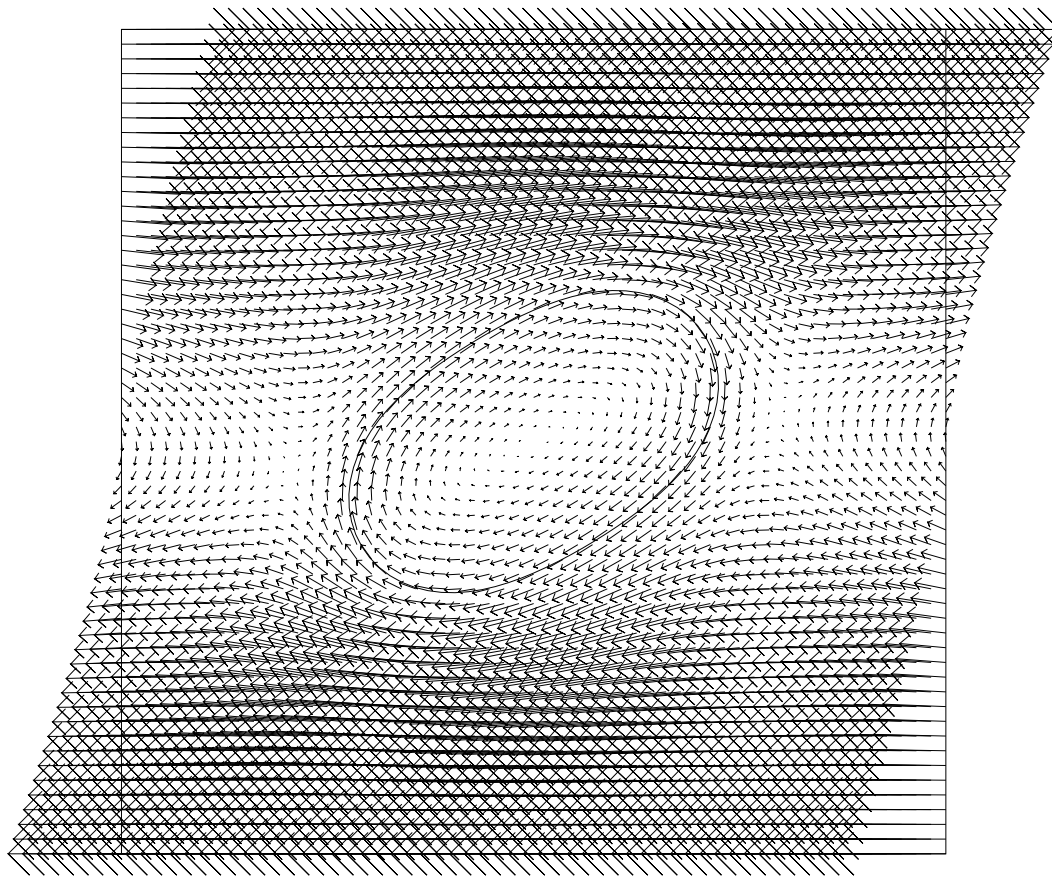
Figure 5.7: Velocity field of the inner circulation in a RBC.
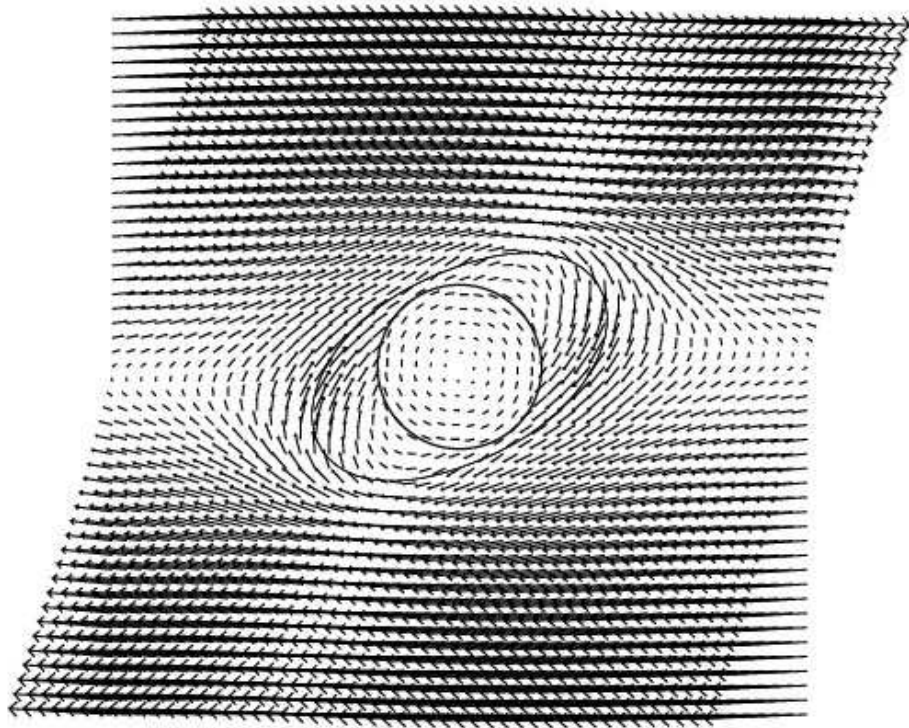
Figure 5.8: Velocity field of the inner circulation in an iRBC. The region inside the interior circle is the velocity field of the rigid inclusion

Chapter 6

Summary

6.1 Conclusion

The comparison of the motions of a single RBC under two flow models, namely the Navier-Stokes and the stationary Stokes, is presented in Chapter Three. As a benchmark problem, the elastic spring model for RBC and the two flow models are validated by the comparison of the steady inclination angles of the tank treading of a single RBC in a shear flow. Then motions of a single RBC in Poiseuille flow is investigated. The computational domain is a narrow channel with dimension 10×100 µm^2. When membrane stiffness is low, the RBC deforms easily due to the external force from the fluid. The combined effects of the cell deformability, the degree of confinement and the shear gradient of the Poiseuille flow make the RBC migrate toward a certain cross-sectional equilibrium position on or very close to the channel center line. By comparing the history of cell mass center, snapshots of positions and shapes of the cells and trajectory of marked points on the membranes, such deformation dominated migration motion under two different flow models has a very

84

good match with each other. The motions start to show difference when the cell becomes stiffer. The cell with biconcave shape is easier to bend along its long axis because it has plenty of excessive membrane length to be deformed while maintaining the cell area. The oscillation eventually damps out and the cell stays at the center region of the flow with a steady inclination angle. The elliptical shaped cell shows different motions under two flow models. In Navier-Stokes flow, a snaking motion is observed but a damped oscillation motion is observed in Stokes flow. This difference is caused by the inertial effect as the elliptical cell is less deformable due to the lack of excessive length and behaves closer to a rigid particle. The lifting inertial effect caused by the angular motion of the long axis of the cell gives the cell an extra push to keep the oscillation from damping out. As a conclusion for the comparison between the Navier-Stokes model and the Stokes model, both models can be used when the motion of the cell is deformation dominated. When the cell becomes stiffer, inertial effect becomes more important and a full Navier-Stokes model is a more proper model for the fluid.

In Chapter Four, the motions of malaria-infected RBC in blood flow is investigated by numerical simulation of a compound cell enclosing a rigid particle. Medical experiments show at late stage, the infected cell tend to migrate toward the vessel walls. Through numerical simulation we find this phenomenon can be explained as combination of two facts: 1) with a parasite inside the deformability of the RBC is hindered, making the cell hard to stay at the channel center; 2) It is easier for the healthy RBC to move toward the region where flow is faster because it has more excessive membrane and has less resist to deformation. While healthy RBC bypasses the iRBC, it pushes the iRBC toward the channel wall.

In Chapter Five, we present a new scheme in handling the non-constant viscosity of

interior and exterior fluid of a RBC. The effective viscosity of a compound cell with rigid inclusion is then investigated. As the inclusion grows in size, it blocks the inner circulation of fluid of the cell. The exchange of fluid can be done only through the narrow margin between the inclusion and the cell membrane. Such resistance to inner circulation can be understanded as a increase in effective viscosity. As the inclusion size increase, the effective viscosity also rises.

6.2   Future work

The comparison between the Navier-Stokes model and the Stokes model is done by comparing the motion of a single RBC in a narrow channel. The behavior of a single RBC in a wider channel and interactions between multiple RBCs in flow under these two flow models can be an interesting direction to work on.

To gain better understanding of how malaria-infected iRBCs affect human blood flow, the interactions between multiple iRBCs and RBCs in a wide channel need to be investigated.

Bibliography

[1] Abkarian M., Faivre M., and Viallat A., Swinging of red blood cells under shear flow, *Phys. Rev. Lett.*, **98**, 2007, 188302.

[2] Adams J., Swarztrauber P., Sweet R., FISHPAK: A package of Fortran subprograms for the solution of separable elliptic partial differential equations, The National Center for Atmospheric Research, Boulder, CO, 1980.

[3] Alexeev A., Verberg R., Balazs A.C., Modeling the interactions between deformable capsules rolling on a compliant surface, *Soft Matter*, **2**, 2006, 499-509.

[4] Atzberger P.J., Krameer P.R., Peskin C., A stochastic immersed boundary method for fluid-structure dynamics at microscopic length scales, *J. Comp. Phys.*, **224**, 2007, 1255-1292.

[5] Canham P.B., and Burton A.C., Distribution of size and shape in populations of normal human red cells, *Cir.Res.*,**22**, 1968, 405-422.

[6] Chorin A.J., Hughes T.J.R., McCracken M.F., Marsden J.E., Product formulas and numerical algorithms, *Comm. Pure Appl. Math.*, **31**, 1978, 205-256.

[7] Ciarlet P.G., The Finite Element Method for Elliptic Problems[M]. North-Holland, Amsterdam, 1978.

[8] Ciarlet P.G., Basic Error Estimates for Elliptic Problems[M]. Handbook of Numerical Analysis, P.G. Ciarlet and J.L. Lions (deceased) eds., North-Holland, Amsterdam, 1991, Vol. II: 17-351.

[9] Coupier G., Kaoui B., Podgorski T., and Misbah C., Non-inertial lateral migration of vesicles in bounded Poiseuille flow, *Physics of Fluids*, **20(11)**, 2008, 111702.

[10] Danker G, Vlahovska PM, and Misbah C., Vesicles in Poiseuille flow, *Phys. Rev. Lett.*, **102**, 2009, 148102.

[11] Dao M., Lim C.T., and Suresh S., Mechanics of the human red blood cell deformed by optical tweezers, *J. Mech. Phys. Solids.*, **51**, 2003, 2259-2280.

[12] Dean E.J., and Glowinski R., A wave equation approach to the numerical solution of the Navier-Stokes equations for incompressible viscous flow, *C.R. Acad. Sc. Paris, S erie 1*, **325**, 1997, 783-791.

[13] Dean E.J., Glowinski R., Pan T.W., A wave equation approach to the numerical simulation of incompressible viscous fluid flow modeled by the NavierStokes equations, In *Mathematical and Numerical Aspects of Wave Propagation*, De Santo J.A. (Ed.), SIAM: Philadelphia, 1998; 65-74.

[14] Deschamps J., Kantsler V., and Steinberg V., Phase diagram of sigle vesicle dynamical states in shear flow, *Phys. Rev. Lett.*, **102**, 2009, 118105.

[15] *http://blogs.discovermagazine.com/loom/page/184/#.UmCnQvHwNeo*

[16] Fischer T.M., Shape memory of human red blood cells, *Biophys. J.*, **86**, 2004, 3304-3313.

[17] Glowinski R, Pironneau O. Finite Element Methods for Navier-Stokes Equations[J]. *Annu. Rev. Fluid Mech.*, 1992, 24, 167-204.

[18] Glowinski R., Pan T.W., Hesla T., Joseph D.D., Periaux J., A fictitious domain approach to the direct numerical simulation of incompressible viscous flow past moving rigid bodies: Application to particulate flow, *J. Comput. Phys.*, **169**, 2001, 363-427.

[19] Glowinski R., Finite element methods for incompressible viscous flow, *Handbook of Numerical Analysis, Vol. IX, Ciarlet P.G. and Lions J.L. (Eds.), North-Holland, Amsterdam*, 2003, 7-1176.

[20] Glowinski R., Pan T.W., and Periaux J., A fictitious domain method for Dirichlet problem and applications, *Comp. Meth. in Appl. Mech. and Eng.*, **111**, 1994, 283-303.

[21] Haas K.H., Blom C., Ende D., Duits M.H.G., and Mellema J., Deformation of a giant lipid bilayer vesicles in shear flow, *Phys. Rev. E.*, **56**, 1997, 7132.

[22] Hou HW., Bhagat A.A., Chong GL., Mao P., Tam S.W., Han J., and Lim CT., Deformability based cell margination- a simple microfluidic design for malaria-infected erythrocyte separation, *Lab Chip*, **10**, 2010, 2605-2613.

[23] Johnson C., Streamline diffusion methods for problems in fluid mechanics. Finite Element in Fluids, R. Gallagher ed., Chichester, England and New York, Wiley-Interscience, 1985: 251-261.

[24] Kan H.C., Udaykumar H.S., Hydrodynamics of a compound drop with application to leukocyte modeling, *Phys. Fluids.*, **10(4)**, 1998, 760.

[25] Kantsler V., and Steinberg V., Transition to tumbling and two regimes of tumbling motion of a vesicle in shear flow, *Phys. Rev. Lett.*, **96**, 2006, 036001.

[26] Kaoui B., Ristow G.H., Cantat I., Misbah C., and Zimmermann W., Lateral migration of a two-dimensional vesicle in unbounded Poiseuille flow, *Phy. Rev. E*, **77(2)**, 2008, 021903.

[27] Kaoui B., Biros G., and Misbah C., Why do red blood cells have asymmetric shapes even in a symmetric flow, *Phys. Rev. E*, **80**, 2009, 188101.

[28] Kaoui B, Harting J, and Misbah C., Two-dimensional vesicle dynamics under shear flow: effect of confinement., *Phys. Rev. E*, **83**, 2011, 066319.

[29] Kaoui B., Kruger T., and Hatting J., How does confinement affect the dynamics of viscous vesicles and red blood cells?, *Soft Matter*, **8(35)**, 2012, 9246-9252.

[30] Karniadakis G. Em., Multiscale modeling of malaria, *SIAM News.*, **44(7)**, 2011.

[31] Koelman J.M.V.A, A simple Lattice Boltzmann Scheme for Navie-Stokes Fluid Flow *Europhys. Lett.*, **15(6)**, 1991, 603-607.

[32] Keller S.R., and Skalak R., Motion of a tank-treading ellipsoidal particle in a shear flow, *J. Fluid Mech.*, **120**, 1982, 27-47.

[33] Kim Y., and Lai M.C., Numerical study of viscosity on tank-treading and tumbling motions of vesicles under shear flow, *Phys. Rev. E*, **86**, 2012, 066321.

[34] Lai M-Ch., Hu W.F., and Lin W.W., A fractional step immersed boundary method for stokes flow with an inextensible interface enclosing a solid particle, *SIAM. J. Sci. Comput.*, **34(5)**, 2012, B692-B710.

[35] Mader M.-a., Vitkova V., Abkarian M., Viallat A., and Podgorski T., Dynamics of viscous vesicles in shear flow, *Eur. Phys. J. E.*, **19**, 2006, 389-397.

[36] Evolution of human-chimpanzee differences in malaria susceptibility: Relationship to human genetic loss of N-glycolylneuraminic acid, Martin M.J., Rayner J.C., Gagneux P., Barnwell J.W., and Varki A., *PNAS.*, **103(25)**, 2006, 9745.

[37] How malaria parasites reduce the deformability of infected RBC, *J. Biophys.*, **103**, 2012, 1-10,

[38] Miisbah C., Vacillating breathing and tumbling of vesicles under shear, *Phys. Rev. Lett.*, **96**, 2006, 028104.

[39] Nash G.B., O'Brien E., Gordon-Smith E.C., and Dormandy J.A. Abnomalities in the mechanical properties of red blood cells caused by plasmodium falciparum, *Blood*, **84**, 1989, 855-861

[40] Haldar K., Kamoun S., Hiller N.L., Bhattacharje S., and Ooij C., Common infection strategies of pathogenic eukaryotes.
http://www.nature.com/nrmicro/journal/v7/n5/fig_tab/nrmicro2110_F1.html,

89

[41] What Is Sickle Cell Anemia,
http://www.nhlbi.nih.gov/health/health-topics/topics/sca/

[42] Niu X., Shi L., Pan TW., Glowinski R., The effect of shape memory on red blood cell motions, *(submitted)*,

[43] Noguchi H., and Gompper G., Swinging and tumbling of fluid vesicles in shear flow, *Phys. Rev. Lett.*, **98**, 2007, 128103.

[44] Pan T.W., Glowinski R., Direct simulation of the motion of neutrally buoyant circular cylinders in plane Poiseuille flow, *J. Comput. Phys.*, **181**, 2002, 260-279.

[45] Pan T.W., Error bounds for a fictitious domain method with lagrange multiplier treatment on the boundary for a Dirichlet problem, *Jap. J. Indust. Appl. Math.*, **15**, 1998, 75-85.

[46] Pan T.W., Joseph D.D., Bai R., Glowinski R., and Sarin V., Fluidization of 1204 spheres: simulation and experiments, *J. Fluid. Mech.*, **451**, 2002, 169-191.

[47] Peskin C.S., Numerical analysis of blood flow in the heart, *J. Comput. Phys.*, **25**, 1977, 220-252.

[48] Peskin C.S., and McQueen D.M., Modeling prosthetic heart valves for numerical analysis of blood flow in the heart, *J. Comput. Phys.*, **37**, 1980, 113-132.

[49] Peskin C.S., The immersed boundary method, *Acta Numer.*, **11**, 2002, 479-517.

[50] Pironneau O., Finite Element Methods for Fluids[M]. J. Wiley, Chichester, 1989.

[51] Pozrikidis C., Numerical simulation of cell motion in tube flow, *Ann. Biomed. Eng.*, **33**, 2005, 165-178.

[52] Pan TW, and Wang T., Dynamical simulation of red blood cell rheology in microvessels, *International Journal of Numerical Analysis and Modeling*, **6(30**, 2009, 455-473.

[53] Rannacher R., On Chorin's projection method for the incompressible Navier-Stokes Equations, *Lect. Notes. in Math.*, **1530**, 1992, 167-183.

[54] Secomb T.W., and Skalak R., A two-dimensional model for asymmetric cell, *Microvas. Res*, bf 24, 1982, 194-203

[55] Shelby J.P., White J., Ganesan K., Rathod P. K., and Chiu D. T., A microfluidic model for single-cell capillary obstruction by Plasmodium falciparum-infected erythrocytes *Proc. Natl. Acad. Sci. U.S.A.*, **100**, 2003, 14618-14622.

[56] Shi L., Pan TW., Glowinski R., Numerical simulation of lateral migration of red blood cells in Poiseuille flows, *Int. J. Numer. Meth. Fluids.*, **68**, 2012, 1393-1408.

[57] Shi L., Pan T.W., and Glowinski R., Deformation of a single red blood cell in bounded Poiseuille flows, *Phys. Rev. E*, **85**, 2012, 016307.

[58] Shi L., Yu Y., Pan T.W., and Glowinski R., On oscillating motion of a red blood cell and a neutrally buoyant rigid particle in Poiseuille flow in a narrow channel, *J. Phys. Fluids (submitted).*

[59] Human blood flow.
https://mville.digication.com/neeta_yousaf/Chemical_Composition_of_Cell_Membrane

[60] Suresh S., Spatz J.,Mills J.P.,Micoulet A., and Dao M., Connections between sigle-cell biomechanics and human disease states: gastrointestinal cancer and malaria, *Acta. Biom.*, **1**, 2005, 15-30

[61] Impact of a compound droplet on a flat surface: A model for single cell epitaxy, *Phys. Fluid.*, **22(8)**, 1994, 082103.

[62] Tsubota K., Wada S., and Yamaguchi T., Simulation study on effects of hematocrit on blood flow properties using particle method, *J. Biomech. Sci. Eng.*, **1**, 2006, 159-170

[63] Wang T., Pan T.W., Xing Z., Glowinski R., Numerical simulation of rheology of red blood cell rouleaux in microchannels, *Phys. Rev. E*, **79**, 2009, 041916.

[64] Wu T., Feng J., Simulation of malaria-infected red blood cells in microfluidic channels: passage and blockage, *Biomicrofluidics.*, **7**, 2013, 044115.

[65] Yoshino M., and Murayama T., A lattice Boltzmann method for a two-phase flow containing solid bodies with viscoelastic membranes, s *Eur. Phys. J. Special. Topics*, **171**, 2009, 151-157.

[66] Zhang J., Johnson P.C., and Popel A.S., Effects of erythrocyte deformability and aggregation on the cell free layer and the apparent viscosity of microscopic blood flows, *Microvascular Research*, **77**, 2009, 265-272.

[67] Zhao H., Isfahani A.H.G., Olson L.N., and Freund J.B., A spectral boundary integral method for flowing blood cells, *J. of Comp. Fluids.*, **229**, 2010, 3726-3744.